





This is to certify that the

dissertation entitled

**Using Beam Polarization to Study  
Anomalous Electroweak Physics and  
Supersymmetry**

presented by

**Michael C. Wiest**

has been accepted towards fulfillment  
of the requirements for

PhD degree in Physics

*Daniel Stump*  
Major professor

Date November 23, 1997

**LIBRARY**  
**Michigan State**  
**University**

**PLACE IN RETURN BOX**  
to remove this checkout from your record.  
**TO AVOID FINES** return on or before date due.

DATE DUE	DATE DUE	DATE DUE
_____	_____	_____
_____	_____	_____
_____	_____	_____
_____	_____	_____
_____	_____	_____

USING BEAM POLARIZATION TO STUDY  
ANOMALOUS ELECTROWEAK PHYSICS  
AND  
SUPERSYMMETRY

by  
Michael Christian Wiest

A DISSERTATION  
Submitted to  
Michigan State University  
in partial fulfillment of the requirements  
for the degree of  
DOCTOR OF PHILOSOPHY

Department of Physics and Astronomy

1997

ABSTRACT

USING BEAM POLARIZATION TO STUDY  
ANOMALOUS ELECTROWEAK PHYSICS AND SUPERSYMMETRY

By

Michael Christian Wiest

This thesis considers the phenomenology of two classes of possible fundamental interactions and fields not present in the Standard Model (SM) of high-energy physics. The topics are associated because each example considers how a collider experiment with a longitudinally polarized beam might be used to study the interactions.

It is technically feasible to polarize the proton beam at the Fermilab Tevatron collider. In Part I we model an experiment at a polarized Tevatron, to compare its capabilities to the existing unpolarized Tevatron. In particular, we estimate the precision with which the Standard Model (SM) electroweak triple-boson couplings could be tested; that is, we calculate limits on possible *anomalous* electroweak triple-boson couplings, for a polarized and an unpolarized Tevatron. For comparison to the Tevatron, and as a simpler illustrative calculation, we first calculate the rate of  $W^+W^-$  production at two  $e^+e^-$  colliders, LEP II and the proposed NLC. This process is sensitive to the triple-boson couplings, so the event rate allows us to estimate limits which could be placed on anomalous couplings using data from these two colliders. We then calculate the rates of  $W^+W^-$  production and  $W + \gamma$  production at the Tevatron  $p\bar{p}$  collider with and without a longitudinally polarized proton beam, to gauge the increase in sensitivity with a polarized beam. Because accurate polarized parton distribution functions (ppdf's) would be required for precise predictions, we also consider how measurement of single- $W$  production with a polarized proton beam could be used to improve the accuracy of the ppdf's. The physical decays of

the produced  $W$  bosons are included in all of these calculations.

In Part II we identify the region of parameter space for which the proposed NLC would be able to detect a very light (order keV) gravitino, which is *required* in gauge-mediated models of supersymmetry-breaking, and allowed in “no-scale” models of unified supergravity. To map this accessible parameter space, we calculate the production of gaugino pairs which decay to photons and gravitinos:  $e^+e^- \rightarrow \chi_1^0\chi_1^0 \rightarrow \gamma\gamma GG$ . In such an experiment, the polarized electron beam of the NLC would make it possible to eliminate a background process.

*Dedicated with love to my parents,  
Toni and Michael*

## Acknowledgements

I am most grateful to my thesis advisor, Dan Stump, for his invaluable contribution to my graduate education. My debt to him began to accrue from my first year at MSU, when he introduced our class to quantum mechanics with his well-known clarity and authority. Since I became his student, he has been extremely generous with his time and knowledge, and quite willing to tailor my research to my interests. I am very grateful for the opportunity to osmotically improve my understanding of quantum field theory. I also owe to Dr. Stump an appreciation of what makes a scientifically interesting problem, and an appreciation for thoroughness of investigation. When I would begin to drift into the clouds of speculation, Dr. Stump gently brought me back to earth.

I am grateful to C.-P. Yuan for suggesting the project which became Part I of my thesis, and for his collaboration in that work. I also thank Dr. Yuan for much helpful advice, and for teaching me (in class and out) methods of “practical” field theory, as well as for serving officially on my guidance committee.

If the gift of wisdom excels all others, then the gift of a humorous anecdote may rank second. Gerald Pollack generously shared both with me. Encountering Dr. Pollack in the halls of the physics building during my years here greatly reduced the lab-rat feeling that results from endlessly walking back and forth in a concrete hall. I also thank Dr. Pollack for serving on my guidance committee.

I thank Chip Brock for serving on my guidance committee and for his course which introduced me to quantum field theory. Thanks to Aaron Galonsky for serving on my committee and for encouraging discussions. Thanks to Wayne Repko for guiding me through a physics “800” project which taught me FORTRAN, and for radiating a relaxed attitude at me in the hallways. I also gratefully acknowledge Carl Schmidt’s course on supersymmetry and Jeff Kuhn’s gravity course. I

feel lucky for the exposure to Einstein's wonderful theory and its quantum mechanical sibling. I thank Eric Poppitz, whose talk on gauge-mediated supersymmetry breaking suggested to me the idea for Part II of this thesis.

In *Down and Out in Paris and London*, George Orwell defines the idiomatic French word "debrouillard" to mean something like, "someone who, when asked to do the impossible, finds a way." Stephanie Holland of the graduate physics office has just such a "can-do" attitude. I am grateful to her and to Jules Kovacs for defeating countless frumious beaurocratic bandersnatches. I also gratefully acknowledge much similar help from Mary Curtis, Lisa Ruess, Lorie Neuman; and Jeanette Dubendorf, who helped me with the laborious typing of address labels for post-doc applications. Thanks to George Perkins for waking me from many computer nightmares. My teaching assistantships were enhanced by cheerful support from Peter Signell, Gene Kales, Jack Hetherington, Jerzy Borysowicz, Harry Weerts, Carl Bromberg, and especially Michelle Li of the CBI administration.

Without my fellow graduate students and post-docs I might well have ended like the legendary student found naked on a traffic island, crying "Newton was wrong!" I am grateful for their friendship as well as their help with my studies. Thanks to Doug Carlson for his collaboration and for sharing his home-brewed beer. Thanks to Glenn Ladinsky for sharing his expertise and his program for generating polarized parton distributions. I'm grateful to Joelle Murray, Hung-Liang Lai, Csaba Balazs, Jim Hughes, Xiaoning Wang, Andre Maul, David Bowser-Chao, Francisco Larios, Tim Tait, Tom Rockwell, Gian Diloretto, Steve Jerger, and Jim Amundson for all sorts of technical and moral support. Thank you Kate Frame for invaluable "reality checks" and your cherished friendship. I also thank Ann Connor for her support and patience with me during these final months of thesis writing.

Finally I thank my parents, Michael and Toni, and my brother Matthew, and

the rest of my family, who are my foundation. I cannot adequately express my debt or my gratitude to them.

# Contents

<b>List of Tables</b>	<b>xi</b>
<b>List of Figures</b>	<b>xv</b>
<b>1 Introduction</b>	<b>1</b>
1.1 The Standard Model . . . . .	1
1.1.1 Quantum Chromodynamics . . . . .	2
1.1.2 The Electroweak Sector . . . . .	3
1.1.3 The Higgs Sector . . . . .	3
1.1.4 Generations, the CKM Matrix, and CP violation . . . . .	5
1.1.5 Summary of the Standard Model . . . . .	6
1.2 Triple-Boson Couplings . . . . .	7
1.3 Beam Polarization . . . . .	13
1.4 The Organization of This Thesis . . . . .	14
<b>I Anomalous Electroweak Triple-Boson Couplings</b>	<b>15</b>
<b>2 Probing Anomalous Triple-Boson Couplings with <math>e^-e^+ \rightarrow W^-W^+</math></b>	<b>16</b>
2.1 Introduction . . . . .	16
2.1.1 Calculation . . . . .	18
2.1.2 Estimation of Sensitivity to Anomalous Couplings . . . . .	24

2.1.3	Using $\chi^2$ to Estimate Sensitivities to Anomalous Couplings . .	28
2.1.4	Conclusions . . . . .	31
<b>3</b>	<b>Probing Anomalous Triple-Boson Couplings with Polarized Proton—</b>	
	<b>Antiproton Collisions</b>	<b>35</b>
3.1	Introduction . . . . .	35
3.2	$W^+\gamma$ production . . . . .	39
3.2.1	Method of Calculation . . . . .	39
3.2.2	Results . . . . .	42
3.2.3	Limits on $\Delta\kappa_\gamma$ and $\lambda_\gamma$ . . . . .	45
3.3	$W^+W^-$ production . . . . .	46
3.3.1	Background, Approximations, and Cuts . . . . .	49
3.3.2	Results . . . . .	57
3.3.3	Limits on $\Delta\kappa_\gamma$ , $\Delta\kappa_Z$ , $\lambda_\gamma$ , and $\lambda_Z$ . . . . .	62
3.3.4	Interpretation of the Results . . . . .	64
3.4	Discussion and Conclusions . . . . .	65
<b>4</b>	<b>Probing the Polarized Parton Distributions with <math>p\bar{p} \rightarrow W</math></b>	<b>75</b>
4.1	Introduction . . . . .	75
4.2	$W^\pm$ production . . . . .	77
4.3	Decay of $W^\pm$ . . . . .	86
4.4	Conclusions . . . . .	94
<b>II</b>	<b>A Light Gravitino and the Supersymmetry Breaking</b>	
	<b>Mechanism</b>	<b>96</b>
<b>5</b>	<b>Detecting a Light Gravitino at a Future Linear Collider</b>	<b>97</b>
5.1	Introduction to Supersymmetry . . . . .	97

5.1.1	Supersymmetry Breaking . . . . .	100
5.2	Introduction to the Problem at Hand . . . . .	102
5.3	Detecting a Light Gravitino at the Next Linear Collider . . . . .	104
5.3.1	Production of Neutralino Pairs at the NLC . . . . .	104
5.3.2	Decay of the Neutralino . . . . .	106
5.3.3	Background-Free Signal Events . . . . .	109
5.3.4	Non-Background-Free Signal Events . . . . .	115
5.4	Discussion and Conclusion . . . . .	121
5.5	Additional Comments . . . . .	126
<b>A</b>	<b>The Standard Model Lagrangian</b>	<b>128</b>
<b>B</b>	<b>Helicity Amplitude Method</b>	<b>131</b>
B.1	Helicity Eigenstates . . . . .	131
B.2	Example Calculation . . . . .	134

# List of Tables

1.1	Current 95% C.L. limits on anomalous couplings from direct cross section measurements. A subscript $\gamma, Z$ indicates that the photon and $Z$ anomalous couplings were assumed equal. All couplings but those being limited were fixed at their SM values. All entries shown were calculated with $\Lambda = 1.5$ TeV, except the last, from Reference [12], for which $\Lambda = 1.0$ TeV. . . . .	10
2.1	Final state cuts. . . . .	20
2.2	LEP II limits on $\Delta\kappa_\gamma$ from the total cross section. . . . .	26
2.3	NLC limits on $\Delta\kappa_\gamma$ from the total cross section. . . . .	26
2.4	LEP II limits on $\Delta\kappa_\gamma$ from $\tilde{\chi}^2$ of $\cos\theta_e$ distribution. . . . .	31
2.5	NLC limits on $\Delta\kappa_\gamma$ from $\tilde{\chi}^2$ of $\cos\theta_e$ distribution. . . . .	33
3.1	Cross-section for the process $p\bar{p} \rightarrow W^+\gamma$ with polarized protons, for different values of the anomalous coupling $\Delta\kappa_\gamma$ , assuming $\lambda_\gamma = 0$ . Cross-sections are in pb. The branching ratio $2/9$ for $W^+ \rightarrow e^+\nu_e$ or $\mu^+\nu_\mu$ , and the effect of our cuts, is included. The unpolarized case was calculated separately using CTEQ2 parton distribution functions, for comparison. The asymmetry $\mathcal{A}$ , defined in Eq. (3.7), is calculated by fitting the data to a parabola. . . . .	68

3.2	Cross-section for the process $p\bar{p} \rightarrow W^+\gamma$ with polarized protons, for different values of the anomalous coupling $\lambda_\gamma$ , assuming $\Delta\kappa_\gamma = 0$ . Cross-sections are in pb. The unpolarized case was calculated separately using CTEQ2 parton distribution functions, for comparison. The asymmetry $\mathcal{A}$ , defined in Eq. (3.7), is calculated by fitting the data to a parabola. . . . .	68
3.3	Limits on non-Standard couplings, from $p\bar{p} \rightarrow W^+\gamma$ with polarized and unpolarized protons. The upper number is for $1 \text{ fb}^{-1}$ integrated luminosity, and the lower number (in parentheses) is for $10 \text{ fb}^{-1}$ . . .	69
3.4	Purely electroweak cross-sections, in pb, for $p(R)\bar{p} \rightarrow W^+ + 2 \text{ jets}$ , with $W^+ \rightarrow \bar{\ell}\nu$ where $\ell = e$ or $\mu$ ; the proton is right-handed. The cross-section for $p(R)\bar{p} \rightarrow W^- + 2 \text{ jets}$ is the same. The branching ratio $(2/9) \times (6/9) = 4/27$ and the effect of our cuts are included. . .	70
3.5	Purely electroweak cross-sections, in pb, for $p(L)\bar{p} \rightarrow W^+ + 2 \text{ jets}$ , with $W^+ \rightarrow \bar{\ell}\nu$ where $\ell = e$ or $\mu$ ; the proton is left-handed. The cross-section for $p(L)\bar{p} \rightarrow W^- + 2 \text{ jets}$ is the same. The branching ratio $(2/9) \times (6/9) = 4/27$ and the effect of our cuts are included. . .	71
3.6	Purely electroweak cross-sections, in pb, for $p\bar{p} \rightarrow W^+ + 2 \text{ jets}$ , with $W^+ \rightarrow \bar{\ell}\nu$ where $\ell = e$ or $\mu$ ; the proton is unpolarized. The cross-section for $p\bar{p} \rightarrow W^- + 2 \text{ jets}$ is the same. The branching ratio $(2/9) \times (6/9) = 4/27$ and the effect of our cuts are included. These values were calculated independently using the Morfin-Tung ppdf's; the cross-section for unpolarized protons is equal to the average of cross-section for left and right polarized protons. . . . .	71

3.7	Electroweak cross-sections, in pb, for $W^+W^-$ production with non-Standard couplings, with polarized or unpolarized protons, and with a large- $\sqrt{\hat{s}}$ cut, $\sqrt{\hat{s}} > 340$ GeV. One $W$ decays leptonically, the other to 2 jets, and the branching ratio 4/27 and the effect of our cuts are included in the cross-section. Two assumptions on non-Standard couplings are listed: $\Delta\kappa_\gamma = \Delta\kappa_Z$ with $\lambda_\gamma = \lambda_Z = 0$ , and $\lambda_\gamma = \lambda_Z$ with $\Delta\kappa_\gamma = \Delta\kappa_Z = 0$ . . . . .	72
3.8	QCD background cross-sections for $p\bar{p} \rightarrow W^\pm + 2 jets$ , for various proton polarizations and kinematic cuts. The unpolarized cases $\sigma(p\bar{p} \rightarrow W^+ 2j) = \sigma(p\bar{p} \rightarrow W^- 2j)$ were calculated separately using CTEQ2 parton distribution functions. . . . .	73
3.9	Limits on anomalous couplings that could be set from $p\bar{p} \rightarrow W^\pm + 2 jets$ with polarized or unpolarized protons. The numbers in parentheses are for $10 \text{ fb}^{-1}$ integrated luminosity, and the other numbers are for $1 \text{ fb}^{-1}$ integrated luminosity. . . . .	73
3.10	Limits on anomalous couplings that could be set from $p\bar{p} \rightarrow W^\pm + 2 jets$ with polarized or unpolarized protons, from events with $\sqrt{\hat{s}} > 340$ GeV. The numbers in parentheses are for $10 \text{ fb}^{-1}$ integrated luminosity, and the other numbers are for $1 \text{ fb}^{-1}$ integrated luminosity. . . . .	74
3.11	Effect of parton $Q$ scale on the calculated cross-section for background processes $p\bar{p} \rightarrow W^\pm + 2 jets$ . These are unpolarized cross-sections, calculated with CTEQ2 parton distribution functions. . . . .	74

4.1	Total cross-sections for the processes $p_\lambda + \bar{p} \rightarrow W^\pm \rightarrow e^\pm + \bar{\nu}_e^{(-)}$ , where $\lambda$ is the proton polarization, $L$ or $R$ . The polarized parton distribution functions are taken from Refs. [38] and [39]. Also, we consider a transverse momentum cut $p_{Te} > p_{Tmin}$ . There is no restriction on lepton rapidity $y_e$ ; the effect of a cut on $y_e$ may be judged from Figs. 4.8, 4.9, 4.11, 4.12. . . . .	94
5.1	Production cross-section $\sigma$ and typical decay distance $D$ for the process $e_R^- e^+ \rightarrow \chi_1^0 \chi_1^0$ at the NLC, assuming $\alpha = 0$ , for several values of masses. (Note that the electron beam is right-hand polarized, so the cross-section is a factor of 2 larger than that for an unpolarized electron beam.) These numbers are for $M_{susy} = 10^6$ GeV. . . . .	113
B.1	Helicity states in two-component spinor, and bra-ket notation. . . . .	132
B.2	Dirac helicity eigenvectors for massless fermions. . . . .	133

# List of Figures

2.1	Diagrams for $e^-e^+ \rightarrow W^-W^+ \rightarrow l^-\bar{\nu}q\bar{q}'$ . . . . .	19
2.2	Rapidity distributions of the $W^-$ at LEP II from analytic amplitudes (smooth) and uncut Monte Carlo calculation (histogram). . . . .	19
2.3	Rapidity distributions of the $W^-$ at NLC from analytic amplitudes of (smooth) and uncut Monte Carlo calculation (histogram). . . . .	20
2.4	$d\sigma/dy_e$ at LEP II, without cuts, for $e^+e^- \rightarrow W^+W^- \rightarrow e^-\bar{\nu}_e u_{red}\bar{d}_{red}$ . Solid line is SM, dashed is $\Delta\kappa_\gamma = -0.5$ . . . . .	22
2.5	$d\sigma/dy_e$ at LEP II, with cuts, for $e^+e^- \rightarrow W^+W^- \rightarrow e^-\bar{\nu}_e u_{red}\bar{d}_{red}$ . Solid line is SM, dashed is $\Delta\kappa_\gamma = -0.5$ . . . . .	23
2.6	Total cross section at LEP II for $e^+e^- \rightarrow W^+W^- \rightarrow l^-\bar{\nu}q\bar{q}'$ vs. $\Delta\kappa_\gamma$ . . . . .	25
2.7	Total cross section at NLC for $e^+e^- \rightarrow W^+W^- \rightarrow l^-\bar{\nu}q\bar{q}'$ vs. $\Delta\kappa_\gamma$ . . . . .	25
2.8	Total cross section at NLC for $e^+e^- \rightarrow W^+W^-$ vs. $\Delta\kappa_\gamma$ . The solid and dashed curves are for left and right polarized electron beams, respectively. . . . .	27
2.9	Differential cross sections in cosine of the lepton angle at LEP II and NLC for two values of $\Delta\kappa_\gamma$ . . . . .	30
2.10	$\tilde{\chi}_{th}^2$ at LEP II for $e^+e^- \rightarrow W^+W^- \rightarrow l^-\bar{\nu}q\bar{q}'$ vs. $\Delta\kappa_\gamma$ . . . . .	32
2.11	$\tilde{\chi}_{th}^2$ at NLC for $e^+e^- \rightarrow W^+W^- \rightarrow l^-\bar{\nu}q\bar{q}'$ vs. $\Delta\kappa_\gamma$ . . . . .	32

3.1	Polarized parton distribution functions. The curves are $x\Delta f(x)$ vs $x$ for parton types $u_{val}$ , $d_{val}$ , $u_{sea}(=d_{sea})$ , $g$ , which are the most important partons in our calculations. . . . .	38
3.2	Feynman diagrams for the process $u\bar{d} \rightarrow e^+\nu\gamma$ . . . . .	40
3.3	Total cross-section (with cuts in Eqs.(3.3)–(3.5)) for polarized protons vs anomalous coupling $\Delta\kappa_\gamma$ , assuming $\lambda_\gamma = 0$ . The unpolarized cross-section was calculated separately using CTEQ2 parton distribution functions. . . . .	42
3.4	Total cross-section (with cuts in Eqs.(3.3)–(3.5)) for polarized protons vs anomalous coupling $\lambda_\gamma$ , assuming $\Delta\kappa_\gamma = 0$ . The unpolarized cross-section was calculated separately using CTEQ2 parton distribution functions. . . . .	43
3.5	Distribution of photon transverse momentum $p_{T\gamma}$ . The solid line is for $\Delta\kappa_\gamma = 0$ , and the dashed line is for $\Delta\kappa_\gamma = -1$ ; in both cases $\lambda_\gamma = 0$ . . . . .	44
3.6	Complete set of electroweak diagrams for $u+\bar{u} \rightarrow d+\bar{u}+W^+ (\rightarrow \bar{\ell} + \nu_\ell)$ . 47	
3.7	Example diagrams for QCD production of $W^+$ and two jets. . . . .	49
3.8	Two-jet invariant mass distribution for the signal process. The solid line is the result of the complete calculation of the pure electroweak process $p + \bar{p} \rightarrow q\bar{q}'W^+$ , with $W^+ \rightarrow \bar{\ell}\nu_\ell$ ; the dotted line is the result of the calculation of $W^+W^-$ production, with $W^+ \rightarrow \bar{\ell}\nu_\ell$ and $W^- \rightarrow 2 jets$ , with a cut on the two-jet invariant mass ( $70 < M_{2j} < 90$ GeV). . . . .	51
3.9	Two-jet invariant mass distribution for the QCD background processes $p\bar{p} \rightarrow W^+ + 2 jets$ . (The cross-section for $W^- + 2 jets$ is the same, for unpolarized scattering.) . . . . .	52

3.10	$\sqrt{\hat{s}}$ distribution for the signal process. The solid line is the result of the complete calculation of the pure electroweak process $p + \bar{p} \rightarrow q\bar{q}'W^+$ , with $W^+ \rightarrow \bar{\ell}\nu_\ell$ ; the dotted line is the result of the calculation of $W^+W^-$ production, with $W^+ \rightarrow \bar{\ell}\nu_\ell$ and $W^- \rightarrow 2 \text{ jets}$ , with a cut on the two-jet invariant mass ( $70 < M_{2j} < 90 \text{ GeV}$ ). . . . .	54
3.11	Comparison of $\sqrt{\hat{s}}$ distributions for signal and background processes. The solid line is the QCD background. The dotted line is the electroweak process, with zero anomalous couplings; the dashed line is the electroweak process with $\Delta\kappa_\gamma = \Delta\kappa_Z = 0.5$ . . . . .	55
3.12	Comparison of $\sqrt{\hat{s}}$ distributions for signal and background processes, for $\sqrt{\hat{s}} > 340 \text{ GeV}$ . The solid line is the QCD background. The dotted line is the electroweak process, with zero anomalous couplings; the dashed line is the electroweak process with $\Delta\kappa_\gamma = \Delta\kappa_Z = 0.5$ . . . . .	56
3.13	Electroweak cross-section for $p_\lambda\bar{p} \rightarrow W^+W^-$ as a function of anomalous couplings $\Delta\kappa$ , for polarized ( $L, R$ ) and unpolarized protons. For each polarization, three cases are shown, corresponding to assumptions ( $\times$ ) $\Delta\kappa_\gamma \neq 0$ and $\Delta\kappa_Z = 0$ , ( $\diamond$ ) $\Delta\kappa_\gamma = 0$ and $\Delta\kappa_Z \neq 0$ , and ( $\square$ ) $\Delta\kappa_\gamma = \Delta\kappa_Z$ . In all cases $\lambda_\gamma = \lambda_Z = 0$ . . . . .	59
3.14	Electroweak cross-section for $p_\lambda\bar{p} \rightarrow W^+W^-$ as a function of anomalous couplings $\lambda$ , for polarized ( $L, R$ ) and unpolarized protons. For each polarization, three cases are shown, corresponding to assumptions ( $\times$ ) $\lambda_\gamma \neq 0$ and $\lambda_Z = 0$ , ( $\diamond$ ) $\lambda_\gamma = 0$ and $\lambda_Z \neq 0$ , and ( $\square$ ) $\lambda_\gamma = \lambda_Z$ . In all cases $\Delta\kappa_\gamma = \Delta\kappa_Z = 0$ . . . . .	60

3.15	Electroweak cross-section for $p_\lambda \bar{p} \rightarrow W^+ W^-$ as a function of anomalous couplings, with $\sqrt{\hat{s}} > 340$ GeV. For each polarization, two cases are shown, corresponding to assumptions ( $\times$ ) $\Delta\kappa_\gamma = \Delta\kappa_Z$ with $\lambda_\gamma = \lambda_Z = 0$ , and ( $\diamond$ ) $\lambda_\gamma = \lambda_Z$ with $\Delta\kappa_\gamma = \Delta\kappa_Z = 0$ . . . . .	61
4.1	Polarized parton distribution functions. The curves are $x\Delta f(x)$ vs $x$ for parton types $u$ and $d$ , which are the most important partons in our calculations, for two sets of polarized parton distribution functions. The solid curve is the Nadolsky parametrization [38] and the dashed curve is the Gehrman-Stirling parametrization [39]. . . . .	78
4.2	The function $xg_1^p(x, Q)$ , which has been measured experimentally in polarized deep-inelastic lepton scattering, calculated using two sets of polarized parton distribution functions. The solid curve is the Nadolsky parametrization [38] and the dashed curve is the Gehrman-Stirling parametrization [39]. . . . .	79
4.3	Diagram for $u\bar{d} \rightarrow W^+$ . . . . .	81
4.4	Cross-sections $d\sigma(\lambda)/dy_W$ for $p_\lambda + \bar{p} \rightarrow W^+$ in nb, multiplied by $1/9$ , the branching ratio for the $W^+$ to decay to $e^+ + \nu_e$ . Proton polarization $\lambda$ is $L$ or $R$ . The solid and dashed curves are for ppdf's from Ref. [38] and Ref. [39], respectively. . . . .	82
4.5	Cross-sections $d\sigma(\lambda)/dy_W$ for $p_\lambda + \bar{p} \rightarrow W^-$ in nb, multiplied by $1/9$ , the branching ratio for the $W^-$ to decay to $e^- + \bar{\nu}_e$ . Proton polarization $\lambda$ is $L$ or $R$ . The solid and dashed curves are for ppdf's from Ref. [38] and Ref. [39], respectively. . . . .	83
4.6	The left-right polarization asymmetry $\mathcal{A}_{LR}$ for $W^\pm$ production in polarized $p - \bar{p}$ collisions. The solid and dashed curves are for ppdf's from Ref. [38] and Ref. [39], respectively. . . . .	84

4.7	Schematic diagram of particle momentum and spin orientations in $u_L \bar{d}_R \rightarrow W_L^+ \rightarrow e_R^+ \nu_L$ . Single arrows indicate momentum directions; double arrows indicate spin orientation. For clarity the $\bar{d}$ and $e^+$ momenta are shown at angles to the other particles', but they should be imagined as along the same line. . . . .	87
4.8	Cross-sections $d\sigma(\lambda)/dy_e$ for $p_\lambda + \bar{p} \rightarrow W^+ \rightarrow e^+ + \nu_e$ in nb, with proton polarization $\lambda = L$ or $R$ . The solid and dashed curves, labeled (a) and (b), are for ppdf's from Ref. [38] and Ref. [39], respectively. .	88
4.9	Cross-sections $d\sigma(\lambda)/dy_e$ for $p_\lambda + \bar{p} \rightarrow W^- \rightarrow e^- + \bar{\nu}_e$ in nb, with proton polarization $\lambda = L$ or $R$ . The solid and dashed curves labeled (a) and (b), are for ppdf's from Ref. [38] and Ref. [39], respectively. .	88
4.10	The left-right polarization asymmetry $\mathcal{A}_{LR}(e)$ for $W^\pm$ production in polarized $p - \bar{p}$ collisions, with decay $W^\pm \rightarrow e^\pm + \bar{\nu}_e^{(\prime)}$ . The solid and dashed curves, labeled (a) and (b), are for ppdf's from Ref. [38] and Ref. [39], respectively. . . . .	89
4.11	Cross-sections $d\sigma(\lambda)/dy_e$ for $p_\lambda + \bar{p} \rightarrow W^+ \rightarrow e^+ + \nu_e$ in nb, with a kinematic cut on the lepton transverse momentum, $p_{Te} > 25$ GeV. The solid and dashed curves, labeled (a) and (b), are for ppdf's from Ref. [38] and Ref. [39], respectively. . . . .	90
4.12	Cross-sections $d\sigma(\lambda)/dy_e$ for $p_\lambda + \bar{p} \rightarrow W^- \rightarrow e^- + \bar{\nu}_e$ in nb, with a kinematic cut on the lepton transverse momentum, $p_{Te} > 25$ GeV. The solid and dashed curves labeled (a) and (b), are for ppdf's from Ref. [38] and Ref. [39], respectively. . . . .	91

4.13	The left-right polarization asymmetry $\mathcal{A}_{LR}(e)$ for $W^\pm$ production in polarized $p - \bar{p}$ collisions, with decay $W^\pm \rightarrow e^\pm + \bar{\nu}_e^{(-)}$ , with a kinematic cut on the lepton transverse momentum, $p_{Te} > 25$ GeV. The solid and dashed curves, labeled (a) and (b), are for ppdf's from Ref. [38] and Ref. [39], respectively. . . . .	92
5.1	Differential cross-section $d\sigma/d\cos\theta$ for $e_R^- e^+ \rightarrow \chi_1^0 \chi_1^0$ , where $\theta$ is the angle of a neutralino, at $\sqrt{s} = 500$ GeV. The mixing angle $\alpha$ is 0, and the masses are $m_{\chi_1^0} = 100$ GeV, $m_{\tilde{e}_R} = 300$ GeV (solid curve), and $m_{\chi_1^0} = 200$ GeV, $m_{\tilde{e}_R} = 600$ GeV (dashed curve). . . . .	107
5.2	Range of parameters $M_{susy}$ and $m_{\chi_1^0}$ accessible at the NLC. We allow $M_{susy}$ to vary from $10^4$ to $10^7$ GeV. The shaded region is the range of $M_{susy}$ and $m_{\chi_1^0}$ for which $D < 1$ m and $\sigma > 0.2$ fb, where $D$ is the typical decay length of $\chi_1^0$ and $\sigma$ is the production cross-section for $e_R^- e^+ \rightarrow \chi_1^0 \chi_1^0$ at the NLC. The bound $\sigma > 0.2$ fb is equivalent to observing more than 10 events assuming integrated luminosity $50 \text{ fb}^{-1}$ . The cross-shaded region is for $10 \text{ cm} < D < 1$ m, corresponding to the background-free signal process. Parameter values for this plot are $\alpha = 0$ and $m_{\tilde{e}_R} = 300$ GeV. . . . .	110
5.3	Differential cross-section in photon energy $d\sigma/dE_\gamma$ for $e_R^- e^+ \rightarrow \chi_1^0 \chi_1^0 \rightarrow \gamma\gamma\tilde{G}\tilde{G}$ at the NLC, assuming $\alpha = 0$ . The mass parameter values are $m_{\chi_1^0} = 100$ GeV and $m_{\tilde{e}_R} = 300$ GeV. (The normalization of $d\sigma/dE_\gamma$ is such that the integral over $E_\gamma$ is 2 times the total cross-section, because the final state has identical photons.) . . . . .	111
5.4	Same as Fig. 5.2, but with a more precise calculation as described in Section 5.3.3. . . . .	115

- 5.5 Differential cross-section in photon transverse momentum  $d\sigma/dp_T^\gamma$  for  $e_R^-e^+ \rightarrow \chi_1^0\chi_1^0 \rightarrow \gamma\gamma\tilde{G}\tilde{G}$  at the NLC, assuming  $\alpha = 0$ . The mass parameter values are  $m_{\chi_1^0} = 100$  GeV and  $m_{\tilde{e}_R} = 300$  GeV. (The normalization of  $d\sigma/dp_T^\gamma$  is such that the integral over  $p_T^\gamma$  is 2 times the total cross-section, because the final state has identical photons.) 117
- 5.6 Differential cross-section in the sum of photon energies  $d\sigma/d(E_{\gamma_1} + E_{\gamma_2})$  for  $e_R^-e^+ \rightarrow \chi_1^0\chi_1^0 \rightarrow \gamma\gamma\tilde{G}\tilde{G}$  at the NLC, assuming  $\alpha = 0$ . The mass parameter values are  $m_{\chi_1^0} = 100$  GeV and  $m_{\tilde{e}_R} = 300$  GeV. . . 118
- 5.7 Differential cross-section  $d\sigma/dM_{inv}$  in the invariant mass of invisible particles  $M_{inv}$  for the signal process  $e_R^-e^+ \rightarrow \chi_1^0\chi_1^0 \rightarrow \gamma\gamma\tilde{G}\tilde{G}$ , and for the background process  $e_R^-e^+ \rightarrow \gamma\gamma Z$ , with decay  $Z \rightarrow \nu\bar{\nu}$ . The photon transverse momenta are required to be greater than 20 GeV. The masses for the signal process are  $m_{\chi_1^0} = 200$  GeV and  $m_{\tilde{e}_R} = 600$  GeV. . . . . 119
- 5.8 Total cross-section at the NLC for the process  $e_R^-e^+ \rightarrow \chi_1^0\chi_1^0$  with  $\alpha = 0$ , as a function of  $m_{\chi_1^0}$  for  $m_{\tilde{e}_R} = 300$  GeV (solid curve),  $m_{\tilde{e}_R} = 100$  GeV (dashed curve), and  $m_{\tilde{e}_R} = 600$  GeV (dot dashed curve). (Note that only  $m_{\chi_1^0} < m_{\tilde{e}_R}$  is allowed in the models we consider because  $\chi_1^0$  is the NLSP.) . . . . . 120
- 5.9 Total cross-section for the process  $e_R^-e^+ \rightarrow \chi_1^0\chi_1^0$  with  $\alpha = 0$ , as a function of  $\sqrt{S}$ . The mass parameter values are  $m_{\chi_1^0} = 100$  GeV,  $m_{\tilde{e}_R} = 300$  GeV (solid curve), and  $m_{\chi_1^0} = 200$  GeV,  $m_{\tilde{e}_R} = 600$  GeV (dashed curve). . . . . 122

5.10	Range of parameters $M_{susy}$ and $m_{\chi_1^0}$ accessible at the NLC with $\sqrt{s} = 500$ GeV (solid line), 1 TeV (dashed line), and 1.5 TeV (dot-dash line). The luminosity per year is 50, 200 and 200 fb <sup>-1</sup> , respectively. Mass parameter values are $m_{\tilde{e}_R} = 300$ GeV, 500 GeV and 750 GeV, respectively, and the mixing angle $\alpha$ is 0. The interior of each triangle is the region where the number of events is greater than 10, and $D < 1$ m. . . . .	123
5.11	Range of parameters $M_{susy}$ and $m_{\chi_1^0}$ accessible at the NLC (solid line), LEP/SLC (dashed line), and LEP-II (dot-dash line). The interior of each triangle is the region where the number of events is greater than 10, and $D < 1$ m. Parameter values for this plot are $\alpha = 0$ and $m_{\tilde{e}_R} = 300$ GeV. . . . .	124
B.1	(a) The $WW\gamma$ vertex. (b) Example diagram for $u\bar{d} \rightarrow W^+\gamma \rightarrow e^+\nu\gamma$ . Arrows indicate the defined momentum direction. . . . .	135

# Chapter 1

## Introduction

The field denotes  
this body, and wise men  
call one who knows it  
the field-knower.

Know me as the field-knower  
in all fields—what I deem  
to be knowledge is knowledge  
of the field and its knower.

Lord Krishna, *Bhagavad Gita*

### 1.1 The Standard Model

The Standard Model (SM) describes the interactions of the most fundamental known particles in nature. The SM is a quantum field theory [1], which means that the particles detected in scattering experiments are represented by locally interacting quantum fields. The Lagrangian of such a theory is specified by a list of its

constituent fields and its symmetries. A symmetry is an invariance of the Lagrangian under a group of transformations of the fields. The SM Lagrangian is invariant under “gauge,” or local, transformations corresponding to the group

$$SU(3)_C \times SU(2)_L \times U(1)_Y,$$

where  $SU(N)$  can be represented by the group of unitary complex  $N \times N$  matrices with determinant one, while a  $U(1)$  transformation is equivalent to multiplication by a complex phase.

### 1.1.1 Quantum Chromodynamics

The subscript C on the  $SU(3)$  group refers to the quantum number associated with this group, which is called color. Because it governs the interactions of colored particles, this sector of the Standard model is known as Quantum Chromodynamics (QCD). The fundamental colored matter particles (fermions) are called quarks. Each quark field comes in three colors, so the quarks are represented by  $SU(3)$  triplets. There are six of these color-triplet fields, labelled by their “flavor”: up, down, strange, charm, top, and bottom. The matter fields and the gauge group determine the gauge bosons. The QCD gauge bosons are called gluons because they hold together the quarks which make up protons and neutrons. They fall into the adjoint representation of  $SU(3)$ , which includes eight independent color states.

QCD has the property that only color-singlet states can be isolated and observed: quarks or gluons are “confined” within color-singlet bound states, hadrons, which are the observed strongly interacting particles. The observational consequence of confinement is that when a scattering process produces quarks or gluons in the final state, these will “hadronize” to be observed as “jets” of hadrons.

## 1.1.2 The Electroweak Sector

The  $SU(2)_L \times U(1)_Y$  sector is called the electroweak theory [2]. These two groups are lumped together because their product group is broken down to  $U(1)_{EM}$  by the Higgs mechanism, which will be discussed in section 1.1.3. The subscript L means that only *left-handed* fermion fields couple to the  $SU(2)$  gauge bosons. The Lorentz character of the interaction vertex is vector minus axial vector, or  $V - A$ ; this combination projects out the left-handed component of a fermion.<sup>†</sup> The left-handed fermions, including quarks (color triplets) and leptons (color singlets, or “colorless”) fall into doublets; while the right-handed fields are represented by  $SU(2)$  singlets, which do not interact with the  $SU(2)$  bosons. The upper and lower components of an  $SU(2)_L$  doublet are distinguished by their flavor name, or mathematically by the third component of the “weak isospin” quantum number,  $I_3$ .  $I_3 = \pm\frac{1}{2}$  for the upper and lower components, respectively. The gauge field is again in the adjoint representation, so it has three components, called  $W_1^\mu$ ,  $W_2^\mu$ , and  $W_3^\mu$ .

The  $U(1)_Y$  quantum number is called weak hypercharge, denoted by  $Y$ . The  $U(1)_Y$  gauge field is denoted by  $B^\mu$ . The values of the weak hypercharge are chosen to satisfy a relation with  $I_3$  and the electromagnetic charge  $Q$  (in units of  $e$ ):

$$Y = 2(Q - I_3).$$

## 1.1.3 The Higgs Sector

With the inclusion of quarks, leptons, and gauge bosons as outlined above, we can write down a gauge invariant Lagrangian. However, mass terms for any of these fields, of the generic form  $m^2\Phi^\dagger\Phi$ , would not be invariant under a SM gauge transformation. As the corresponding particles are known experimentally to be

---

<sup>†</sup>This statement is strictly true only for massless fermions. Throughout this thesis quarks and leptons will be approximated as massless. This approximation is good at the collider energies we will be considering, because  $E \gg mc^2$ .

massive, the theory described so far is unacceptable. While the dynamics of the theory, codified in the Lagrangian, respects the SM symmetry, the fields that we would like to call fundamental are found in Nature to be massive, so they do not respect the symmetry.

The SM solution to this problem is called the Higgs mechanism [3]. The general strategy is to associate the gauge non-invariant physics with the ground or vacuum state, and retain the invariance of the Lagrangian. When the ground state of a system does not possess the full symmetry of the system's Lagrangian, the symmetry is said to be "hidden" or "spontaneously broken."

We postulate a complex scalar field, called the Higgs field  $\Phi$ , which is an  $SU(2)$  doublet; and we postulate a Higgs potential that forces the field to have a non-zero vacuum expectation value (vev), thereby breaking the  $SU(2)_L \times U(1)_Y$  symmetry. We may perform a gauge transformation on the Higgs doublet which eliminates three of its four degrees of freedom, so that the Higgs field can be written in terms of its vev and one real field. When we transform the Higgs field we must make the corresponding transformation of the gauge fields. When the Lagrangian is rewritten in terms of these transformed fields, we find that mass terms have appeared for three of the gauge bosons, and the mass is related to the vev of the Higgs field. In the argot, one says that the Nambu-Goldstone boson degrees of freedom have been "eaten" by the gauge bosons to acquire their mass.

The SM symmetry of the original Lagrangian is "hidden" by the Higgs' dynamics, but our transformed Lagrangian respects a residual  $U(1)$  symmetry, called the  $U(1)_{EM}$ . We require the gauge boson associated with this unbroken symmetry to be massless, which identifies it as the photon,  $A_\mu$ , and fixes the physical combinations of the fundamental fields, the  $W_\mu^\pm$  and  $Z_\mu^0$ . This physical SM Lagrangian is shown in Appendix A.

### 1.1.4 Generations, the CKM Matrix, and CP violation

We now have an economical description of massive gauge fields interacting with fermion matter fields, but Nature is not so simple. There are three copies of each fermion field which differ only in mass. In addition to the electron field there are muon and tau fields with the same quantum numbers as the electron, except that they are orders of magnitude more massive. Similarly, the  $SU(2)_L$  doublet of up and down quarks is supplemented by the heavier charm-strange doublet and heaviest, the top-bottom doublet. Each of the three sets of fields is called a “generation,” or “family,” while a specific field within a generation is identified by its “flavor.”

To complicate matters further, the eigenstates of the interaction Lagrangian for these various flavors of fields are not equal to the mass eigenstates observed in scattering experiments. This means that mixing among the generations is present. The mixing can be parametrized by three angles and a complex phase arranged in a  $3 \times 3$  matrix in generation space, called the Cabbibo-Kobayashi-Maskawa (CKM) matrix [4]. It turns out that we can relegate all the mixing to affect only the  $I_3 = -\frac{1}{2}$  quarks; the lepton mass eigenstates are equal to their interaction eigenstates. An important experimentally verified prediction of this formalism is the absence of flavour-changing neutral currents at “tree level,” the leading order of perturbation theory. For example, a charm quark very rarely decays to an up quark.

Experiments with the decay of K mesons, containing strange flavor quarks, show that the weak interactions are not invariant under combined charge-conjugation (C) and parity (P) transformations. The complex phase in the CKM matrix provides a convenient parametrization of CP violation, because CP invariance requires that  $M_{CKM}^* = M_{CKM}$ . (However, it is not yet known whether CP violation in the Standard Model is *solely* due to this complex phase in the CKM matrix.)

In this thesis we will neglect the CKM mixing, as the CKM matrix is near enough to the identity for our calculation.

### 1.1.5 Summary of the Standard Model

The SM identifies the constituents of matter as a set of interacting boson and fermion fields. The Lagrangian postulated to describe their dynamics is invariant under a set of transformations corresponding to the group  $SU(3)_C \times SU(2)_L \times U(1)_Y$ . The ground state, or vacuum, of this system of fields does *not* respect the SM symmetry. The non-zero vev of the Higgs field leads to a set of effective, or physical fields, including massive vector bosons.

The fermions of the SM are the quarks and leptons. The quarks are “colored,” because they transform as triplets under an  $SU(3)_C$  transformation. The left-handed quarks are also doublets under  $SU(2)_L$ , while the right-handed quark fields are  $SU(2)_L$  singlets. The leptons are color singlets and again the left-handed leptons are  $SU(2)_L$  doublets, while the right-handed leptons are singlets. There are three generations of quarks and leptons differing only in mass; the CKM matrix parametrizes the mixing between generations.

The bosons of the SM are the vector gauge bosons and the scalar Higgs boson. The Higgs is a colorless  $SU(2)_L$  doublet. The mediators of the color interaction are the  $SU(3)_C$  octet gluons, which are  $SU(2)_L$  singlets. The physical electro-weak bosons are the massive  $W^\pm, Z^0$ , and the massless photon  $A$ . They are linear combinations of the  $SU(2)_L \times U(1)_Y$  gauge bosons, which transform under the adjoint representation of their respective simple groups.

This set of fields along with the dynamics specified by the Lagrangian has been adequate thus far to account for the results of high-energy scattering experiments, although precision tests are under way to test for deviation from the SM. Despite

its phenomenological success, there are reasons to believe that the SM is not a complete theory of elementary particles. For one, the gauge groups and parameters of the SM appear arbitrary. Also, the equality of the magnitudes of the proton and electron charges is unexplained unless the SM gauge groups are unified into a larger simple group such as  $SU(5)$ . Furthermore, the gravitational interaction is not included in the theory. It may also be argued that the technical “triviality” of the Standard Higgs sector implies that the model is only valid below some cut-off energy scale [5]. In other words, the SM must be considered an effective—as opposed to a fundamental—theory. However, like the periodic table of elements, the Standard Model will continue to provide an accurate and economical description of the phenomena in its domain.

## 1.2 Triple-Boson Couplings

Because the generators of the Standard model gauge group do not commute, the gauge bosons must interact among themselves to preserve gauge invariance. The form and strength of these interactions are fixed by the gauge invariance, so the measurement of the triple-boson coupling parameters is an important test of the Standard Model.

In part I of this work we will focus on the electroweak triple-boson couplings. In particular, we would like to determine experimentally values of the  $WW\gamma$  and  $WWZ$  couplings. Let  $W^{\pm\mu}(x)$ ,  $Z^\mu(x)$ , and  $A^\mu(x)$  denote the fields of  $W^\pm$ ,  $Z^0$ , and  $\gamma$ ; then the interaction Lagrangian we consider is

$$\begin{aligned} \mathcal{L}_3 = & -ig(W_{\mu\nu}^+ W^{-\mu} - W_{\mu\nu}^- W^{+\mu})(A^\nu \sin \theta_W + Z^\nu \cos \theta_W) \\ & -igW_\mu^+ W_\nu^- (A^{\mu\nu} \kappa_\gamma \sin \theta_W + Z^{\mu\nu} \kappa_Z \cos \theta_W) \\ & -\frac{ig}{M_W^2} W_{\mu\alpha}^+ W_\nu^{-\alpha} (A^{\mu\nu} \lambda_\gamma \sin \theta_W + Z^{\mu\nu} \lambda_Z \cos \theta_W) \end{aligned} \quad (1.1)$$

where  $A_{\mu\nu} = \partial_\mu A_\nu - \partial_\nu A_\mu$ , etc.  $\mathcal{L}_3$  is CP invariant, and gauge invariant with respect to  $U(1)_{EM}$  electromagnetic gauge transformations.

The parameters  $\kappa_\gamma$  and  $\lambda_\gamma$  are related to the anomalous magnetic moment ( $\mu_W$ ) and anomalous electric quadrupole moment ( $Q_W$ ) of the  $W^-$ , as follows [6]:

$$\mu_W = \frac{e}{2M_W}(1 + \kappa_\gamma + \lambda_\gamma),$$

$$Q_W = \frac{-e}{M_W^2}(\kappa_\gamma - \lambda_\gamma).$$

The parameters  $\kappa_Z$  and  $\lambda_Z$  are similar  $WWZ$  couplings. In the Standard  $SU(2) \times U(1)$  gauge theory these coupling parameters have the definite values

$$\kappa_\gamma = \kappa_Z = 1, \quad \lambda_\gamma = \lambda_Z = 0 \quad (\text{Standard Model}).$$

We define  $\Delta\kappa$  by

$$\Delta\kappa = \kappa - 1.$$

If  $\Delta\kappa$  or  $\lambda$  is significantly different than 0 for either  $\gamma$  or  $Z^0$ , then the Standard  $SU(2) \times U(1)$  gauge theory is not the complete theory of the electroweak interactions.

We can check that the SM Lagrangian from the appendix reproduces  $\mathcal{L}_3$  with  $\Delta\kappa$  and  $\lambda$  both zero. From Appendix A, the SM electroweak triple-boson interactions are included in:

$$\begin{aligned} \mathcal{L}_{eff}(SM) = & - \frac{1}{2} |\bar{D}_\mu W_\nu^+ - \bar{D}_\nu W_\mu^+|^2 \\ & - \frac{i}{2} [g \cos \theta_W Z_{\mu\nu}^0 + e A_{\mu\nu}] (W^{+\mu} W^{-\nu} - W^{-\mu} W^{+\nu}). \end{aligned}$$

The second line is equal to the second line of  $\mathcal{L}_3$ , because the symmetric part of  $W^{+\mu} W^{-\nu}$  contracted with the antisymmetric field tensors vanishes; and because  $e = g \sin \theta_W$ . To expand the first line and show that it includes the first line of  $\mathcal{L}_3$  above, recall that

$$\bar{D}_\mu \equiv \partial_\mu + ig(Z_\mu^0 \cos \theta_W + A_\mu \sin \theta_W).$$

Then the terms cubic in the vector fields are

$$\begin{aligned}
 & igW_{\mu\nu}^+ [(Z^{0,\mu} \cos \theta_W + A^\mu \sin \theta_W)W^{-\nu} - (Z^{0,\nu} \cos \theta_W + A^\nu \sin \theta_W)W^{-\mu}] \\
 & - igW_{\mu\nu}^- [(Z^{0,\mu} \cos \theta_W + A^\mu \sin \theta_W)W^{+\nu} - (Z^{0,\nu} \cos \theta_W + A^\nu \sin \theta_W)W^{+\mu}].
 \end{aligned}$$

Again, since the tensor  $W_{\mu\nu}$  is antisymmetric, when it is contracted with any other tensor only the antisymmetric part will survive; so we may replace the terms in brackets, giving finally

$$-ig(W_{\mu\nu}^+ W^{-\mu} - W_{\mu\nu}^- W^{+\mu})(A^\nu \sin \theta_W + Z^\nu \cos \theta_W),$$

as claimed.

In the Standard Model,  $\Delta\kappa$  and  $\lambda$  can be induced at loop level, but only of the size of  $\mathcal{O}(g^2/16\pi^2) \approx 0.003$  at one-loop level from naive dimensional analysis [7]. Thus setting stringent experimental limits on the anomalous  $WW\gamma$  or  $WWZ$  couplings is an important test of the Standard Model; actually discovering large anomalous interactions would be a sign of new physics. We treat  $\mathcal{L}_3$  as an effective Lagrangian and only use it for tree-level calculations.

To determine the  $WWV$  couplings (where  $V$  stands for  $\gamma$  or  $Z^0$ ) it is necessary to measure the experimental cross-section, or the distribution of some kinematic variable, for a scattering process that depends on the  $WWV$  coupling, and compare the measurement to a calculated prediction. In subsequent chapters we will consider a few processes to estimate their sensitivities to the  $WWV$  couplings.

Current (95% confidence) limits on  $\Delta\kappa$  and  $\lambda$  from  $p\bar{p} \rightarrow W\gamma, WW, WZ$  at Fermilab, as reported in References [8] – [12] are shown in Table 1.1. The limits on individual anomalous couplings were calculated assuming the other anomalous couplings were zero.

Because the anomalous triple-boson amplitudes increase with energy as  $s/M_W^2$ , to preserve the unitarity of the amplitudes these analyses were performed treating

Table 1.1: Current 95% C.L. limits on anomalous couplings from direct cross section measurements. A subscript  $\gamma, Z$  indicates that the photon and Z anomalous couplings were assumed equal. All couplings but those being limited were fixed at their SM values. All entries shown were calculated with  $\Lambda = 1.5$  TeV, except the last, from Reference [12], for which  $\Lambda = 1.0$  TeV.

Experiment/Luminosity	Process $p\bar{p} \rightarrow$	Ref.	Limits
D $\emptyset$ 13.8pb $^{-1}$	$l\nu\gamma(l = e, \mu)$	[8]	$-1.6 < \Delta\kappa_\gamma < 1.8$ $-0.6 < \lambda_\gamma < 0.6$
D $\emptyset$ 96 pb $^{-1}$	$e\nu jjX$	[9]	$-0.47 < \Delta\kappa_{\gamma,Z} < 0.63$ $-0.36 < \lambda_{\gamma,Z} < 0.39$ $-1.38 < \Delta\kappa_\gamma < 1.70$ $-1.21 < \lambda_\gamma < 1.25$ $-0.60 < \Delta\kappa_Z < 0.79$ $-0.40 < \lambda_Z < 0.43$
D $\emptyset$ 13.8pb $^{-1}$	$W_\gamma, WZ, WW$ Combined	[10]	$-1.38 < \Delta\kappa_{\gamma,Z} < 1.70$ $-0.44 < \lambda_{\gamma,Z} < 0.44$
CDF 19.6pb $^{-1}$	$l\nu\gamma(l = e, \mu)$	[11]	$-2.3 < \Delta\kappa_\gamma < 2.2$ $-0.7 < \lambda_\gamma < 0.7$
CDF 19.6pb $^{-1}$	$l\nu jj$	[12]	$-0.89 < \Delta\kappa_{\gamma,Z} < 1.27$ $-0.81 < \lambda_{\gamma,Z} < 0.84$

the anomalous coupling parameters as “dipole” form factors. For example,

$$\Delta\kappa(s) = \frac{\Delta\kappa}{(1 + s/\Lambda^2)^2}, \quad (1.2)$$

with a similar expression for  $\lambda$ .  $\Lambda$  may be interpreted as the energy scale of non-Standard gauge boson dynamics. Both Tevatron detector collaborations found that for sufficiently large  $\Lambda$ , above about 200 GeV, the limits on non-Standard couplings are relatively insensitive to  $\Lambda$ . In this thesis we treat the anomalous couplings as point couplings, independent of  $s$ . That is, we set  $\Delta\kappa(s) = \Delta\kappa$ , which is valid at energy scales much smaller than  $\Lambda$ . This approximation causes our estimates of bounds on anomalous couplings to be more stringent than those calculated including the form factor behavior. Low energy values of anomalous couplings provide a lower limit on  $\Lambda$  of order 1 TeV [13]. In the worst case, if  $\Lambda \approx 1$  TeV, our NLC limits ( $\sqrt{s} = 500$  GeV) would be about 35% smaller than those calculated using form factor couplings.

The fact that the anomalous vertices violate unitarity at high energies can actually be used to derive limits on the couplings. The authors of Reference [14] find for  $\Lambda^\ddagger$  greater than about 1 TeV,

$$\begin{aligned} |\Delta\kappa_\gamma| &< \frac{1.86}{\Lambda^2}, & |\Delta\kappa_Z| &< \frac{0.85}{\Lambda^2}, \\ |\lambda_\gamma| &< \frac{0.99}{\Lambda^2}, & |\lambda_Z| &< \frac{0.54}{\Lambda^2}, \end{aligned} \quad (1.3)$$

with  $\Lambda$  in TeV. To compare these unitarity bounds to the bounds obtainable from direct cross section measurements, we anticipate a result of Chapter 2, namely that the Next Linear Collider (NLC) could probe anomalous couplings of order 0.01. Therefore, direct experimental cross section measurements will set stronger limits on anomalous couplings than these unitarity bounds, unless  $\Lambda$  is greater than order

---

<sup>‡</sup>The definition of  $\Lambda$  in Ref. [14] is not identical to Eq. (1.2), but the interpretation as the scale of new triple-boson dynamics is the same.

10 TeV. Inversely, if  $\Lambda$  is greater than 10 TeV, the unitarity bounds imply that we could not observe anomalous couplings at the NLC.

One can also derive limits on anomalous couplings by an analysis of precision (loop-level) electroweak measurements [15]. A DPF study [16] reports that a global fit of electroweak data, including for example measurements of lepton gyromagnetic ratios and electric dipole moments, yields the following  $1\sigma$  (68 % C.L.) constraints,

$$\begin{aligned}\Delta\kappa_\gamma &= 0.056 \pm 0.056 \\ \Delta\kappa_Z &= -0.0019 \pm 0.044 \\ \lambda_\gamma &= -0.036 \pm 0.034 \\ \lambda_Z &= 0.049 \pm 0.045,\end{aligned}\tag{1.4}$$

assuming that only one anomalous coupling varies at a time. The authors of [16] consider it unlikely that non-Standard physics will only produce one anomalous triple-boson vertex. They emphasize that these bounds disappear if the couplings are allowed to vary simultaneously, due to the possibility of cancellations among the couplings. In this case one is left with limits of order 1 from precision electroweak measurements. Furthermore, the authors of [14] caution that bounds such as these, which make use of loop calculations, "should be taken with a grain of salt," because of ambiguities inherent in calculating loop effects in non-gauge models. They point out that if one only analyzes unambiguous low-energy quantities, like  $(g-2)_\mu$ , the resulting bounds are again only of order 1. (Reference [17] discusses bounds from  $(g-2)_\mu$  and from the precision measurement of the  $Z \rightarrow b\bar{b}$  branching ratio at LEP II and BNL.) We conclude that possible bounds on anomalous couplings from direct experimental cross section measurements are worth investigating; Part I of this thesis is devoted to calculating these bounds at a few particle colliders.

### 1.3 Beam Polarization

Polarizing one or both incoming beams longitudinally in a collider experiment can enhance the precision of studies of parity non-conserving physics, or reduce parity non-conserving background processes. Because the electroweak interaction violates parity conservation (e.g. the  $W$  couples only to left-handed fields), electroweak processes are the SM processes most sensitive to polarization.

Experimenters can potentially use this fact in two ways. To study an electroweak process, a polarized beam would allow the experimenter to choose the polarization with the higher cross section and greater event rate. On the other hand, to study a parity-conserving process with an electroweak background, the polarization which minimizes the background may be chosen. As an example consider single  $W$  production from  $e^+e^-$  annihilation, where we may polarize the electron to be right or left-handed. Because the  $W$  coupling to fermions is pure left-handed, we will see no  $W$ 's from a right-handed electron beam. Now, the unpolarized cross section is the average of the two polarized cross sections. Therefore, if we choose the left polarization, the polarized cross section will be twice the unpolarized cross section. This will be true of any process for which the diagrams involve a  $W$  line connected to a massless initial fermion.

The calculation of polarized cross sections is straightforward in terms of helicity amplitudes. The helicity eigenstates are definite polarization states of the initial elementary fermions. At an  $e^+e^-$  collider this means we simply include the helicity amplitudes corresponding to the chosen polarization. At a  $p\bar{p}$  collider, we may polarize the initial hadron; however, since we can only calculate amplitudes involving the elementary fields of the SM, *i.e.* “partons” within the proton, therefore to relate the polarization of the beam to the helicity of the interacting constituent “partons” from the proton, we will need to make use of polarized parton distribution functions

(pdf's), which give the probability to find a gluon or quark in a polarized proton. These functions will be introduced in Chapter 3.

## 1.4 The Organization of This Thesis

Part I of this thesis is concerned with comparing the sensitivities of various collider experiments to anomalous electroweak triple-boson vertices. In Chapter 2 we will estimate these sensitivities at two  $e^+e^-$  colliders. The purpose of Chapter 3 is to determine to what extent polarizing a  $p\bar{p}$  collider, the Fermilab Tevatron, can enhance its sensitivity to anomalous couplings. In Chapter 3 the importance of the polarized parton distribution functions will become apparent. Chapter 4 examines how these might be constrained by studying single  $W$  production at a polarized  $p\bar{p}$  collider.

Part II of this thesis deals with supersymmetry (SUSY). After a brief introduction to SUSY, we explore the phenomenology of a very light “gravitino” particle, which arises in certain mechanisms of SUSY-breaking. The role of polarization in this part will be to eliminate a background process.

# **Part I**

## **Anomalous Electroweak Triple-Boson Couplings**

# Chapter 2

## Probing Anomalous Triple-Boson Couplings with $e^-e^+ \rightarrow W^-W^+$

### 2.1 Introduction

Processes which produce electroweak bosons offer the most obvious testing ground for the triple-boson vertices. We will focus here on  $W$  pair production, as it is simple to calculate and has a relatively large cross-section. In part I of this work we are interested in the potential of beam polarization for improving sensitivities to triple-boson couplings. The Tevatron, with center of mass energy  $\sqrt{s} \simeq 2$  TeV, is the existing collider with sufficient energy to produce a  $W$  pair. Before turning to the  $p\bar{p}$  collider calculation, we consider production of a pair of  $W$ 's from  $e^-e^+$  collisions at LEP II and at the proposed Next Linear Collider (NLC). This calculation will be somewhat simpler than the  $p\bar{p}$  calculation, so the analysis may be more transparent.

The authors of [18] estimated the sensitivity of LEP II to anomalous triple-boson couplings through  $W$  pair production, without explicitly calculating the decay of the  $W$ 's. We will reproduce their calculation here, including the decays and realistic cuts, and focusing on one particular anomalous coupling,  $\Delta\kappa_\gamma$ . They assumed for LEP II  $\sqrt{s} = 190$  GeV and a luminosity of  $0.5 \text{ fb}^{-1} \text{ yr}^{-1}$ , as will we. We will not consider the partial polarizability of the LEP beam. The proposed NLC would have  $\sqrt{s} = 0.5$  TeV, very high luminosity ( $50 \text{ fb}^{-1} \text{ yr}^{-1}$ ), and better than 90% polarization

of the electron beam [19]. The authors of [20] estimated the sensitivities to anomalous couplings at the NLC, using a  $\chi^2$  analysis of a triple-differential cross-section. We will instead use a single-differential cross-section, the cosine distribution of the final electron, which was identified in [18] as the most sensitive variable to the anomalous couplings. We will thus be able to directly compare our LEP II and NLC sensitivities. In our NLC calculation we will assume 100% polarization.

In the  $p\bar{p}$  analysis in the next chapter we will use only the total cross-section to calculate limits on the anomalous couplings, because the uncertainties in the polarized parton distribution functions (ppdf's) are incompatible with the precision we would hope to achieve by a  $\chi^2$  fit. For the  $e^+e^-$  case at hand, we will also estimate sensitivities using the  $\chi^2$  statistic to rule out values of anomalous couplings for which the final state electron cosine distribution,  $d\sigma/d\cos\theta_e$ , deviates significantly from the standard model distribution. By comparing the sensitivities from the  $\chi^2$  calculation to those from the total cross-section calculation, we can get an idea of how the sensitivities in the  $p\bar{p}$  case could improve when the ppdf's are better constrained.

A realistic study must include the decay of the  $W$  bosons. Following references [18, 20] we will consider the semi-leptonic decay channel:

$$e^-e^+ \rightarrow W^-W^+ \rightarrow l^-\bar{\nu}q\bar{q}'.$$

The leptons included are  $l = e, \mu$ , and the hadronic decay channel includes  $q = u, c$ . At the NLC we calculate cross-sections with a left-polarized electron beam, and at LEP II we consider the unpolarized process. We choose this decay mode because allowing both  $W$ 's to decay leptonically would reduce the cross-section, whereas the four-jet hadronic mode would have a large QCD background.

### 2.1.1 Calculation

To calculate the cross-sections, we began with the helicity amplitudes corresponding to the Feynman diagrams in Figure 2.1. The definitions of our helicity eigenstates are collected in Appendix B.1. Helicity amplitudes are most convenient in a study involving polarization, as at the NLC, because the helicity amplitudes correspond to definite polarization states. To calculate a polarized cross section, we include only the helicity amplitudes corresponding to the chosen polarization, instead of summing the amplitudes-squared for every helicity.

To calculate a cross-section from the amplitudes, we must integrate the phase space of the process. We perform this integration using a Monte-Carlo event generator based on the VEGAS routine [21]. We store all the simulated events in an HBOOK NTUPLE, from which we can project any differential cross-section.

Figures 2.2 and 2.3 compare the differential cross section in  $W^-$  rapidity<sup>†</sup> of our Monte Carlo calculation to an analytic calculation based on the amplitudes of [18]. The Monte Carlo distribution is uncut at this stage, but includes the  $W$  decay with a narrow width.

The cuts we imposed on the cross-section calculations are shown in Table 2.1.  $\Delta R = \sqrt{(\Delta\phi)^2 + (\Delta\eta)^2}$  is a measure of the separation between two particles, where  $\Delta\phi$  and  $\Delta\eta$  are their separations in azimuthal angle and rapidity, respectively. Requiring  $\Delta R$  to be greater than 0.7 ensures that after a final parton showers into a jet it will still be distinguishable experimentally from the other final state particles. The cuts on  $\Delta R$  and on the absolute value of rapidity are imposed on all final state particles except for the neutrino. The cut on transverse momentum ( $P_T$ ) is imposed

---

<sup>†</sup>Rapidity  $y$  is a measure of polar angle defined by  $y \equiv \frac{1}{2} \ln \frac{E+P_z}{E-P_z}$ , where  $P_z = P \cos \theta$ ,  $\theta$  being the angle from the  $z$ -axis. The  $z$ -axis is defined to point in the direction of the proton beam at  $p\bar{p}$  colliders, and the electron beam at  $e^+e^-$  colliders. Zero rapidity corresponds to the “central”  $\theta = 90$  region; large positive or negative rapidity approaches  $\theta = 0$  or  $\theta = 180$  degrees, respectively. (Throughout this thesis  $c$  and  $\hbar$  are set equal to 1.)

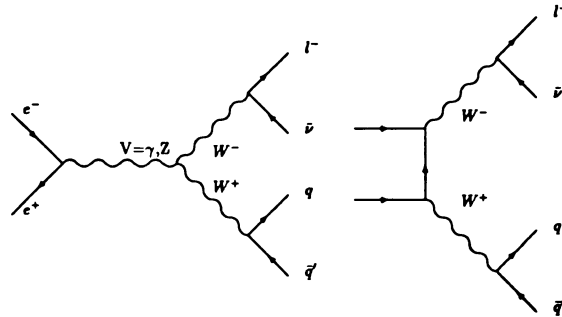


Figure 2.1: Diagrams for  $e^-e^+ \rightarrow W^-W^+ \rightarrow l^-\bar{\nu}q\bar{q}'$

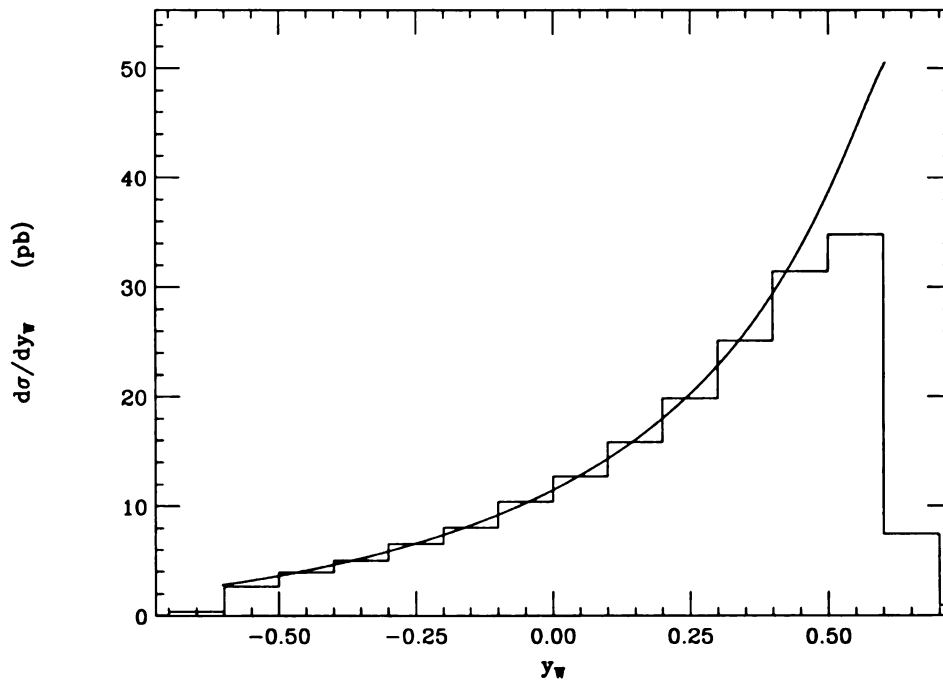


Figure 2.2: Rapidity distributions of the  $W^-$  at LEP II from analytic amplitudes (smooth) and uncut Monte Carlo calculation (histogram).

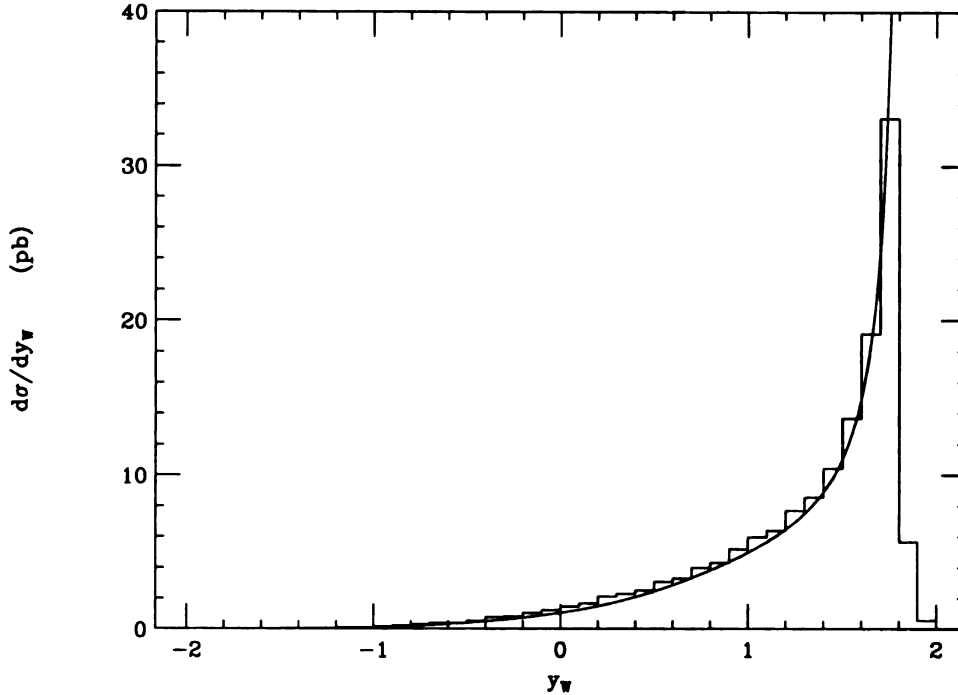


Figure 2.3: Rapidity distributions of the  $W^-$  at NLC from analytic amplitudes of (smooth) and uncut Monte Carlo calculation (histogram).

Table 2.1: Final state cuts.

	LEP II	NLC
Minimum $P_T$	10 GeV	20 GeV
Maximum Rapidity	1.5	1.5
Minimum $\Delta R$	0.7	0.7

on all final state particles.

Although these cuts reduce the total number of events, they enhance the dependence of the cross section on anomalous couplings. Figure 2.4 shows the rapidity distribution of the final electron at LEP II for the SM and for  $\Delta\kappa_\gamma = 0.5$ , without cuts. Where the cross section is large, at high rapidities, the dependence on anomalous coupling is small. The largest deviation from the SM occurs at low and central rapidities, where the cross section is smaller. This means that when we cut out events with high  $|y_e|$ , we cut out mostly events from the region with weak dependence on anomalous couplings. Furthermore, since the effect of anomalous

couplings increases with energy, the low  $P_T$  region, which we cut out, is less sensitive than the high  $p_t$  region. Figure 2.5 shows the electron rapidity distributions after implementing the cuts of Table 2.1. Still, the cuts we chose are probably not optimal, so perhaps the limits we find could be improved somewhat.

With these cuts, the total SM cross section is 3.43 picobarns at LEP II, and 0.66 pb at the NLC (with left polarized electron beam). The total cross section as a function of anomalous photon couplings is shown in Figures 2.6 and 2.7. This dependence of the cross section on anomalous coupling will allow us to rule out couplings for which the cross section is significantly different from the SM.

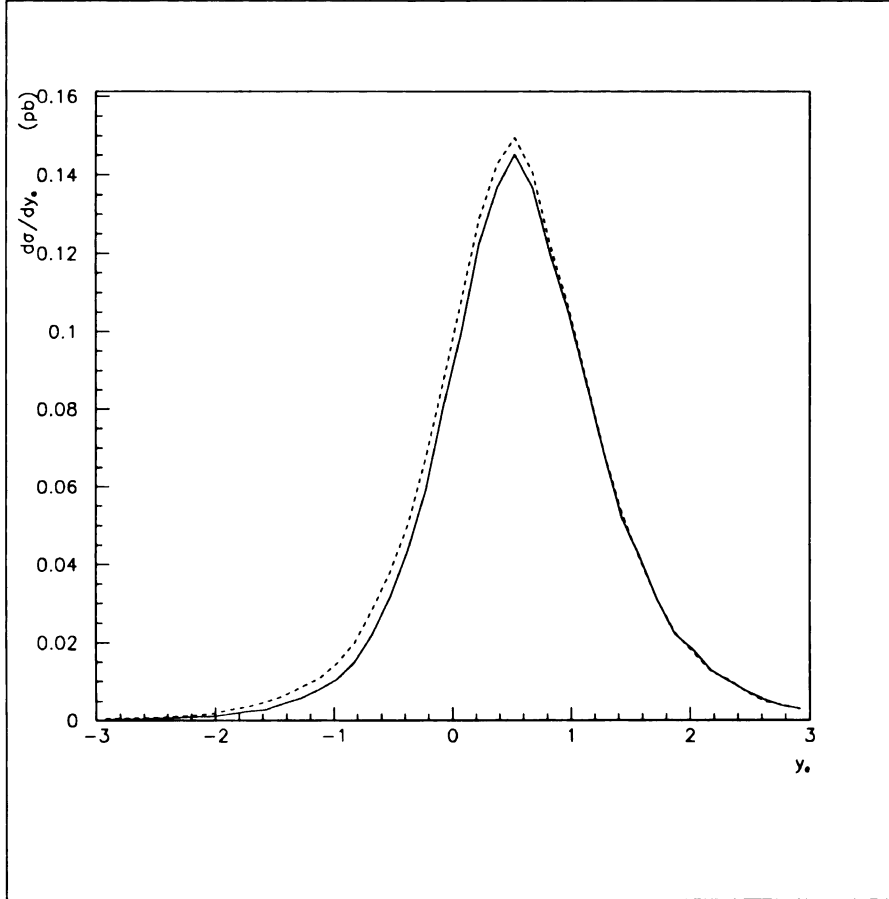


Figure 2.4:  $d\sigma/dy_e$  at LEP II, without cuts, for  $e^+e^- \rightarrow W^+W^- \rightarrow e^-\bar{\nu}_e u_{red}\bar{d}_{red}$ . Solid line is SM, dashed is  $\Delta\kappa_\gamma = -0.5$ .

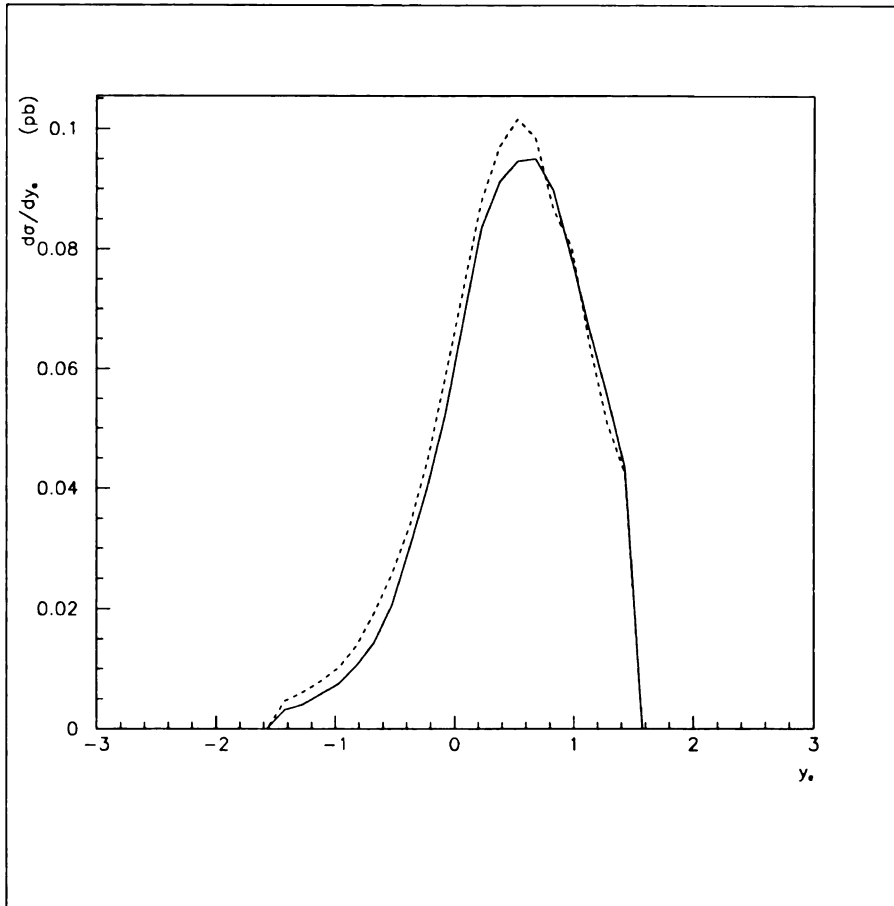


Figure 2.5:  $d\sigma/dy_e$  at LEP II, with cuts, for  $e^+e^- \rightarrow W^+W^- \rightarrow e^-\bar{\nu}_e u_{red}\bar{d}_{red}$ . Solid line is SM, dashed is  $\Delta\kappa_\gamma = -0.5$ .

### 2.1.2 Estimation of Sensitivity to Anomalous Couplings

Here follows an explanation of how we estimated the sensitivity of  $W$  pair production to anomalous triple-boson couplings. We assume the anomalous couplings are in fact zero; the limits we place on their allowed values from hypothetical experiments at LEP II and NLC indicate the sensitivity of these experiments to the anomalous couplings.

For simplicity, we focus on the  $\Delta\kappa_\gamma$  coupling, assuming that  $\lambda_\gamma = \Delta\kappa_Z = \lambda_Z = 0$ . To estimate the experimental limit that could be placed on an anomalous  $WW\gamma$  coupling, we must estimate the uncertainty in an experimental measurement of the cross section  $\sigma$ . For this analysis we simply assume that the standard deviation in the number of events  $N$  is  $\delta N = \sqrt{N}$ , *i.e.* that  $N$  obeys Poisson statistics. (For our purposes we do not include the efficiency of the detector.) The measured cross section would be  $\sigma = N/L$  where  $L$  is the integrated luminosity. The 3-sigma upper limit on  $\sigma$  (*i.e.* 99.7% confidence level) expected from Poisson statistics would be  $(N + 3\sqrt{N})/L$ . Thus the measurement would rule out a cross-section larger than  $\sigma + \delta\sigma_3$ , where

$$\delta\sigma_3 = 3\sqrt{\frac{\sigma}{L}}. \quad (2.1)$$

Similarly, for a 1-sigma (68.3% C.L.) or 2-sigma (95.5% C.L.) limit, we replace the 3 in this equation with a 1 or a 2, respectively.

To estimate the limit that could be placed on  $\Delta\kappa_\gamma$  or  $\lambda_\gamma$ , assuming the anomalous couplings are in fact zero, we compare the uncertainty  $\delta\sigma_3$  to the variation of the calculated  $\sigma$  as a function of the anomalous coupling. At the 3-sigma confidence level  $\Delta\kappa_\gamma$  would be in the range with

$$|\sigma(\Delta\kappa_\gamma) - \sigma(\Delta\kappa_\gamma = 0)| < \delta\sigma_3. \quad (2.2)$$

We obtain the results in Tables 2.2 and 2.3, for the experimental limits that

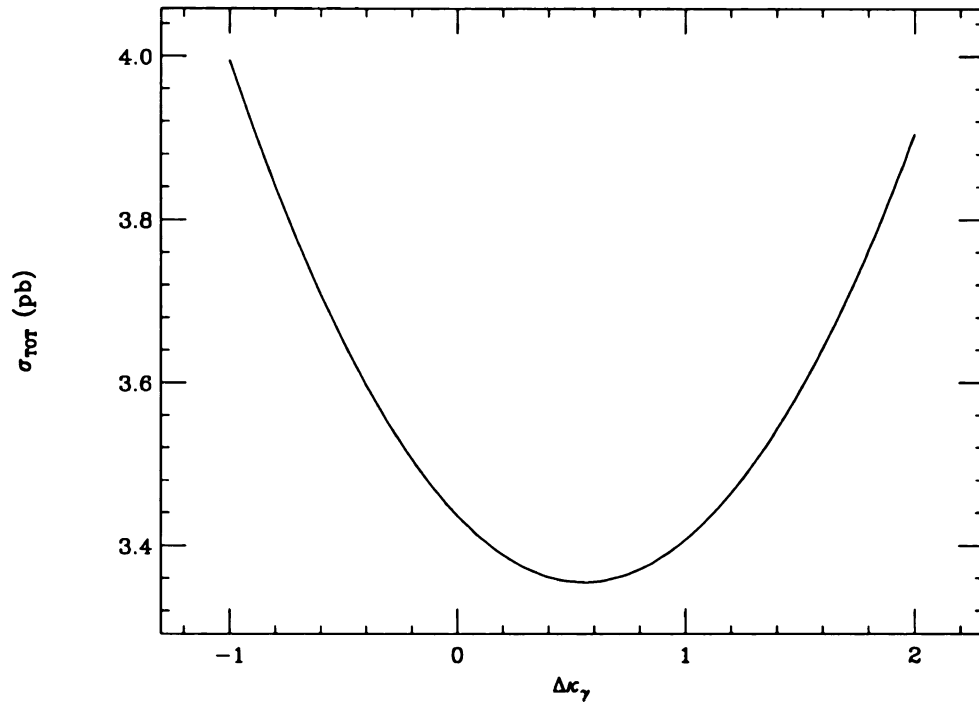


Figure 2.6: Total cross section at LEP II for  $e^+e^- \rightarrow W^+W^- \rightarrow l^-\bar{\nu}qq'$  vs.  $\Delta\kappa_\gamma$ .

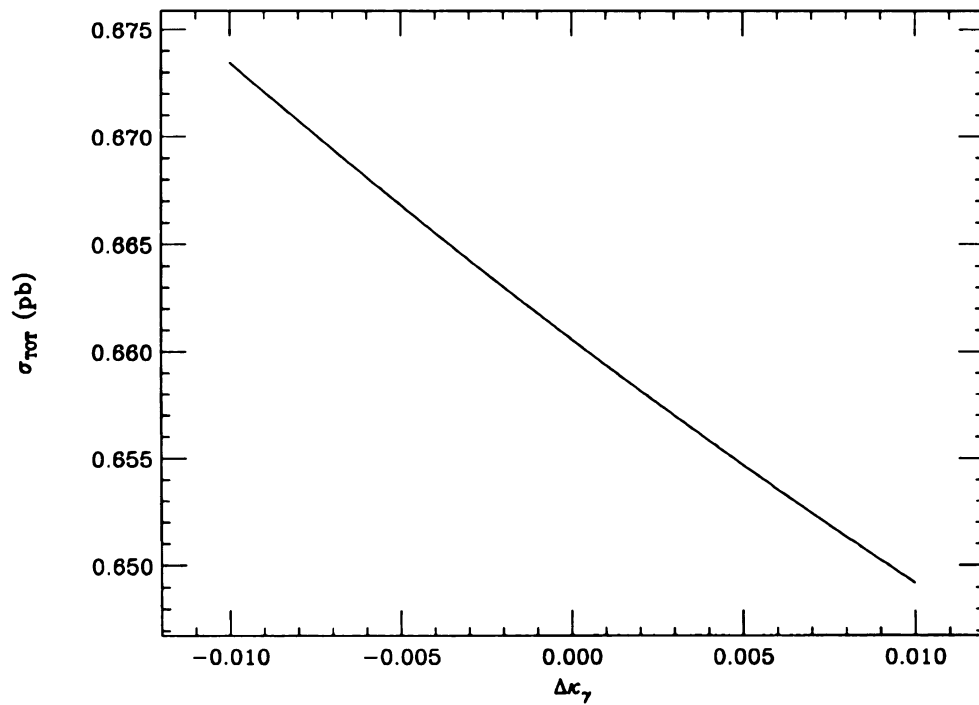


Figure 2.7: Total cross section at NLC for  $e^+e^- \rightarrow W^+W^- \rightarrow l^-\bar{\nu}qq'$  vs.  $\Delta\kappa_\gamma$ .

Table 2.2: LEP II limits on  $\Delta\kappa_\gamma$  from the total cross section.

LEP II Total Cross Section Limits			
	1 Sigma	2 Sigma	3 Sigma
$\Delta\kappa_\gamma$	+1.35	+1.52	+1.68
	-0.23	-0.41	-0.56

Table 2.3: NLC limits on  $\Delta\kappa_\gamma$  from the total cross section.

NLC Total Cross Section Limits			
	1 Sigma	2 Sigma	3 Sigma
$\Delta\kappa_\gamma$	+0.0031	+0.0062	+0.0095
	-0.0029	-0.0058	-0.0085

could be set on the anomalous couplings of the photon. We emphasize that the numbers in Tables 2.2 and 2.3 do not include possible experimental uncertainties.

This procedure gives us limits on anomalous couplings, *assuming the anomalous couplings are in fact zero*. In an experiment we would want to find the most probable value of the couplings based on our measurement. A glance at Figures 2.6 and 2.7 shows that for any measured value of the total cross section there correspond *two* values of anomalous coupling. This ambiguity possibly can be avoided with the polarization capability of the NLC.

Figure 2.8 shows the total cross section as a function of  $\Delta\kappa_\gamma$  for each polarization, for the process  $e^+e^- \rightarrow W^+W^-$  at the NLC. We calculated these cross sections from analytic amplitudes given in [18]. To see how these plots may resolve an ambiguity in  $\Delta\kappa_\gamma$ , imagine we perform the experiment with a left-handed electron beam and find a cross section of 15 pb. This corresponds to  $\Delta\kappa_\gamma$  of about -0.1 or 0.26. If we then measure the right-handed cross section, a value of 1 pb means  $\Delta\kappa_\gamma = -0.1$ ; while 2 pb means  $\Delta\kappa_\gamma = 0.26$ . In other words, after finding two possible values of  $\Delta\kappa_\gamma$  from the left-handed run, the right-handed run will distinguish between them

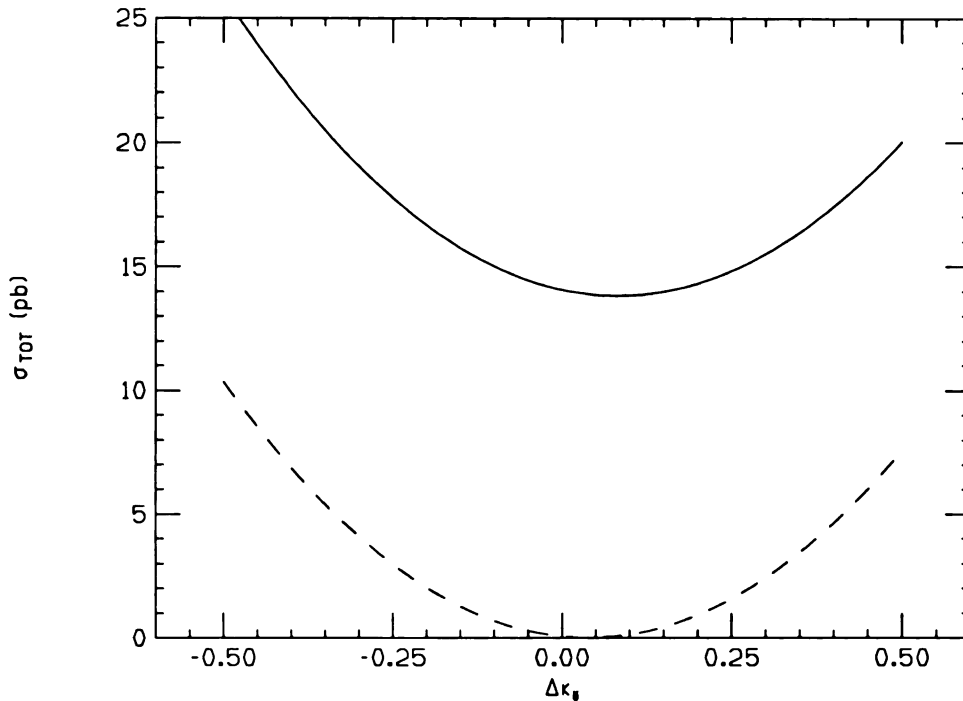


Figure 2.8: Total cross section at NLC for  $e^+e^- \rightarrow W^+W^-$  vs.  $\Delta\kappa_\gamma$ . The solid and dashed curves are for left and right polarized electron beams, respectively.

if the right-handed cross section is significantly different at the two values of  $\Delta\kappa_\gamma$ .

Figure 2.8 also shows why we chose to study the left polarized process at NLC. The right-handed cross section is much smaller, without showing any greater dependence on the anomalous couplings. The right-handed cross section is smaller because the t-channel diagram in Figure 2.1 is dominant, and vanishes in the right-polarized case due to the pure left-handed coupling of the  $W$  boson.

### 2.1.3 Using $\chi^2$ to Estimate Sensitivities to Anomalous Couplings

We also found limits on anomalous couplings by a  $\chi^2$  analysis. The  $\chi^2$  statistic provides a measure of the deviation of a *differential* cross section from the SM distribution. The strategy is similar to the above. Instead of limiting the deviation of the total cross section from the SM, we limit the  $\chi^2$ .

The reduced chi squared is defined by [22]

$$\tilde{\chi}_{exp}^2 = \frac{1}{d} \sum_{k=1}^d \frac{(O_k - E_k)^2}{E_k}, \quad (2.3)$$

where  $d$  is the number of degrees of freedom. For our purposes,  $d$  will be the number of bins into which we histogram a differential cross section.  $O_k$  is the number of events observed, and  $E_k$  is the number of events expected, in the  $k^{th}$  bin. The subscript *exp* is a reminder that this quantity is defined in terms of an experiment. In our theoretical study we are not making an actual observation, but merely simulating a possible experiment.  $N = L\sigma$  relates the number of observed events to the luminosity and the theoretical cross section. Using this formula to relate the numbers of events in Eq. (2.3) to cross sections, we define a theoretical reduced “chi squared” in terms of a binned differential cross section:

$$\tilde{\chi}_{th}^2(\Delta\kappa_\gamma) = \frac{L}{d} \sum_{k=1}^d \frac{(\sigma_{\Delta\kappa_\gamma,k} - \sigma_{SM,k})^2}{\sigma_{SM,k}}, \quad (2.4)$$

which is a function of the anomalous coupling.  $\sigma_k$  is the integrated cross section in the  $k^{th}$  bin. The quotes around “chi squared” indicate that it is a theoretical quantity, not distributed according to the chi-squared distribution—a distribution which refers to the results of experiments. We will nevertheless treat the theoretical chi squared as a deviation from the SM that could be measured if the anomalous couplings were not zero. Then, assuming the anomalous couplings *are* zero, we rule out those anomalous couplings that correspond to “unlikely” chi squareds (at some confidence level).

We will choose a distribution, calculate the chi squared as a function of anomalous coupling, and rule out large chi squareds. The authors of [18] found that the angular distribution of the final electron is most sensitive to the couplings we are interested in, so we will use the cosine distribution,  $d\sigma/d\cos\theta_e$ , as they did. Figure 2.9 shows this differential cross section at each collider for two values of  $\Delta\kappa_\gamma$ .

For calculational convenience and to remove any bias in  $\tilde{\chi}_{th}^2(\Delta\kappa_\gamma)$  due to Monte Carlo fluctuations, we fitted our Monte Carlo data to a smooth function. The functional form we choose is cubic times Gaussian in the electron cosine and quadratic in anomalous coupling. We rebin the smoothed distribution to use Eq. (2.4).

In principle we can bin our differential cross section into an arbitrary number of bins. The sensitivity to anomalous couplings of a distribution is dependent on how we bin that distribution. One restriction on our binning is that the bin widths must be large enough so that the number of events corresponding to the cross section in a particular bin is statistically significant. This means the number of bins cannot be too large. This turns out not to be a limiting factor for the process we are considering. We calculated sensitivities for various numbers of bins, and found that dividing  $d\sigma/d\cos\theta_e$  into 2 or 3 bins is most advantageous. This is initially surprising, as one might imagine that dividing the distribution into more bins increases our sensitivity to detailed features of the distribution. However, if there are no “features” to be distinguished in the anomalous distribution, increasing the number of bins is actually a disadvantage. This conclusion can be made plausible by considering the chi-squared for an experiment whose observed and predicted distributions differ only by a constant. In this case the highest value of  $\tilde{\chi}_{exp}^2$  will be obtained for only one bin, which is equivalent to calculating the squared deviation of the total cross section.

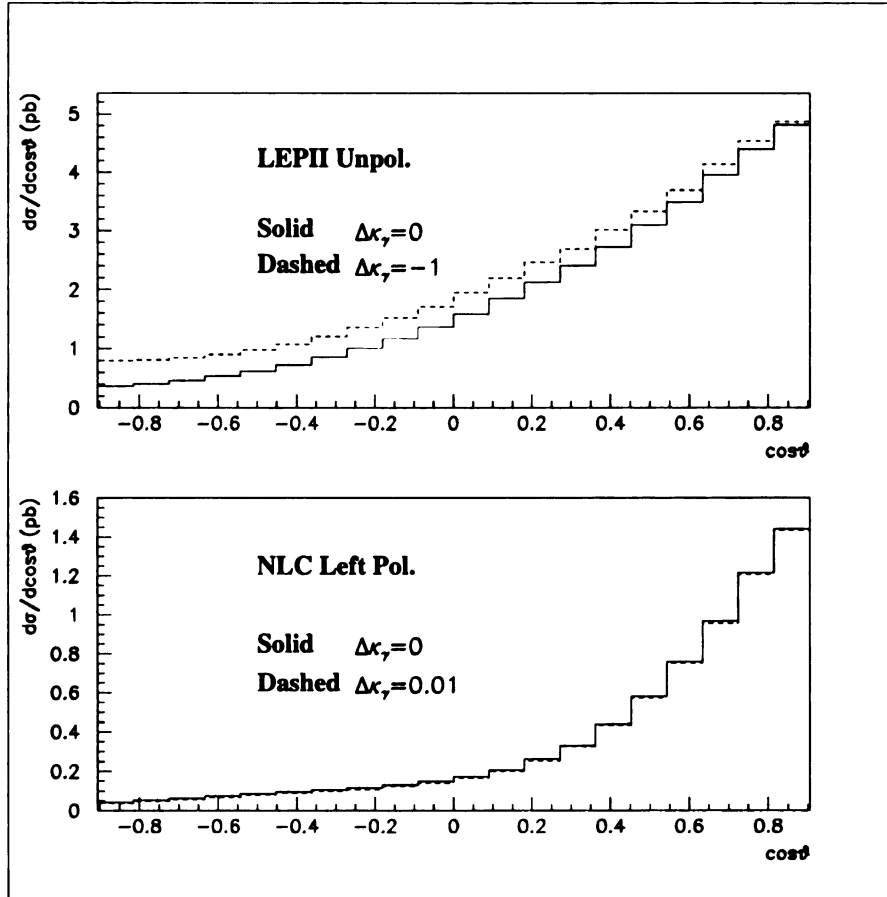


Figure 2.9: Differential cross sections in cosine of the lepton angle at LEP II and NLC for two values of  $\Delta\kappa_\gamma$ .

Table 2.4: LEP II limits on  $\Delta\kappa_\gamma$  from  $\tilde{\chi}^2$  of  $\cos\theta_e$  distribution.

LEP II $\tilde{\chi}^2$ Limits on $\Delta\kappa_\gamma$			
d	1 Sigma	2 Sigma	3 Sigma
1	+1.35	+1.52	+1.68
	-0.23	-0.41	-0.56
2	+0.35	+1.57	+1.73
	-0.23	-0.36	-0.46
3	+0.42	+1.60	+1.75
	-0.26	-0.37	-0.46

The highest value of the reduced chi-squared, however, does not necessarily correspond to the greatest sensitivity to anomalous coupling. We rule out a particular value of  $\Delta\kappa_\gamma$  if  $\tilde{\chi}_{th}^2(\Delta\kappa_\gamma)$  is greater than some cut-off  $\tilde{\chi}^2(d, CL)$ , which is given by the chi-squared distribution and depends on the number of bins  $d$  and the desired confidence level. The question of the optimal number of bins to use is therefore answered by the detailed calculation.

Plots of  $\tilde{\chi}_{th}^2$  versus anomalous coupling are shown in Figures 2.10 and 2.11, for 2 bins. We report estimated limits on  $\Delta\kappa_\gamma$  from LEP II and the NLC in Tables 2.4 and 2.5; for 1, 2, and 3 bins. We note that higher numbers of bins than 3 give poorer limits on  $\Delta\kappa_\gamma$ . Also note that the limit calculation for a chi-squared with one bin is equivalent to the calculation from deviations in the total cross section discussed above.

### 2.1.4 Conclusions

We estimated sensitivities to  $\Delta\kappa_\gamma$  at LEP II and the proposed NLC.  $W$  pair production is sensitive, at the 3 sigma level, to anomalous couplings of order 1 at LEP II, and less than order 0.01 at the NLC. We conclude that the NLC would be able to probe the loop-level corrections to the triple-boson couplings.

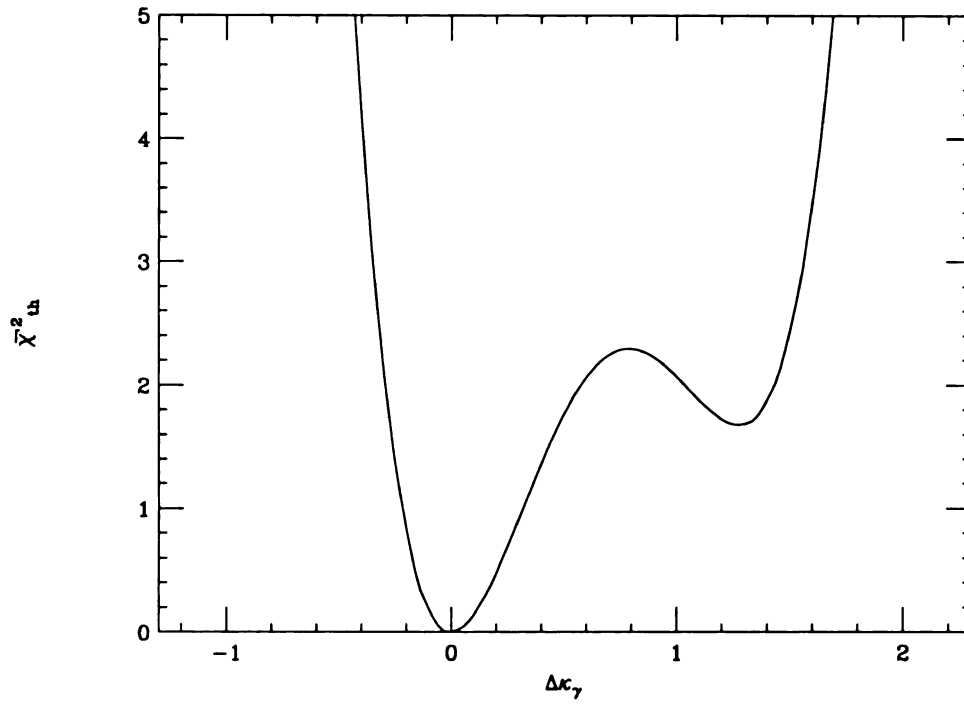


Figure 2.10:  $\tilde{\chi}_{th}^2$  at LEP II for  $e^+e^- \rightarrow W^+W^- \rightarrow l^-\bar{\nu}qq'$  vs.  $\Delta\kappa_\gamma$ .

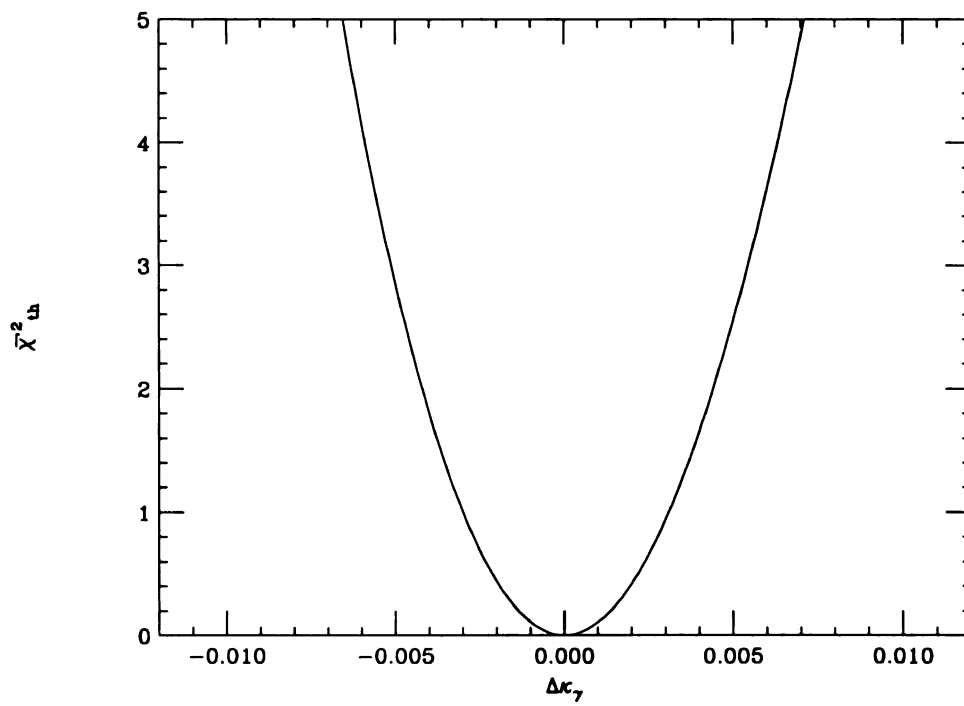


Figure 2.11:  $\tilde{\chi}_{th}^2$  at NLC for  $e^+e^- \rightarrow W^+W^- \rightarrow l^-\bar{\nu}qq'$  vs.  $\Delta\kappa_\gamma$ .

Table 2.5: NLC limits on  $\Delta\kappa_\gamma$  from  $\tilde{\chi}^2$  of  $\cos\theta_e$  distribution.

NLC $\tilde{\chi}^2$ Limits on $\Delta\kappa_\gamma$			
d	1 Sigma	2 Sigma	3 Sigma
1	+0.0031	+0.0062	+0.0095
	-0.0029	-0.0058	-0.0085
2	+0.0038	+0.0055	+0.0077
	-0.0036	-0.0052	-0.0071
3	+0.0041	+0.0062	+0.0083
	-0.0039	-0.0058	-0.0076

The LEP II sensitivities we find are worse than the sensitivities estimated in [18] to the anomalous Z couplings. This disparity is not surprising, since our choice of one  $W$  decay channel reduces the total number of events. Those authors expected about 4000 events at LEP II, whereas after cuts we find about 1600 events. Assuming similar sensitivity to photon and Z couplings, the reduction in statistics corresponds to a reduction in estimated sensitivity. In fact, a  $W$  pair production experiment cannot distinguish an anomalous Z coupling from an anomalous photon coupling from the total cross section alone. In the event of a non-standard experimental result, one may resolve this ambiguity with complementary data from an unambiguous process, such as  $W$  plus photon production, which only depends on the photon couplings. (In the next chapter we will estimate sensitivities to  $W$  plus photon production at a  $p\bar{p}$  collider.)

We find that using a  $\chi^2$  analysis generally improves our sensitivity only marginally, by about 15% or less. It turns out that the optimal number of bins for a chi-squared analysis to limit  $\Delta\kappa_\gamma$  is only two, because for the very small non-standard couplings we are simulating, there is little difference in shape between the Standard and non-standard differential cross sections.

In the next chapter we estimate sensitivities to anomalous couplings at the

Tevatron, and at a proposed Tevatron with a polarized proton beam. The fact that the protons and anti-protons are not elementary particles will add a level of complication to the calculation.

# Chapter 3

## Probing Anomalous Triple-Boson Couplings with Polarized Proton—Antiproton Collisions

### 3.1 Introduction

In the last few years the SPIN collaboration has shown in various technical notes that it is feasible to polarize the proton beam, longitudinally or transversely, during the colliding mode of the Tevatron [23]. Taking proton polarization as a possibility, we examine one of the possible physics topics that could be pursued with such a beam configuration – to study tri-boson couplings of the weak gauge bosons. (Other interesting physics topics involving polarization at the Tevatron collider can be found in Ref. [24].) †

In this chapter we consider two processes in proton-antiproton collisions

$$p + \bar{p} \rightarrow W^+ (\rightarrow \ell^+ \nu_\ell) + \gamma ,$$

$$p + \bar{p} \rightarrow W^\pm (\rightarrow \ell^\pm \bar{\nu}_\ell) + W^\mp (\rightarrow 2 \text{ jets}) .$$

---

†After this work was completed, we learned that a polarized colliding beam is less likely to be built in the near future at the Tevatron. However, since a polarized collider is technically feasible, we believe it is still interesting, and potentially useful, to explore theoretically the possible experiments with such a machine.

For  $\ell$  we include both  $e$  and  $\mu$ . The unpolarized cross-section for  $p\bar{p} \rightarrow W^- \gamma$  is equal to that for  $p\bar{p} \rightarrow W^+ \gamma$  in a CP invariant theory such as  $\mathcal{L}_3$ , the tri-boson Lagrangian defined in Section 1.2. However, we are interested in scattering of polarized protons, for which  $W^+ \gamma$  is more interesting than  $W^- \gamma$ , as we will see below.

The purpose of this chapter is to explore the experimental search for anomalous couplings in proton-antiproton collisions, *assuming the protons are longitudinally polarized*. The antiprotons are assumed to be unpolarized. With the Tevatron collider in mind [23, 24], we consider the center-of-mass energy equal to 2 TeV.

The reaction cross-section for a process involving the  $WW\gamma$  or  $WWZ$  coupling depends on the longitudinal polarization of the proton through spin-dependent parton distribution functions. The coupling of  $W^\pm$  to quarks ( $ud$  or other flavor combinations) is a V–A (vector–axial vector coupling) interaction, so the parton-level cross-section depends strongly on the helicities of the quarks: for massless quarks a  $W^\pm$  couples only to left-handed ( $L$ ) quarks and right-handed ( $R$ ) antiquarks. Thus the parton-level process depends strongly on helicity. The question is whether the *proton process* depends strongly on proton helicity. If a polarized proton contained equal parton densities of left-handed and right-handed quarks, then the proton cross-section would not depend on the proton helicity. However, we know that the densities of  $L$  and  $R$  quarks are not equal for polarized protons. Therefore, the  $p\bar{p}$  cross-section will be different for left-polarized and right-polarized protons.

Our calculations of the polarized-proton cross-sections depend on polarized parton distribution functions (hereafter abbreviated ppdf's), and these are only known with limited accuracy. The ppdf's are defined as follows: For any parton type  $f$ , we define

$$\begin{aligned} f_+(x) &= \frac{1}{2}(f(x) + \Delta f(x)) \\ &= \text{density of L (or R) partons in a L (or R) proton,} \end{aligned}$$

$$\begin{aligned}
f_-(\boldsymbol{x}) &= \frac{1}{2}(f(\boldsymbol{x}) - \Delta f(\boldsymbol{x})) \\
&= \text{density of L (or R) partons in a R (or L) proton,}
\end{aligned}$$

where  $\boldsymbol{x}$  is the fraction of the proton momentum carried by the parton. There are nine different parton types

$$f = u_{val} , d_{val} , u_{sea} = \bar{u}_{sea} , d_{sea} = \bar{d}_{sea} , g , s = \bar{s} , c = \bar{c} , b = \bar{b} , t = \bar{t} .$$

In the ppdf's we used, the  $u$  and  $d$  sea distributions are equal, but different than the  $s$  and  $c$  distributions, and the  $b$  and  $t$  distributions are zero

$$u_{sea}(\boldsymbol{x}) = d_{sea}(\boldsymbol{x}) ; b(\boldsymbol{x}) = 0 ; t(\boldsymbol{x}) = 0 .$$

Figure 3.1 shows the polarization dependence of the ppdf's we used, by plotting  $\boldsymbol{x} \Delta f(\boldsymbol{x})$  for several parton species. The ppdf's depend on momentum scale  $Q$ ; *i.e.*  $f_{\pm} = f_{\pm}(\boldsymbol{x}, Q^2)$ . Fig. 3.1 corresponds to  $Q=80$  GeV. (These ppdf's are calculated from a program based on Morfin-Tung parton distribution functions [25, 26].) The ppdf's have been measured, to some limited precision, from polarized deep-inelastic lepton scattering [27]. For example, recent data from the Spin Muon Collaboration (SMC) at CERN provide a measurement of the polarization difference, integrated over  $\boldsymbol{x}$  and weighted by  $e_q^2/e^2$  [28]:

$$\begin{aligned}
I &\equiv \int_0^1 d\boldsymbol{x} \sum_{f=u,d,s,c} \frac{e_f^2}{e^2} \frac{1}{2} [\Delta f(\boldsymbol{x}, Q^2) + \Delta \bar{f}(\boldsymbol{x}, Q^2)] \\
&= 0.142 \pm 0.008 \pm 0.011,
\end{aligned}$$

where the momentum scale is  $Q^2 = 10 \text{ GeV}^2$ . The ppdf's used in our calculations have

$$\begin{aligned}
I &= 0.138 \text{ for } Q^2 = 10 \text{ GeV}^2 , \\
I &= 0.163 \text{ for } Q^2 = (80 \text{ GeV})^2 ,
\end{aligned}$$

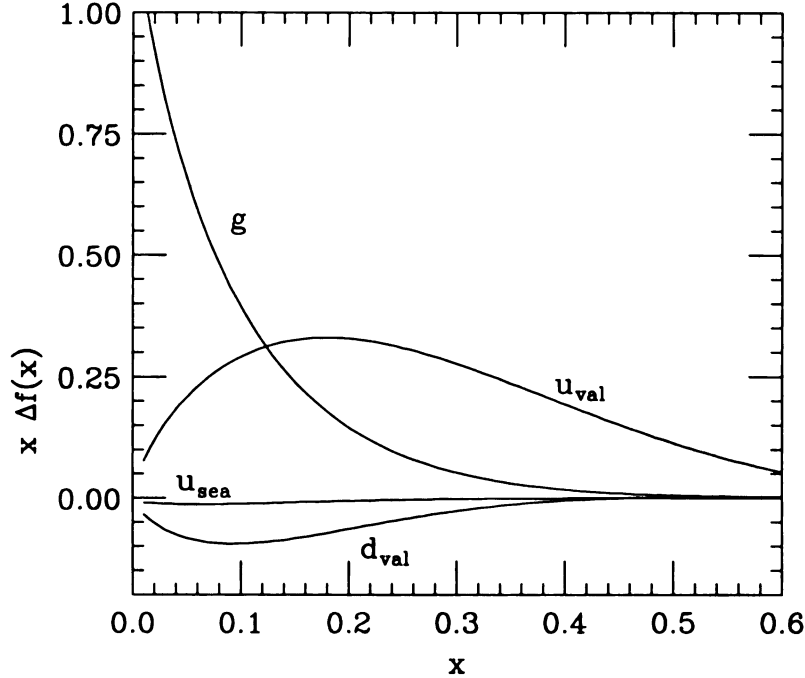


Figure 3.1: Polarized parton distribution functions. The curves are  $x\Delta f(x)$  vs  $x$  for parton types  $u_{val}$ ,  $d_{val}$ ,  $u_{sea}(=d_{sea})$ ,  $g$ , which are the most important partons in our calculations.

where the  $Q^2$ -dependence is determined by renormalization group equations. For  $W^\pm$  production the relevant momentum scale is of order  $M_W$ . The spin-dependence of the quark densities is rather small, as indicated by the small value of  $I$ ,<sup>†</sup> so one question that motivates our study is whether the cross-sections for these  $W^\pm$ -production processes depend significantly on the proton helicity.

In Section 3.2 we calculate the cross-section for the process  $p_\lambda \bar{p} \rightarrow W^+ \gamma$ , where  $\lambda = L$  or  $R$  denotes a left-handed or right-handed proton. This process is sensitive to the  $WW\gamma$  anomalous couplings. In Section 3.3 we consider the process  $p_\lambda \bar{p} \rightarrow W^\pm W^\mp$ , which is sensitive to both  $WW\gamma$  and  $WWZ$  anomalous couplings. The purpose of these calculations is to explore whether polarization of the protons can increase the sensitivity of measurement of anomalous couplings.

<sup>†</sup> $I = .138$  is small compared to the prediction  $I = .17$ , based on the Ellis-Jaffe sum rule, which assumes vanishing strange sea polarization [29].

## 3.2 $W^+\gamma$ production

The Feynman diagrams for the process  $p + \bar{p} \rightarrow W^+ + \gamma$  are shown in Figure 3.2. One diagram has a  $WW\gamma$  vertex, so the cross-section depends on the anomalous photon coupling parameters  $\Delta\kappa_\gamma$  and  $\lambda_\gamma$ . This process can be used to place limits on the anomalous couplings. Calculations of the unpolarized cross-section with anomalous couplings were described in References [30] and [31]. For polarized scattering we expect the cross-section for left-polarized protons to be larger than for right-polarized protons, because the produced  $W^+$  line is always connected to a left-handed quark line. We only consider the process  $p_\lambda \bar{p} \rightarrow W^+\gamma$ , and not  $W^-\gamma$ , because the former is more sensitive to the proton helicity. A  $W^+$  comes from a  $u$  quark, whereas a  $W^-$  comes from a  $d$  quark. The helicity dependence is stronger for  $u$  than  $d$  in a proton, as seen in Figure 3.1. To investigate whether polarizing the proton beam would yield better limits on  $\Delta\kappa_\gamma$  and  $\lambda_\gamma$ , we have calculated the polarized and unpolarized cross-sections. The results of this study are reported in this section.

### 3.2.1 Method of Calculation

The cross-section for  $p_\lambda + \bar{p} \rightarrow W^+ + \gamma$ , where  $\lambda$  is  $L$  or  $R$  for left-handed or right-handed protons, and with subsequent decay  $W^+ \rightarrow \ell^+ + \nu_\ell$ , is expressed as

$$\sigma(\lambda) = \frac{1}{2} \int_0^1 dx dx' [\hat{\sigma}_{LR}(xP_1, x'P_2)u_\pm(x)d(x') + \hat{\sigma}_{LR}(x'P_2, xP_1)\bar{d}_\mp(x)\bar{u}(x')] \quad (3.1)$$

where the notation is as follows: The parton cross-section  $\hat{\sigma}_{LR}(p_1, p_2)$  is for the process  $u_L(p_1) + \bar{d}_R(p_2) \rightarrow W^+ + \gamma$ . The upper sign on  $u_\pm(x)$  and  $\bar{d}_\mp(x)$  is for  $\lambda = L$  and the lower sign is for  $\lambda = R$ . The factor of  $\frac{1}{2}$  averages over the spins of the

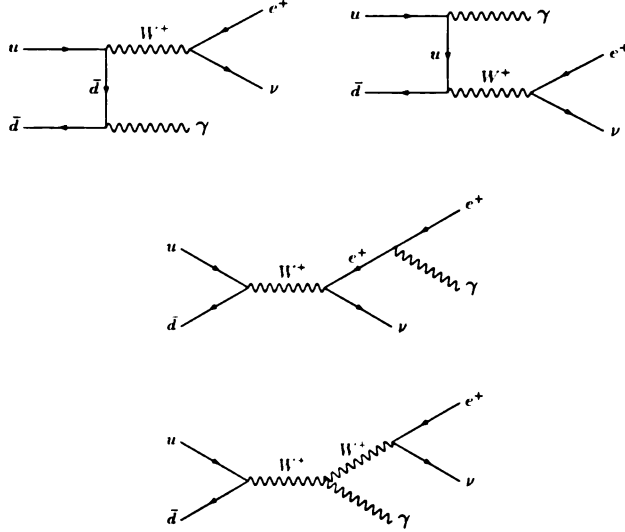


Figure 3.2: Feynman diagrams for the process  $u\bar{d} \rightarrow e^+\nu\gamma$ .

unpolarized  $\bar{p}$ . The first line in Eq. (3.1) corresponds to  $u, \bar{d}$  coming from  $p, \bar{p}$ , and the second line corresponds to  $\bar{d}, u$  coming from  $p, \bar{p}$ , respectively.  $x$  and  $x'$  are the parton momentum fractions in the proton and antiproton respectively. The parton distribution functions are, for example,

$$u_{\pm}(x) = u \text{ quark with same/opposite helicity as } p$$

$$d(x') = \bar{d} \text{ quark in unpolarized } \bar{p}$$

$$\bar{d}_{\mp}(x) = \bar{d} \text{ quark with opposite/same helicity as } p$$

$$\bar{u}(x') = u \text{ quark in unpolarized } \bar{p}.$$

We also add the contribution for the parton process  $c + \bar{s} \rightarrow W^+ + \gamma$ , which is, however, small. (We ignore Cabibbo-Kobayashi-Maskawa mixing in this work.) Finally, we add the cross-sections for two lepton decay modes of the  $W^+$ ; that is,  $\ell$  can be either  $e$  or  $\mu$ .

The parton cross-section is calculated from helicity amplitudes for the reaction. In this reaction there is only one nonzero helicity amplitude, with  $\lambda_u = L$  and  $\lambda_d = R$ , because we approximate the quark masses as 0. We calculate the helicity amplitude  $\mathcal{M}_{LR}$  analytically. Then the parton cross-section is

$$\hat{\sigma}_{LR} = \int d\Phi |\mathcal{M}_{LR}|^2 \quad (3.2)$$

where  $\int d\Phi$  indicates a phase space integral.

The phase space and  $x, x'$  integrations are performed by a Monte-Carlo program, based on the Vegas Monte-Carlo integration routine [21]. The style of the full Monte-Carlo program is the same as the program PAPAGENO [32].

The kinematic cuts we impose on the final  $\ell^+$  and  $\gamma$  are:

$$\text{rapidity } |\eta_\ell| < 3, \quad |\eta_\gamma| < 3, \quad (3.3)$$

$$\text{transverse momentum } p_{T\ell} > 20 \text{ GeV}, \quad p_{T\gamma} > 20 \text{ GeV}, \quad (3.4)$$

$$\Delta R \equiv \sqrt{(\Delta\eta)^2 + (\Delta\phi)^2} > 0.7, \quad (3.5)$$

where  $\Delta R$  is the separation of the  $\ell^+$  and  $\gamma$  in  $\eta - \phi$  space. The only cut on the neutrino is a transverse momentum cut  $p_{T\nu} > 20 \text{ GeV}$ ; that is, we require

$$\cancel{E}_T > 20 \text{ GeV}. \quad (3.6)$$

At the parton level, there is no background to this process from other interactions, as long as we require the  $W^+$  to decay to leptons. There is an experimental background due to confusion between jets and photons in the detector [31]. However, we do not consider the experimental background here, because our interest is to examine the effect of proton polarization, compared with the unpolarized case.

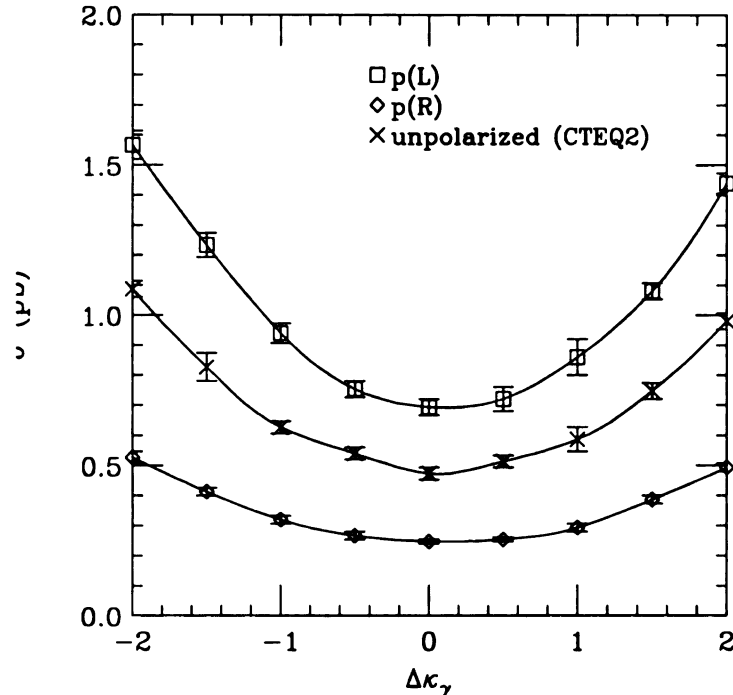


Figure 3.3: Total cross-section (with cuts in Eqs.(3.3)–(3.5)) for polarized protons *vs* anomalous coupling  $\Delta\kappa_\gamma$ , assuming  $\lambda_\gamma = 0$ . The unpolarized cross-section was calculated separately using CTEQ2 parton distribution functions.

### 3.2.2 Results

Tables 3.1 and 3.2 show the results of our calculations: the  $W^+\gamma$  production cross-section for polarized and unpolarized protons with different values of anomalous couplings  $\Delta\kappa_\gamma$  and  $\lambda_\gamma$ . The cross-section includes the branching ratio  $2/9$  for  $W^+ \rightarrow \ell^+ \nu_\ell$ , where the decay modes  $\ell = e$  and  $\ell = \mu$  are added. (The branching ratio factor  $2/9$  is included in all cross-sections reported hereafter.) The cross-section is smallest for the Standard Model values  $\Delta\kappa_\gamma = 0$  and  $\lambda_\gamma = 0$ . The cross-section depends more strongly on  $\lambda_\gamma$  than on  $\Delta\kappa_\gamma$ . Figures 3.3 and 3.4 show plots of the cross-section *vs*  $\Delta\kappa_\gamma$  assuming  $\lambda_\gamma = 0$ , and *vs*  $\lambda_\gamma$  assuming  $\Delta\kappa_\gamma = 0$ . As expected, the cross-section is larger for left-handed protons;  $\sigma(L)$  is roughly 3 times  $\sigma(R)$ , and so roughly 1.5 times the unpolarized cross-section. The unpolarized cross-section is by definition equal to  $\frac{1}{2}(\sigma(L) + \sigma(R))$ .

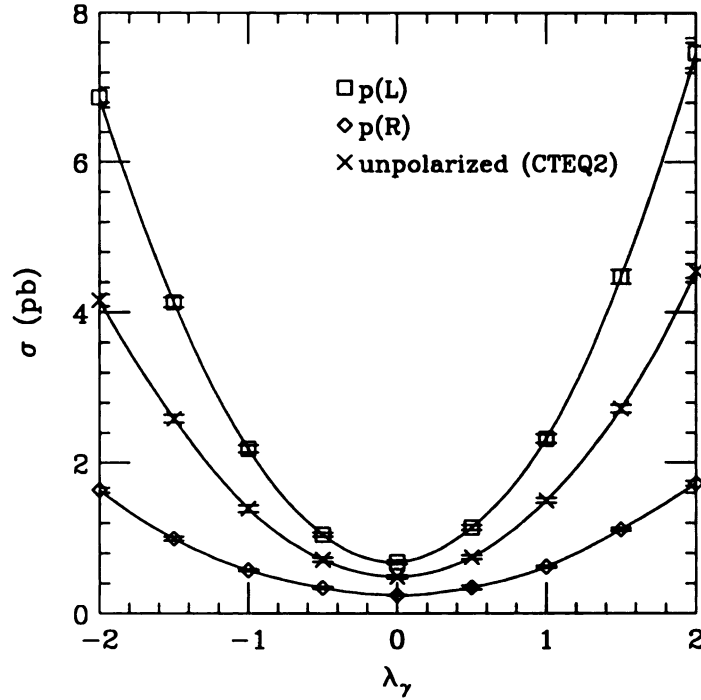


Figure 3.4: Total cross-section (with cuts in Eqs.(3.3)–(3.5)) for polarized protons *vs* anomalous coupling  $\lambda_\gamma$ , assuming  $\Delta\kappa_\gamma = 0$ . The unpolarized cross-section was calculated separately using CTEQ2 parton distribution functions.

Figures 3.3 and 3.4 show only the total cross-section, for the cuts specified in Eqs. (3.3)–(3.5). Analysis of differential cross-sections with respect to relevant kinematic variables—such as the  $\chi^2$  analysis of the previous chapter—may provide more precise tests of anomalous couplings [31]. For example, Figure 3.5 shows the distribution of  $p_{T\gamma}$  for polarized proton scattering, with  $\Delta\kappa_\gamma = 0$  (solid line) and  $\Delta\kappa_\gamma = -1$  (dashed line). The shapes of the distributions are similar for left- or right-handed protons, but there is an overall difference of magnitude.

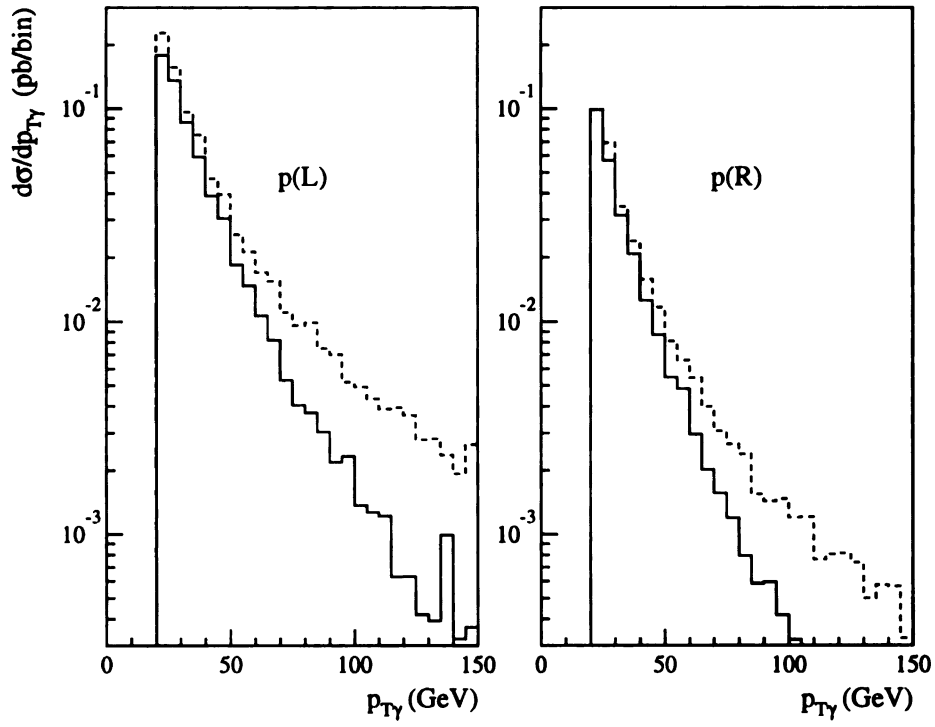


Figure 3.5: Distribution of photon transverse momentum  $p_{T\gamma}$ . The solid line is for  $\Delta\kappa_\gamma = 0$ , and the dashed line is for  $\Delta\kappa_\gamma = -1$ ; in both cases  $\lambda_\gamma = 0$ .

### 3.2.3 Limits on $\Delta\kappa_\gamma$ and $\lambda_\gamma$

Tables 3.1 and 3.2 are results from the Monte Carlo calculations of cross-section *vs* anomalous couplings. There is a fairly large effect of proton polarization:  $\sigma(L)$  is generally about a factor of 3 larger than  $\sigma(R)$ . But to see whether an experiment with polarized protons would yield a significantly better measurement of the anomalous couplings, we must estimate the experimental limit that could be set on  $\Delta\kappa_\gamma$  or  $\lambda_\gamma$ , for a given integrated luminosity. The sensitivities to these anomalous couplings are estimated using the same procedure as in Chapter 2. That is, we assume the number of events  $N$  detected is predicted by the SM, and an uncertainty in this number given by  $\sqrt{N}$ . (This is an underestimate of the experimental uncertainty; for instance, it does not take into account the experimental background of jets misidentified as photons.) The anomalous couplings which correspond to a three-sigma fluctuation of the number of events are the largest anomalous couplings consistent with a SM result, at the 99.7% confidence level; in other words these values of the anomalous couplings are the  $3\sigma$  limits on the couplings.

The left-polarized proton provides a better limit on  $\Delta\kappa_\gamma$  or  $\lambda_\gamma$ , because it has a larger cross-section. The improvement in precision from left-polarized protons, compared to unpolarized, is not very great, because  $\sigma(L)$  is only about 1.5 times larger than  $\sigma(\text{unpolarized})$ , and because the precision on  $\sigma$  is only proportional to  $\sigma^{1/2}$ . The result is that the total cross-section for left-polarized proton scattering can provide a better limit on  $\Delta\kappa_\gamma$  or  $\lambda_\gamma$  than that for unpolarized scattering, better by about 10 to 20 %.

Another way to consider the effect of proton helicity is to calculate the left-right asymmetry, defined by

$$\mathcal{A} = \frac{\sigma(L) - \sigma(R)}{\sigma(L) + \sigma(R)}. \quad (3.7)$$

An asymmetry measurement may be accurate experimentally because systematic

errors cancel in the ratio. The possible range of  $\mathcal{A}$  is  $-1 \leq \mathcal{A} \leq 1$ , and  $\mathcal{A}$  is equal to 0 in a left-right symmetric world. For the *parton* process  $q\lambda\bar{q}' \rightarrow W^+\gamma$ , we have  $\mathcal{A} = 1$  because only left-handed quarks contribute. For the *proton* process, the asymmetry is reported in Tables 3.1 and 3.2; we find  $\mathcal{A} \approx 0.5$ . However,  $\mathcal{A}$  depends only weakly on  $\Delta\kappa_\gamma$  and  $\lambda_\gamma$ :  $\mathcal{A}$  varies by  $\mathcal{O}(10\%)$  over the range of anomalous couplings considered. Thus a measurement of  $\mathcal{A}$  to determine  $\Delta\kappa_\gamma$  or  $\lambda_\gamma$  would require high statistics.

### 3.3 $W^+W^-$ production

The process  $p\bar{p} \rightarrow W^+W^-$  provides a way to test the Standard Model  $WWV$  vertices for both  $V = \gamma$  and  $V = Z^0$ , although we may not be able to distinguish the two couplings from each other unless we can compare to results from the  $W\gamma$  production process discussed above. We consider the electroweak process

$$p(\lambda) + \bar{p} \rightarrow W^+ (\rightarrow \bar{\ell} + \nu_\ell) + W^- (\rightarrow d + \bar{u}) , \quad (3.8)$$

and also the process in which the  $W^-$  decays leptonically while the  $W^+$  decays to 2 jets. The diagrams for the production of two  $W$ 's include two electroweak vertices, in contrast to the background diagrams (discussed below), which only contain one electroweak vertex. The complete set of Feynman diagrams with the final state  $\bar{\ell}\nu d\bar{u}$  includes diagrams that do not have the form of  $W^+W^-$  production. Figure 3.6 shows the complete set of Feynman diagrams for the parton process

$$u + \bar{u} \rightarrow W^+ + d + \bar{u} , \quad \text{with } W^+ \rightarrow \bar{\ell} + \nu_\ell ; \quad (3.9)$$

there is similarly a set of diagrams for the process

$$d + \bar{d} \rightarrow W^+ + d + \bar{u} , \quad \text{with } W^+ \rightarrow \bar{\ell} + \nu_\ell . \quad (3.10)$$

Also, there are similar diagrams for production of  $W^- + u + \bar{d}$ , with  $W^- \rightarrow \ell + \bar{\nu}_\ell$ . (The complete set of diagrams for the final state  $\bar{\ell}\nu d\bar{u}$ , or  $\ell\bar{\nu}u\bar{d}$ , includes additional

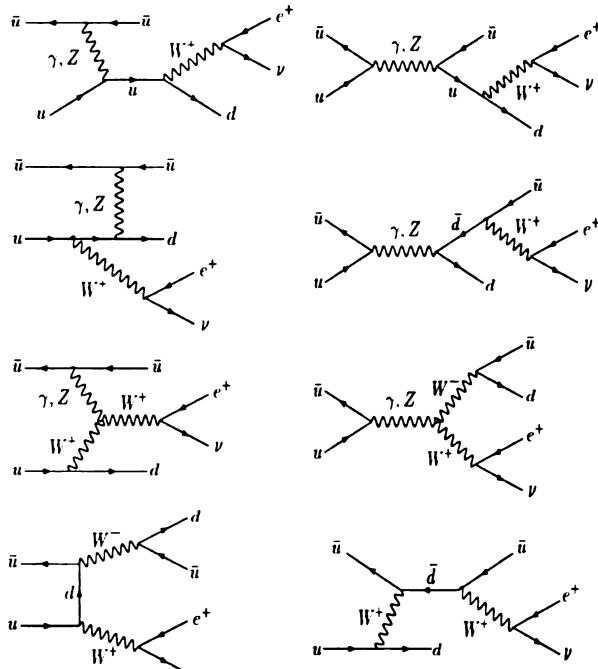


Figure 3.6: Complete set of electroweak diagrams for  $u + \bar{u} \rightarrow d + \bar{u} + W^+ (\rightarrow \bar{\ell} + \nu_{\ell})$ .

diagrams in which the leptons are not decay products of a single narrow  $W^{\pm}$ .) These parton processes involve the  $WW\gamma$  and  $WWZ$  vertices in some Feynman diagrams, so the cross-sections depend on anomalous  $WWV$  couplings, *i.e.* the parameters  $\Delta\kappa_{\gamma}, \Delta\kappa_Z, \lambda_{\gamma}, \lambda_Z$ . In this section we study the cross-section as a function of these non-Standard parameters, for polarized protons. The purpose is again to see whether an experiment with a polarized proton beam would yield a stronger test of the electroweak triple-boson vertices.

Some, though not all, of the Feynman diagrams in Fig. 3.6 have the form of  $W^+W^-$  production, followed by decays of the  $W$ 's, one leptonically and the other into two jets. At 2 TeV center-of-mass energy, the cross-section is dominated by the  $W^+W^-$  production. Therefore, as explained further below, we approximate the cross-section by  $W^+W^-$  production. The cross-sections for  $\bar{\ell}\nu u\bar{d}$  and  $\bar{\ell}\nu\bar{u}d$  final states are equal in this approximation, because either  $W$  is equally likely to decay leptonically.

A related process is  $W^\pm Z^0$  production, where the  $Z^0$  decays to 2 jets, *e.g.*,

$$u + \bar{d} \rightarrow W^+ (\rightarrow \ell^+ + \nu_\ell) + Z^0 (\rightarrow q + \bar{q}) . \quad (3.11)$$

In our calculations we ignore the  $W^\pm Z^0$  production. In a theoretical calculation the  $W^+W^-$  production is distinguishable from the  $W^\pm Z^0$  production. However, in an experiment these two processes are tangled together, because they are both observed as  $W^\pm + 2 \text{ jets}$ . In our  $W^+W^-$  calculation we impose a kinematic cut on the invariant mass  $M_{2j}$  of the 2 jets, making  $M_{2j}$  approximately equal to the  $W^\pm$  mass; specifically we take  $M_{2j}$  between 70 and 90 GeV. (This cut reduces the QCD background of  $W^\pm + 2 \text{ jets}$ , as discussed in the next subsection.) But even with this cut on  $M_{2j}$  there would still be an overlap between  $W^+W^-$  production and  $W^\pm Z^0$  production. The purpose of our calculation is a theoretical study of the effect of proton polarization on the cross-section. A complete analysis of experimental data would need to include both the  $W^+W^-$  and  $W^\pm Z^0$  processes together.

The method of calculation is similar to that of  $W\gamma$  production in Section 3.1, but with some differences. In Section 3.2 only one parton helicity combination contributes,  $u(L)\bar{d}(R)$ . Here two helicity combinations contribute, for example  $u(L)\bar{u}(R)$  and  $u(R)\bar{u}(L)$ , and we include both. In fact, for Standard couplings the contribution from  $u(R)\bar{u}(L)$  is very small compared to  $u(L)\bar{u}(R)$ , because of interference between Feynman diagrams, so the parton-level process still depends strongly on quark helicities. A more important difference is that in Section 3.2 there was no parton-level background process, whereas here we have a large background from electroweak+QCD processes.

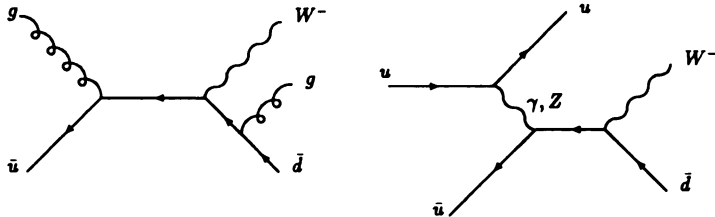


Figure 3.7: Example diagrams for QCD production of  $W^+$  and two jets.

### 3.3.1 Background, Approximations, and Cuts

The parton-level background to this process is the production of  $W^\pm + 2 \text{ jets}$  by processes with one electroweak vertex and one QCD vertex. Two example background diagrams are shown in Figure 3.7. All combinations of quarks and gluons in the initial and final states are included in the complete set. These processes do not interfere quantum mechanically with our doubly electroweak signal process, because they have a different color structure. For example, the  $q\bar{q}g$  vertex is color octet, where  $g$  denotes the gluon, whereas  $q\bar{q}\gamma$  or  $q\bar{q}Z^0$  vertices are color singlet. However, the final states are indistinguishable experimentally, so the doubly electroweak reaction is hidden in a background of electroweak-QCD reactions.

We have calculated the background cross-section from the helicity amplitudes for a complete set of  $W^\pm + 2 \text{ jets}$  processes [33], with the polarized parton distribution functions described in Section 3.1. The background reactions should depend strongly on the helicity of the proton: The produced  $W^\pm$  must connect to a left-handed quark

or right-handed antiquark for massless quarks, by the V–A coupling; the density of quarks of given helicity depends on the helicity of the proton. By contrast, for the signal reaction the diagrams *with  $WW\gamma$  or  $WWZ$  vertices* do not require any specific helicities of the incoming quarks. Thus the signal reaction will have a different dependence on proton helicity than the background. The important question is whether the signal-to-background ratio in the measurement of anomalous  $WWV$  couplings is better for left- or right-polarized protons.

To reduce the background we impose a cut on the invariant mass  $M_{2j}$  of the 2 jets, putting  $M_{2j}$  approximately equal to  $M_W$ . The solid curve in Figure 3.8 shows the distribution of the invariant mass of the two jets produced by the complete unpolarized doubly electroweak process with final state  $q\bar{q}'W^+$ , with  $W^+ \rightarrow \bar{\ell}\nu_\ell$ , for  $\sqrt{s} = 2$  TeV. (Figures 3.8 through 3.12 are 30 bin histograms; the vertical axes are labelled in picobarns *per bin*.) The  $q\bar{q}'$  invariant mass is peaked at the  $W^+$  mass. Because the cross-section is dominated by the  $W^+$  resonance, we approximate the calculation by keeping only the Feynman diagrams that produce a  $W^+W^-$  pair, which is an accurate simplifying approximation. Furthermore, we *require* the  $q\bar{q}'$  invariant mass to be approximately equal to the  $W^\pm$  mass: we calculate the cross-section only for events with  $M_{q\bar{q}'}$  between 70 and 90 GeV. The dotted curve in Figure 3.8 shows the 2-jet mass distribution when we neglect all but the  $W^+W^-$  pair production diagrams and also require the 2-jet mass to be between 70 and 90 GeV. With this  $M_{2j}$  cut, the complete doubly electroweak process is practically the same as production of  $W^+W^-$  followed by leptonic decay of  $W^\pm$  and quark-antiquark decay of  $W^\mp$ . For comparison, Fig. 3.9 shows the 2-jet mass distribution of the background processes with the kinematic cuts listed in Eqs. (3.12)–(3.14) below. The cut  $70 \text{ GeV} < M_{q\bar{q}'} < 90 \text{ GeV}$  reduces the total background significantly, because there is no resonant effect in the background processes.

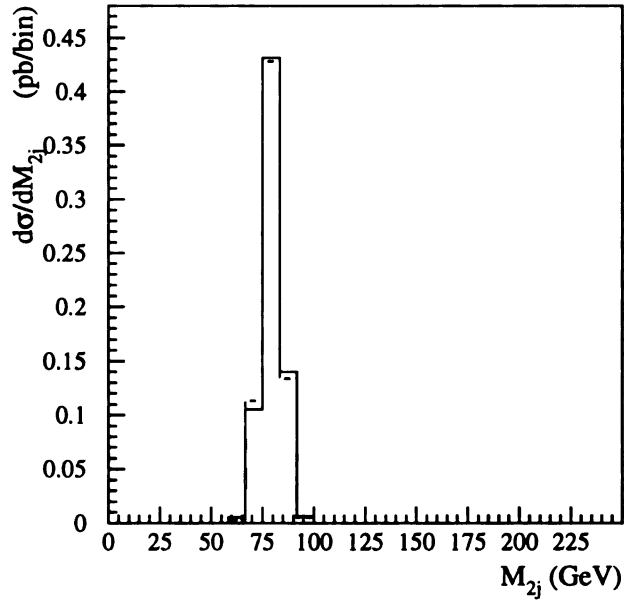
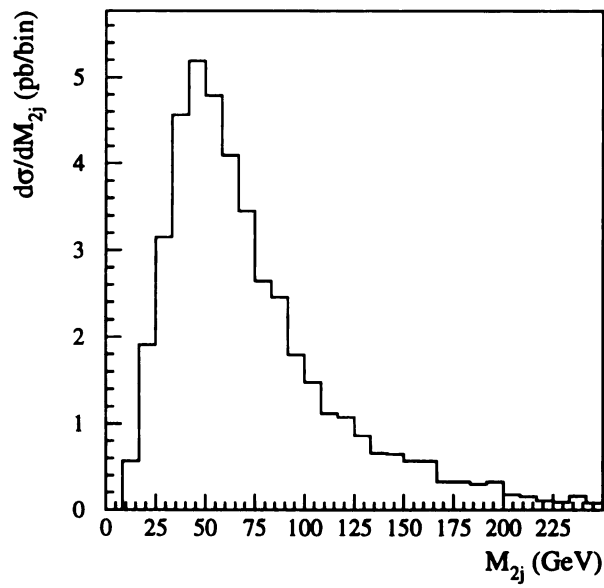


Figure 3.8: Two-jet invariant mass distribution for the signal process. The solid line is the result of the complete calculation of the pure electroweak process  $p + \bar{p} \rightarrow q\bar{q}'W^+$ , with  $W^+ \rightarrow \bar{\ell}\nu_\ell$ ; the dotted line is the result of the calculation of  $W^+W^-$  production, with  $W^+ \rightarrow \bar{\ell}\nu_\ell$  and  $W^- \rightarrow 2 \text{ jets}$ , with a cut on the two-jet invariant mass ( $70 < M_{2j} < 90$  GeV).



**Figure 3.9:** Two-jet invariant mass distribution for the QCD background processes  $p\bar{p} \rightarrow W^+ + 2 \text{ jets}$ . (The cross-section for  $W^- + 2 \text{ jets}$  is the same, for unpolarized scattering.)

In addition to the  $M_{2j}$ -cut just described, we impose the following kinematic cuts on all the final-state particles except the neutrino:

$$\text{rapidity } |\eta| < 3, \quad (3.12)$$

$$\text{transverse momentum } p_T > 15 \text{ GeV}, \quad (3.13)$$

$$\Delta R \equiv \sqrt{(\Delta\eta)^2 + (\Delta\phi)^2} > 0.7, \quad (3.14)$$

where  $\Delta R$  is the separation of any pair of final particles not including the neutrino. In the case of the neutrino, we impose only a transverse momentum cut,  $p_{T\nu} > 15$  GeV. That is,

$$\cancel{E}_T > 15 \text{ GeV}. \quad (3.15)$$

Figure 3.10 is another comparison between the complete doubly electroweak calculation, shown as the solid line, and the simplified approximation ( $W^+W^-$  production with subsequent  $W^\pm$  decays), shown as the dashed line. Figure 3.10 compares the  $\sqrt{\hat{s}}$  distributions, where  $\sqrt{\hat{s}}$  is the center of mass energy of the parton-level process. Again, the two calculations are practically equal.

We also consider, separately, a cut requiring large  $\sqrt{\hat{s}}$ , specifically  $\sqrt{\hat{s}} > 340$  GeV. The variable  $\sqrt{\hat{s}}$  is important because the effect of anomalous coupling increases with  $\sqrt{\hat{s}}$ . Figure 3.11 compares signal and background as a function of  $\sqrt{\hat{s}}$ . This figure shows why large  $\sqrt{\hat{s}}$  is interesting: The dependence on  $\Delta\kappa$  and  $\lambda$  is stronger, and the signal-to-background ratio is larger, for large  $\sqrt{\hat{s}}$ . Figure 3.12 compares signal and background for  $\sqrt{\hat{s}} > 340$  GeV. On the other hand, this energy cut reduces drastically the total number of events, so it becomes a question of detailed calculation to see whether it is a real advantage, given the available luminosity. Our calculation is for  $\sqrt{s} = 2$  TeV. A  $p\bar{p}$  collider with higher center-of-mass energy would produce more events in the interesting region of phase space with large  $\sqrt{\hat{s}}$ , and provide stronger tests of the anomalous  $WWV$  couplings.

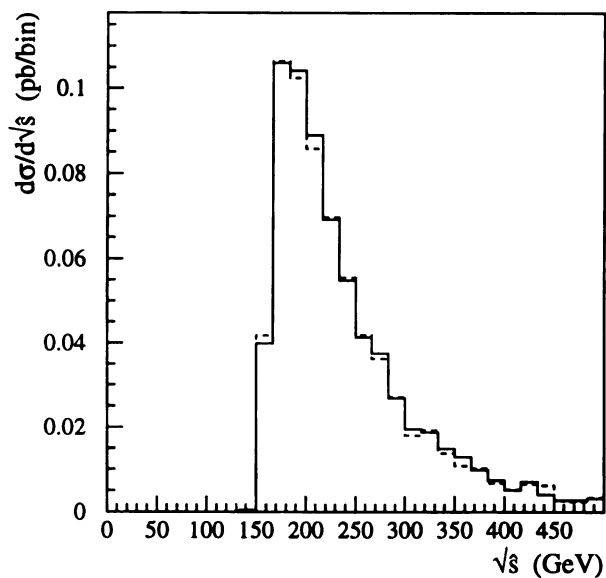


Figure 3.10:  $\sqrt{\hat{s}}$  distribution for the signal process. The solid line is the result of the complete calculation of the pure electroweak process  $p + \bar{p} \rightarrow q\bar{q}'W^+$ , with  $W^+ \rightarrow \bar{\ell}\nu_{\ell}$ ; the dotted line is the result of the calculation of  $W^+W^-$  production, with  $W^+ \rightarrow \bar{\ell}\nu_{\ell}$  and  $W^- \rightarrow 2 \text{ jets}$ , with a cut on the two-jet invariant mass ( $70 < M_{2j} < 90 \text{ GeV}$ ).

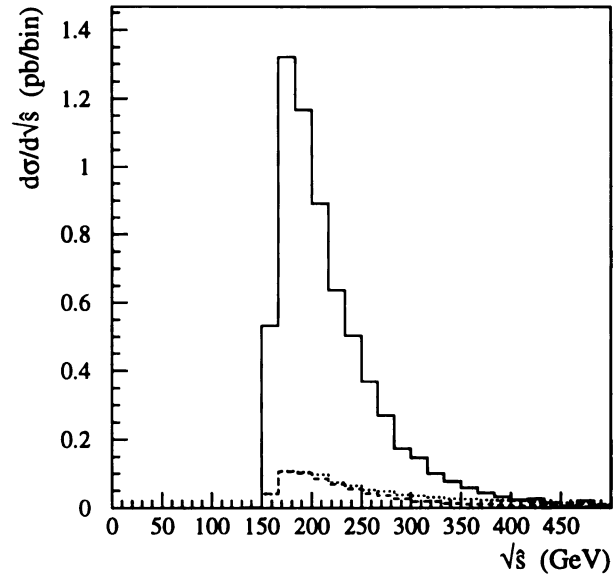


Figure 3.11: Comparison of  $\sqrt{s}$  distributions for signal and background processes. The solid line is the QCD background. The dotted line is the electroweak process, with zero anomalous couplings; the dashed line is the electroweak process with  $\Delta\kappa_\gamma = \Delta\kappa_Z = 0.5$ .

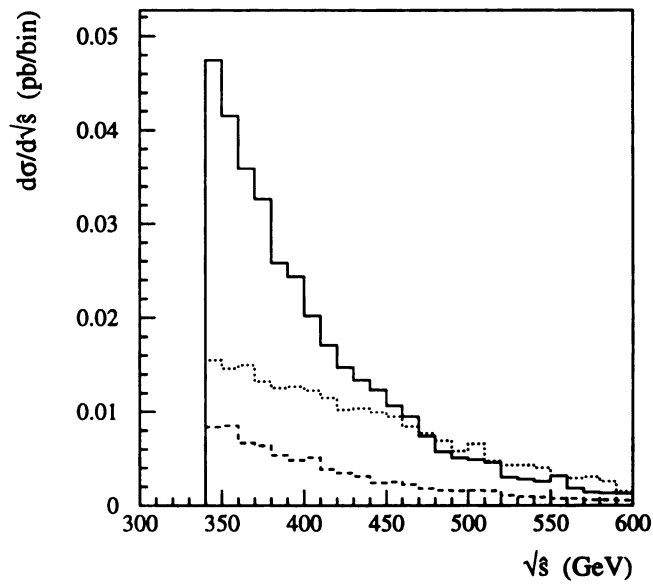


Figure 3.12: Comparison of  $\sqrt{\hat{s}}$  distributions for signal and background processes, for  $\sqrt{\hat{s}} > 340$  GeV. The solid line is the QCD background. The dotted line is the electroweak process, with zero anomalous couplings; the dashed line is the electroweak process with  $\Delta\kappa_\gamma = \Delta\kappa_Z = 0.5$ .

It is difficult to determine  $\sqrt{\hat{s}}$  accurately in an experimental event, because that requires measurement of jet momenta and missing neutrino momentum. The  $z$ -component of the neutrino momentum  $p_{\nu z}$  can be obtained up to a two-fold ambiguity by solving the mass constraint for the  $W$ -boson,  $M_W^2 = (p_\ell + p_\nu)^2$ . One way to choose  $p_{\nu z}$  is to select the solution with smaller absolute value, because a hard scattering process tends to produce final products in the central rapidity region with large transverse momenta. Given  $p_{\nu z}$  it is straightforward to calculate  $\sqrt{\hat{s}}$  from the 4-momenta of  $\ell, \nu$ , and the 2 jets. An alternative way to select large  $\sqrt{\hat{s}}$  is to require large transverse mass of the final state of the hard scattering process [34]. However, we have not pursued these approaches in this work.

### 3.3.2 Results

For the cross-section calculations that follow, we set  $Q = \sqrt{\hat{s}}$ , where  $Q$  is the momentum scale used in the parton distribution functions. The uncertainties we quote are only the statistical Monte-Carlo uncertainties. The theoretical uncertainty due to the choice of  $Q$  scale is discussed briefly later. The cross-section includes the branching ratio  $2/9$  for leptonic decay of one  $W$  into either electron or muon plus neutrino. The cross-section also includes the branching ratio  $6/9$  for 2-jet decay of the other  $W$ ,  $W^+ \rightarrow u\bar{d}$  and  $W^+ \rightarrow c\bar{s}$ . (Again, we ignore CKM mixing.) The overall branching ratio  $(2/9) \times (6/9) = 4/27$ , as well as the effect of the cuts of Eqs. (3.12)–(3.14), are always included in the cross-sections reported hereafter for  $W^+W^-$  production. Note that we consider separately the rates for  $\ell^+ + jets$  and  $\ell^- + jets$ .

Figures 3.13 to 3.15 show the results as plots of signal cross-section *vs* anomalous coupling parameters. Since our signal process involves the creation of a  $W^+W^-$  pair with subsequent decays of the  $W^+$  and  $W^-$ , the signal cross-section is the same

regardless of which  $W$  decays to leptons, in the narrow-width approximation. This is not true of the background cross-section, when the proton beam is polarized. (For *unpolarized* scattering the production rates of  $W^+$  and  $W^-$  are equal by CP invariance; but for scattering of polarized protons on unpolarized antiprotons, CP invariance does not apply.) For instance, for a left-handed proton the background process  $p(L) + \bar{p} \rightarrow W^+ + 2 \text{ jets}$  has a larger rate than  $p(L) + \bar{p} \rightarrow W^- + 2 \text{ jets}$ , because the probability of finding  $u(L)$  (which produces  $W^+$ ) inside  $p(L)$  is larger than  $d(L)$  (which produces  $W^-$ ), as implied by Fig. 3.1. (Remember that  $u(R)$  and  $d(R)$  do not contribute to the constituent cross-section of the  $W^\pm + 2 \text{ jets}$  background process because the weak charged current is left-handed.) Thus we may calculate the  $W^+ + 2 \text{ jets}$  and  $W^- + 2 \text{ jets}$  possible backgrounds, and then choose the  $W$  charge for which the background cross-section is smaller. Since the signal process is symmetric with respect to the charge of the  $W$  that decays leptonically, the process with the smaller background has a better signal-to-background ratio. In light of the cross-section inequalities mentioned above, it is advantageous experimentally to observe the  $W^-(\rightarrow \ell\bar{\nu}) + 2 \text{ jets}$  mode for a left-polarized proton beam, and similarly the  $W^+(\rightarrow \bar{\ell}\nu) + 2 \text{ jets}$  for a right-polarized proton beam. Hereafter we apply this strategy when comparing signal and background rates in the tables.

The program we have used to calculate the electroweak+QCD background, which comes from many processes [33], is set up to calculate the cross-section for production of  $W^- + 2 \text{ jets}$ . To find the cross-section for production of  $W^+ + 2 \text{ jets}$ , we calculate the rate for  $W^-$  production with polarized *anti-protons*, which is equal to the rate we want by the approximate CP invariance of the SM:

$$\sigma(p + \bar{p}(L) \rightarrow W^- + 2 \text{ jets}) = \sigma(p(R) + \bar{p} \rightarrow W^+ + 2 \text{ jets}) \quad (3.16)$$

$$\sigma(p + \bar{p}(R) \rightarrow W^- + 2 \text{ jets}) = \sigma(p(L) + \bar{p} \rightarrow W^+ + 2 \text{ jets}) \quad (3.17)$$

Tables 3.4 to 3.8 give the calculated cross-sections. Table 3.8 lists the background

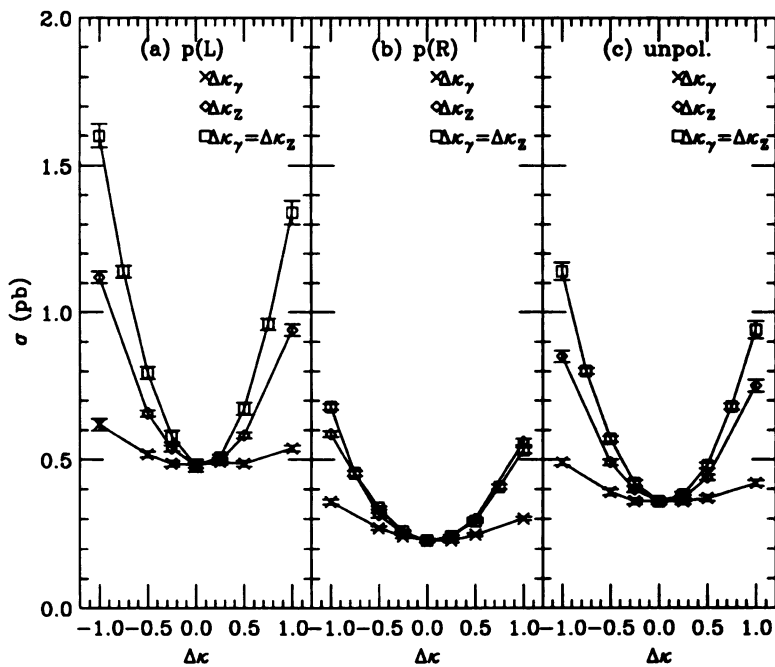


Figure 3.13: Electroweak cross-section for  $p_\lambda \bar{p} \rightarrow W^+ W^-$  as a function of anomalous couplings  $\Delta\kappa$ , for polarized ( $L, R$ ) and unpolarized protons. For each polarization, three cases are shown, corresponding to assumptions ( $\times$ )  $\Delta\kappa_\gamma \neq 0$  and  $\Delta\kappa_Z = 0$ , ( $\diamond$ )  $\Delta\kappa_\gamma = 0$  and  $\Delta\kappa_Z \neq 0$ , and ( $\square$ )  $\Delta\kappa_\gamma = \Delta\kappa_Z$ . In all cases  $\lambda_\gamma = \lambda_Z = 0$ .

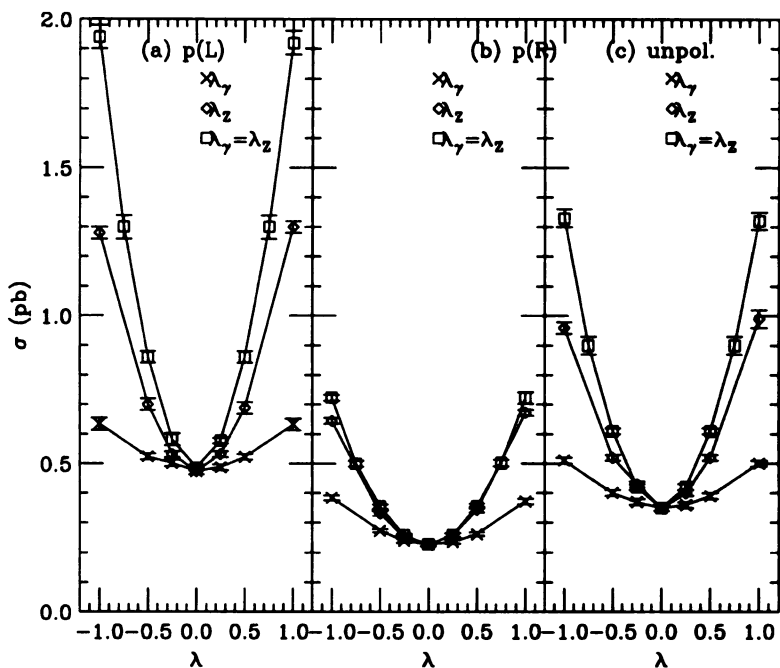


Figure 3.14: Electroweak cross-section for  $p_\lambda \bar{p} \rightarrow W^+ W^-$  as a function of anomalous couplings  $\lambda$ , for polarized ( $L, R$ ) and unpolarized protons. For each polarization, three cases are shown, corresponding to assumptions ( $\times$ )  $\lambda_\gamma \neq 0$  and  $\lambda_Z = 0$ , ( $\diamond$ )  $\lambda_\gamma = 0$  and  $\lambda_Z \neq 0$ , and ( $\square$ )  $\lambda_\gamma = \lambda_Z$ . In all cases  $\Delta\kappa_\gamma = \Delta\kappa_Z = 0$ .

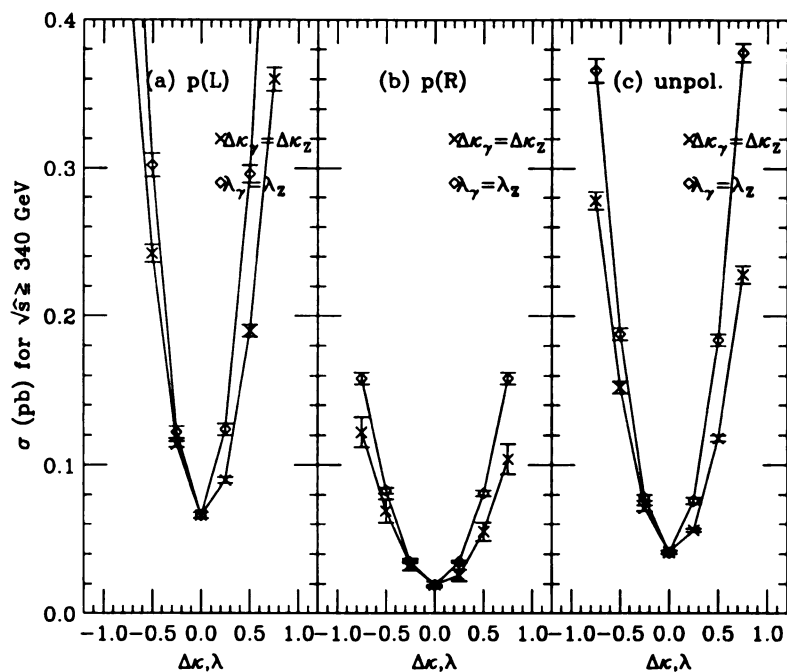


Figure 3.15: Electroweak cross-section for  $p_\lambda \bar{p} \rightarrow W^+ W^-$  as a function of anomalous couplings, with  $\sqrt{s} > 340$  GeV. For each polarization, two cases are shown, corresponding to assumptions ( $\times$ )  $\Delta\kappa_\gamma = \Delta\kappa_Z$  with  $\lambda_\gamma = \lambda_Z = 0$ , and ( $\diamond$ )  $\lambda_\gamma = \lambda_Z$  with  $\Delta\kappa_\gamma = \Delta\kappa_Z = 0$ .

cross-sections for different proton helicities. As expected,  $\sigma(L)$  is larger than  $\sigma(R)$  for  $W^+$  production: the  $W^+$  must come from a  $u(L)$ , and the density of  $u(L)$  is larger in  $p(L)$  than in  $p(R)$ . On the other hand,  $\sigma(L)$  is *smaller* than  $\sigma(R)$  for  $W^-$  production: the  $W^-$  must come from a  $d(L)$ , and the density of  $d(L)$  is *smaller* in  $p(L)$  than in  $p(R)$ , because  $\Delta d(x)$  is mostly negative, as shown in Fig. 3.1.

Table 3.8 lists cross-sections calculated using the polarized parton distribution functions of Section 3.1, and also, for comparison, unpolarized cross-sections calculated using CTEQ2 parton distribution functions [35]. We have used the leading-order set CTEQ2L for our studies. The CTEQ2 results are consistent with the average of the two proton helicities, within the uncertainty of the Monte Carlo calculations.

### 3.3.3 Limits on $\Delta\kappa_\gamma$ , $\Delta\kappa_Z$ , $\lambda_\gamma$ , and $\lambda_Z$

We estimate limits on anomalous couplings that could be set by experiments at  $\sqrt{s} = 2$  TeV. Since there is a large background for this process, the limits depend on the background cross-section  $\sigma_B$ . Again, as in our previous analyses, we assume that in an experiment with  $N$  events the standard deviation of  $N$  is  $\delta N = \sqrt{N}$ . At the three-sigma confidence level, the uncertainty of  $\sigma$  is

$$\delta\sigma_3 = 3\sqrt{\frac{\sigma}{L}}, \quad (3.18)$$

which is the same as in Chapter 2, except that here  $\sigma$  is the sum of signal and background cross-sections. We consider integrated luminosity  $L = 1 \text{ fb}^{-1}$  and  $L = 10 \text{ fb}^{-1}$ .

To calculate the limit that could be set on an anomalous coupling parameter, *e.g.*  $\Delta\kappa_\gamma$ , assuming the actual value of the parameter is zero, we compare the statistical uncertainty  $\delta\sigma_3$  to the variation of the calculated cross-section as a function of  $\Delta\kappa_\gamma$ .

At the three-sigma confidence level,  $\Delta\kappa_\gamma$  is in the range with

$$|\sigma(\Delta\kappa_\gamma) - \sigma(\Delta\kappa_\gamma = 0)| < \delta\sigma_3 . \quad (3.19)$$

For example, Figure 3.13c shows  $\sigma$  vs  $\Delta\kappa$  for unpolarized scattering. Three possibilities are shown: (i) the effect of  $\Delta\kappa_\gamma$  with  $\Delta\kappa_Z = 0$ , (ii) the effect of  $\Delta\kappa_Z$  with  $\Delta\kappa_\gamma = 0$ , and (iii) the effect if  $\Delta\kappa_\gamma = \Delta\kappa_Z$ . The background cross-section is given in Table 3.8. Then Tables 3.9 and 3.10 list the limits that could be set on  $\Delta\kappa$  (and also  $\lambda$ ) for these three cases. The estimated limits in Table 3.9 are from events with arbitrary  $\sqrt{\hat{s}}$ , and the limits in Table 3.10 are from events with  $\sqrt{\hat{s}} > 340$  GeV.

Our purpose is to determine whether measurement of the cross-section with polarized protons leads to stronger limits on anomalous couplings than with unpolarized protons. Tables 3.9 and 3.10 show that the limit is stronger with polarized protons, assuming the same integrated luminosity as for unpolarized scattering. The constraints on either  $\Delta\kappa_\gamma$  or  $\lambda_\gamma$  alone from the  $W^+W^-$  channel are not as strong as those obtained from studying the  $W^+\gamma$  channel. Though the total  $W\gamma$  cross section is much larger than the  $W^+W^-$  cross section, after including the  $W$  decays and cuts the signal cross sections are comparable (unpolarized cross sections 0.47 and 0.7 pb, for  $W\gamma$  and  $W^+W^-$ , respectively). Therefore the superior sensitivity of the  $W\gamma$  channel in our study is not explained by a large cross section for that channel. The  $W\gamma$  channel is more sensitive to the *photon* couplings simply because no  $Z$  couplings contribute to the event rate. In other words, some of the  $WW$  events are due to  $Z$  interactions, which are independent of the photon couplings, so a given anomalous *photon* coupling will result in a smaller fractional deviation from the SM event rate. The  $W\gamma$  and  $WW$  channels are therefore complementary, since the  $WW$  channel probes both  $W$  and photon couplings, without distinguishing between them, while the  $W\gamma$  channel limits only the photon couplings.

The constraints on  $\Delta\kappa_Z$  and  $\lambda_Z$  are about a factor of 2 better than those on

$\Delta\kappa_\gamma$  and  $\lambda_\gamma$  from the  $W^+W^-$  channel. For models with a linear SU(2) symmetry, such that  $\kappa_\gamma = \kappa_Z$  and  $\lambda_\gamma = \lambda_Z$ , the constraint on  $\Delta\kappa_\gamma$  is about a factor of 2 better than from the  $W^+\gamma$  channel, while the constraint on  $\lambda_\gamma$  is about the same as from the  $W^+\gamma$  channel, after selecting the large  $\sqrt{\hat{s}}$  region. In general, selecting large  $\sqrt{\hat{s}}$  ( $> 340$  GeV) improves the significance of signal to background by about a factor of 2.

### 3.3.4 Interpretation of the Results

The limits described above show how this process,  $W^+W^-$  production with polarized protons, tests the  $WWV$  vertex. The estimated limits on anomalous couplings include only simple statistical uncertainty, based on Poisson statistics ( $\delta N = \sqrt{N}$ ); they do not include experimental uncertainty due to detector inefficiency or theoretical uncertainty of parton distribution functions or  $Q$  scale.

For example, the background calculation depends on the choice of parton momentum scale  $Q$ . Table 3.11 shows how the background cross-section, for unpolarized scattering, depends on the choice of  $Q$ . We used  $Q = \sqrt{\hat{s}}$  in our calculations.  $Q = 2M_W$  or  $Q = \sqrt{\hat{s}}/2$  would also be reasonable choices. The cross-sections for the three choices differ by about 20%. This theoretical uncertainty due to dependence on scale choice is larger than the statistical uncertainty estimated above. It is thus difficult to extract the signal cross-section unless the uncertainty in the background cross-section is reduced, by including higher-order QCD effects to reduce the dependence on  $Q$  scale. On the other hand, given large luminosity the details of the QCD background processes, *e.g.*, the shapes of  $\sqrt{\hat{s}}$  distributions, can be measured directly from data to discriminate between different theoretical predictions from different scale choices. Therefore we anticipate that background rates will eventually be better known, and allow us to extract signal rates.

Our purpose in this work is to study the effect of proton polarization. For this

study we have analysed only the *total cross-section* as a function of  $\Delta\kappa$  and  $\lambda$ . Stronger constraints on  $\Delta\kappa$  and  $\lambda$  may be set by analysing, as in Chapter 2, differential cross-sections with respect to variables for which the distribution of events is sensitive to  $\Delta\kappa$  or  $\lambda$  [30, 31]. It would be interesting to find kinematic variables *dependent on proton helicity* for which the distribution of events is sensitive to  $\Delta\kappa$  or  $\lambda$ , to further test the triple-boson couplings with polarized proton scattering.

### 3.4 Discussion and Conclusions

We have studied the potential of a polarized proton beam at the Tevatron collider for measuring the tri-boson couplings  $WW\gamma$  and  $WWZ$ . Because the polarized parton distribution functions in the relevant kinematic region (*i.e.*,  $x$ -values) are not yet precise enough to give definite detailed predictions about the rates of the signal and the backgrounds, we have concentrated on the comparisons between the total event rates from a polarized- and an unpolarized- proton beam. As summarized in Tables 3.3, 3.9 and 3.10, we found that with a polarized proton beam the limits on non-standard parameters  $\Delta\kappa_\gamma$ ,  $\lambda_\gamma$ ,  $\Delta\kappa_Z$  and  $\lambda_Z$  are somewhat improved compared to those obtained from an unpolarized proton beam. We anticipate that these results can be further improved by studying detailed distributions of relevant kinematic variables. Generally a factor of 2 improvement in measuring these non-standard parameters is expected, after selecting kinematic regions where the signal becomes more important, as illustrated in Tables 3.9 and 3.10.

One interesting feature that we found about the polarized collider program is that it is possible to select the polarization state of the proton beam to enhance the ratio of signal to background for a specific charge mode of the final state. This was demonstrated in studying the process  $p\bar{p} \rightarrow W^+W^- \rightarrow \ell^\pm \bar{\nu}_\ell + 2 \text{ jets}$ . For the

final state with a positive charged lepton ( $\ell^+$ ), one can select the polarization of the proton beam to be right-handed to improve the signal-to-background ratio because the QCD background process  $p(R)\bar{p} \rightarrow W^+(\rightarrow \ell^+ \nu_\ell) + 2 \text{ jets}$  has a smaller rate than  $p(L)\bar{p} \rightarrow W^+(\rightarrow \ell^+ \nu_\ell) + 2 \text{ jets}$ . The signal rate, in contrast, is independent of the charge mode of the isolated lepton from the  $W$ -boson decay because either  $W^+$  or  $W^-$  can decay into the charged lepton. We expect that similar tricks can be applied to other polarized physics measurements, such as the *lepton + jet* mode of the  $t\bar{t}$  pair production from  $q\bar{q}$  and  $gg$  fusion processes.

We are now in a position to compare the sensitivity of a Tevatron experiment with a polarized beam (“polarized Tevatron”) to those of the NLC and LEP II. Tables 2.2 and 2.3 show limits on anomalous photon couplings from LEP II and the NLC, calculated from the variation of the total cross section; and Tables 3.9 and 3.10 show limits from a polarized Tevatron. Comparing 3-sigma limits on  $\Delta\kappa_\gamma$  and  $\lambda_\gamma$ , it is immediately evident that the NLC is superior to the other colliders by about two orders of magnitude. The polarized Tevatron gives somewhat better limits than LEP II, especially when we capitalize on high energy events with greater dependence on anomalous couplings by cutting events with  $\sqrt{\hat{s}} < 340$  Gev. Note, however, that a complete analysis of an actual Tevatron experiment would have to include the contribution from  $WZ$  production, which depends on anomalous  $Z$  couplings. In addition, to extract such precise limits from the Tevatron one would have to reduce the momentum-scale choice uncertainty by calculating the next-to-leading-order corrections to the cross section. Due to the relatively wide range of center-of-mass energies for the Tevatron hard-scattering events, it would also be important to include the energy dependence of the anomalous couplings, especially if the scale of anomalous physics  $\Lambda$  (discussed in Chapter 1) were near its lower bound.

The Tevatron limits should improve mildly, as did those from the  $e^+e^-$  colliders, were we to use differential cross section information to calculate them, rather than merely the total cross section. However, reliable predictions of distributions of kinematic variables will require more precise polarized parton distribution functions. Measurements of polarized proton-antiproton reactions will yield new information on spin-dependent parton distributions. Thus the use of polarized scattering to test fundamental physics, and the determination of the spin structure of the proton, would proceed together. In the next chapter we investigate the potential improvement of ppdf accuracy from studying single- $W^\pm$  production with a polarized proton beam.

## Chapter 3 Tables

Table 3.1: Cross-section for the process  $p\bar{p} \rightarrow W^+\gamma$  with polarized protons, for different values of the anomalous coupling  $\Delta\kappa_\gamma$ , assuming  $\lambda_\gamma = 0$ . Cross-sections are in pb. The branching ratio  $2/9$  for  $W^+ \rightarrow e^+\nu_e$  or  $\mu^+\nu_\mu$ , and the effect of our cuts, is included. The unpolarized case was calculated separately using CTEQ2 parton distribution functions, for comparison. The asymmetry  $\mathcal{A}$ , defined in Eq. (3.7), is calculated by fitting the data to a parabola.

$p\lambda\bar{p} \rightarrow W^+\gamma$ cross-sections in pb				
$\Delta\kappa_\gamma$	p(R)	p(L)	Unpol	$\mathcal{A}$
2.0	$0.49 \pm 0.01$	$1.44 \pm 0.01$	$0.98 \pm 0.01$	0.514
1.5	$0.39 \pm 0.01$	$1.08 \pm 0.01$	$0.75 \pm 0.01$	0.504
1.0	$0.29 \pm 0.01$	$0.86 \pm 0.01$	$0.59 \pm 0.01$	0.491
0.5	$0.25 \pm 0.01$	$0.72 \pm 0.01$	$0.51 \pm 0.01$	0.480
0.0	$0.25 \pm 0.01$	$0.69 \pm 0.01$	$0.47 \pm 0.01$	0.475
-0.5	$0.27 \pm 0.01$	$0.75 \pm 0.01$	$0.54 \pm 0.01$	0.480
-1.0	$0.32 \pm 0.01$	$0.94 \pm 0.01$	$0.63 \pm 0.01$	0.491
-1.5	$0.41 \pm 0.01$	$1.23 \pm 0.01$	$0.83 \pm 0.01$	0.504
-2.0	$0.53 \pm 0.02$	$1.57 \pm 0.02$	$1.09 \pm 0.02$	0.514

Table 3.2: Cross-section for the process  $p\bar{p} \rightarrow W^+\gamma$  with polarized protons, for different values of the anomalous coupling  $\lambda_\gamma$ , assuming  $\Delta\kappa_\gamma = 0$ . Cross-sections are in pb. The unpolarized case was calculated separately using CTEQ2 parton distribution functions, for comparison. The asymmetry  $\mathcal{A}$ , defined in Eq. (3.7), is calculated by fitting the data to a parabola.

$p\lambda\bar{p} \rightarrow W^+\gamma$ cross-sections in pb.				
$\lambda_\gamma$	p(R)	p(L)	Unpol	$\mathcal{A}$
2.0	$1.73 \pm 0.03$	$7.47 \pm 0.03$	$4.55 \pm 0.03$	0.613
1.5	$1.11 \pm 0.02$	$4.47 \pm 0.02$	$2.72 \pm 0.02$	0.602
1.0	$0.62 \pm 0.01$	$2.32 \pm 0.01$	$1.50 \pm 0.01$	0.580
0.5	$0.35 \pm 0.03$	$1.14 \pm 0.03$	$0.75 \pm 0.03$	0.530
0.0	$0.24 \pm 0.01$	$0.68 \pm 0.01$	$0.49 \pm 0.01$	0.478
-0.5	$0.34 \pm 0.01$	$1.05 \pm 0.01$	$0.71 \pm 0.01$	0.530
-1.0	$0.57 \pm 0.01$	$2.19 \pm 0.01$	$1.39 \pm 0.01$	0.580
-1.5	$0.99 \pm 0.03$	$4.13 \pm 0.03$	$2.59 \pm 0.03$	0.602
-2.0	$1.64 \pm 0.03$	$6.87 \pm 0.03$	$4.16 \pm 0.03$	0.613

**Table 3.3:** Limits on non-Standard couplings, from  $p\bar{p} \rightarrow W^+\gamma$  with polarized and unpolarized protons. The upper number is for  $1 \text{ fb}^{-1}$  integrated luminosity, and the lower number (in parentheses) is for  $10 \text{ fb}^{-1}$ .

Parameter	Limits		
	$p(R)$	$p(L)$	Unpol
$\Delta\kappa_\gamma$	$\pm 0.89$ ( $\pm 0.50$ )	$\pm 0.62$ ( $\pm 0.35$ )	$\pm 0.70$ ( $\pm 0.39$ )
$\lambda_\gamma$	$\pm 0.36$ ( $\pm 0.20$ )	$\pm 0.22$ ( $\pm 0.13$ )	$\pm 0.26$ ( $\pm 0.14$ )

Table 3.4: Purely electroweak cross-sections, in pb, for  $p(R)\bar{p} \rightarrow W^+ + 2 \text{ jets}$ , with  $W^+ \rightarrow \bar{\ell}\nu$  where  $\ell = e$  or  $\mu$ ; the proton is right-handed. The cross-section for  $p(R)\bar{p} \rightarrow W^- + 2 \text{ jets}$  is the same. The branching ratio  $(2/9) \times (6/9) = 4/27$  and the effect of our cuts are included.

<i>Electroweak cross-sections in pb; right-polarized proton.</i>			
Value	Varied parameter		
	$\Delta\kappa_\gamma$	$\Delta\kappa_Z$	$\Delta\kappa_\gamma = \Delta\kappa_Z$
1.00	0.604±.012	1.120±.020	1.064±.020
0.75	0.534±.012	0.774±.016	0.816±.016
0.50	0.496±.012	0.600±.012	0.588±.012
0.25	0.456±.012	0.484±.012	0.484±.012
0.00	0.456±.012	0.456±.012	0.456±.012
-0.25	0.484±.012	0.508±.012	0.516±.012
-0.50	0.540±.012	0.628±.012	0.676±.012
-0.75	0.620±.012	0.822±.014	0.908±.016
-1.00	0.716±.016	1.172±.024	1.356±.028
	$\lambda_\gamma$	$\lambda_Z$	$\lambda_\gamma = \lambda_Z$
1.00	0.740±.020	1.344±.028	1.444±.032
0.75	0.602±.014	0.952±.018	1.004±.020
0.50	0.524±.012	0.688±.016	0.712±.016
0.25	0.472±.012	0.520±.012	0.520±.012
0.00	0.456±.012	0.456±.012	0.456±.012
-0.25	0.480±.012	0.504±.012	0.516±.012
-0.50	0.548±.012	0.664±.016	0.708±.016
-0.75	0.642±.016	0.920±.018	1.000±.020
-1.00	0.768±.016	1.288±.024	1.444±.028

Table 3.5: Purely electroweak cross-sections, in pb, for  $p(L)\bar{p} \rightarrow W^+ + 2 \text{ jets}$ , with  $W^+ \rightarrow \bar{\ell}\nu$  where  $\ell = e$  or  $\mu$ ; the proton is left-handed. The cross-section for  $p(L)\bar{p} \rightarrow W^- + 2 \text{ jets}$  is the same. The branching ratio  $(2/9) \times (6/9) = 4/27$  and the effect of our cuts are included.

<i>Electroweak cross-sections in pb; left-polarized proton.</i>						
Value	Varied quantity					
	$\Delta\kappa_\gamma$	$\Delta\kappa_Z$	$\Delta\kappa_\gamma = \Delta\kappa_Z$	$\lambda_\gamma$	$\lambda_Z$	$\lambda_\gamma = \lambda_Z$
1.00	1.08±.02	1.88±.04	2.68±.08	1.26±.04	2.60±.04	3.84±.08
0.75	1.02±.02	1.48±.04	1.92±.04	1.10±.02	1.84±.04	2.60±.08
0.50	0.98±.02	1.16±.02	1.34±.04	1.04±.02	1.38±.04	1.72±.08
0.25	0.98±.02	1.00±.02	1.02±.02	0.98±.02	1.06±.02	1.16±.02
0.00	0.96±.02	0.96±.02	0.96±.02	0.94±.02	0.94±.02	0.98±.02
-0.25	0.98±.02	1.08±.02	1.16±.04	1.00±.02	1.06±.02	1.16±.04
-0.50	1.04±.02	1.32±.02	1.58±.04	1.04±.02	1.40±.04	1.72±.04
-0.75	1.14±.02	1.72±.04	2.28±.04	1.14±.02	1.86±.04	2.60±.08
-1.00	1.24±.04	2.24±.04	3.20±.08	1.26±.04	2.56±.04	3.88±.08

Table 3.6: Purely electroweak cross-sections, in pb, for  $p\bar{p} \rightarrow W^+ + 2 \text{ jets}$ , with  $W^+ \rightarrow \bar{\ell}\nu$  where  $\ell = e$  or  $\mu$ ; the proton is unpolarized. The cross-section for  $p\bar{p} \rightarrow W^- + 2 \text{ jets}$  is the same. The branching ratio  $(2/9) \times (6/9) = 4/27$  and the effect of our cuts are included. These values were calculated independently using the Morfin-Tung ppdf's; the cross-section for unpolarized protons is equal to the average of cross-section for left and right polarized protons.

<i>Electroweak cross-sections in pb; unpolarized proton</i>						
Value	Varied quantity					
	$\Delta\kappa_\gamma$	$\Delta\kappa_Z$	$\Delta\kappa_\gamma = \Delta\kappa_Z$	$\lambda_\gamma$	$\lambda_Z$	$\lambda_\gamma = \lambda_Z$
1.00	0.84±.02	1.50±.04	1.88±.06	1.00±.02	1.98±.06	2.64±.06
0.75	0.78±.02	1.14±.02	1.36±.02	0.86±.02	1.40±.04	1.80±.06
0.50	0.74±.02	0.88±.02	0.96±.02	0.78±.02	1.04±.02	1.22±.02
0.25	0.72±.02	0.74±.02	0.76±.02	0.72±.02	0.80±.02	0.84±.02
0.00	0.72±.02	0.72±.02	0.72±.02	0.70±.02	0.70±.02	0.70±.02
-0.25	0.72±.02	0.80±.02	0.84±.02	0.74±.02	0.86±.02	0.84±.02
-0.50	0.78±.02	0.98±.02	1.14±.02	0.80±.02	1.04±.02	1.22±.02
-0.75	0.88±.02	1.28±.02	1.60±.02	0.88±.02	1.38±.04	1.80±.06
-1.00	0.98±.02	1.70±.04	2.28±.06	1.02±.02	1.92±.04	2.66±.06

Table 3.7: Electroweak cross-sections, in pb, for  $W^+W^-$  production with non-Standard couplings, with polarized or unpolarized protons, and with a large- $\sqrt{s}$  cut,  $\sqrt{s} > 340$  GeV. One  $W$  decays leptonically, the other to 2 jets, and the branching ratio 4/27 and the effect of our cuts are included in the cross-section. Two assumptions on non-Standard couplings are listed:  $\Delta\kappa_\gamma = \Delta\kappa_Z$  with  $\lambda_\gamma = \lambda_Z = 0$ , and  $\lambda_\gamma = \lambda_Z$  with  $\Delta\kappa_\gamma = \Delta\kappa_Z = 0$ .

<i>Electroweak cross-sections</i>			
<i>in pb, with <math>\sqrt{s} &gt; 340</math> GeV</i>			
Value	Varied parameter		
	$\Delta\kappa_\gamma = \Delta\kappa_Z$		
	$p(L)$	$p(R)$	Unpol
0.75	0.720±.016	0.208±.004	0.456±.012
0.50	0.380±.008	0.110±.002	0.236±.004
0.25	0.180±.004	0.052±.002	0.112±.002
0.00	0.132±.004	0.038±.002	0.082±.002
-0.25	0.228±.004	0.066±.002	0.142±.004
-0.50	0.484±.012	0.138±.002	0.304±.008
-0.75	0.876±.016	0.244±.004	0.556±.012
	$\lambda_\gamma = \lambda_Z$		
	$p(L)$	$p(R)$	Unpol
0.75	1.196±.028	0.316±.008	0.756±.012
0.50	0.592±.012	0.162±.004	0.368±.008
0.25	0.248±.008	0.070±.002	0.152±.004
0.00	0.132±.004	0.038±.000	0.082±.002
-0.25	0.244±.008	0.070±.002	0.156±.004
-0.50	0.604±.016	0.166±.004	0.376±.008
-0.75	1.160±.028	0.316±.008	0.732±.016

Table 3.8: QCD background cross-sections for  $p\bar{p} \rightarrow W^\pm + 2 \text{ jets}$ , for various proton polarizations and kinematic cuts. The unpolarized cases  $\sigma(p\bar{p} \rightarrow W^+ 2j) = \sigma(p\bar{p} \rightarrow W^- 2j)$  were calculated separately using CTEQ2 parton distribution functions.

<i>W+2 jet Background</i>	
process	$\sigma$ (pb)
<i>without 2 jet mass cut:</i>	
$p(R)\bar{p} \rightarrow W^- 2j$	$50.56 \pm .58$
$p(L)\bar{p} \rightarrow W^- 2j$	$41.36 \pm .52$
$p(L)\bar{p} \rightarrow W^+ 2j$	$65.46 \pm .78$
$p(R)\bar{p} \rightarrow W^+ 2j$	$26.84 \pm .28$
$p\bar{p} \rightarrow W^+ 2j$	$45.30 \pm .50$
<i>with 2 jet mass cut (70-90 GeV):</i>	
$p(R)\bar{p} \rightarrow W^- 2j$	$7.324 \pm .070$
$p(L)\bar{p} \rightarrow W^- 2j$	$5.910 \pm .056$
$p(L)\bar{p} \rightarrow W^+ 2j$	$9.404 \pm .092$
$p(R)\bar{p} \rightarrow W^+ 2j$	$3.874 \pm .034$
$p\bar{p} \rightarrow W^+ 2j$	$6.514 \pm .060$
<i>with 2 jet mass cut and <math>\sqrt{s} &gt; 340</math> GeV:</i>	
$p(R)\bar{p} \rightarrow W^- 2j$	$0.348 \pm .004$
$p(L)\bar{p} \rightarrow W^- 2j$	$0.308 \pm .004$
$p(L)\bar{p} \rightarrow W^+ 2j$	$0.520 \pm .004$
$p(R)\bar{p} \rightarrow W^+ 2j$	$0.144 \pm .004$
$p\bar{p} \rightarrow W^+ 2j$	$0.358 \pm .002$

Table 3.9: Limits on anomalous couplings that could be set from  $p\bar{p} \rightarrow W^\pm + 2 \text{ jets}$  with polarized or unpolarized protons. The numbers in parentheses are for  $10 \text{ fb}^{-1}$  integrated luminosity, and the other numbers are for  $1 \text{ fb}^{-1}$  integrated luminosity.

Parameter	Limits		
	$p(R)$	$p(L)$	Unpol
$\Delta\kappa_\gamma$	$\pm 0.89$	$\pm 1.10$	$\pm 1.06$
$\Delta\kappa_Z$	$\pm 0.56$	$\pm 0.47$	$\pm 0.54$
$\Delta\kappa_\gamma = \Delta\kappa_Z$	$\pm 0.53$	$\pm 0.35$	$\pm 0.44$
	( $\pm 0.30$ )	( $\pm 0.20$ )	( $\pm 0.24$ )
$\lambda_\gamma$	$\pm 0.79$	$\pm 0.77$	$\pm 0.83$
$\lambda_Z$	$\pm 0.47$	$\pm 0.37$	$\pm 0.44$
$\lambda_\gamma = \lambda_Z$	$\pm 0.44$	$\pm 0.29$	$\pm 0.36$
	( $\pm 0.25$ )	( $\pm 0.16$ )	( $\pm 0.20$ )

Table 3.10: Limits on anomalous couplings that could be set from  $p\bar{p} \rightarrow W^\pm + 2 \text{ jets}$  with polarized or unpolarized protons, from events with  $\sqrt{\hat{s}} > 340$  GeV. The numbers in parentheses are for  $10 \text{ fb}^{-1}$  integrated luminosity, and the other numbers are for  $1 \text{ fb}^{-1}$  integrated luminosity.

Parameter	Limits		
	$p(R)$	$p(L)$	Unpol
$\Delta\kappa_\gamma = \Delta\kappa_Z$	$\pm 0.34$ ( $\pm 0.19$ )	$\pm 0.23$ ( $\pm 0.13$ )	$\pm 0.28$ ( $\pm 0.16$ )
$\lambda_\gamma = \lambda_Z$	$\pm 0.28$ ( $\pm 0.16$ )	$\pm 0.18$ ( $\pm 0.10$ )	$\pm 0.23$ ( $\pm 0.13$ )

Table 3.11: Effect of parton  $Q$  scale on the calculated cross-section for background processes  $p\bar{p} \rightarrow W^\pm + 2 \text{ jets}$ . These are unpolarized cross-sections, calculated with CTEQ2 parton distribution functions.

$Q$ scale	$\sigma$ (pb)
$\sqrt{\hat{s}}$	$6.420 \pm .056$
$\sqrt{\hat{s}}/2$	$8.538 \pm .074$
$2M_W$	$7.398 \pm .068$

# Chapter 4

## Probing the Polarized Parton Distributions with $p\bar{p} \rightarrow W$

### 4.1 Introduction

In the preceding chapter we examined the potential of a Tevatron with a polarized proton beam for studying anomalous electroweak physics. Other possible physics topics to explore with a polarized beam are outlined in Reference [24]. However, in order to use polarized  $p\bar{p}$  scattering as a probe of interesting physics, it would be necessary to know accurately the parton distribution functions for polarized protons.

Polarized parton distribution functions (hereafter abbreviated ppdf's) have been measured to some accuracy in deep-inelastic polarized lepton scattering [36, 27, 28]. These experiments have revealed the spin structure of the proton, which is interesting in its own right. Several parametrizations of ppdf's have been published [37, 26, 38, 39] based on this data. The purpose of this chapter is to examine whether single- $W^\pm$  production in polarized  $p\bar{p}$  collisions, with longitudinally polarized protons, could be used as another, complementary, method to constrain the ppdf's.

With the Tevatron collider in mind [23], we consider the center-of-mass energy equal to 2 TeV.<sup>†</sup>

---

<sup>†</sup>After this work was completed, we learned that a polarized colliding beam is less likely to

The idea to study ppdf's from the effect of proton polarization on the process  $p + \bar{p} \rightarrow W^\pm$  has been considered previously, in Ref. [40], in which the cross-section for producing  $W^\pm$  was calculated, treating the  $W^\pm$  as a stable particle. Here we will take into account also the leptonic decay  $W^\pm \rightarrow e^\pm + \bar{\nu}_e^{(-)}$ , including a possible kinematic cut on  $p_T$  of the  $e^\pm$ ; *i.e.*, we are concerned with the experimentally measurable processes  $p + \bar{p} \rightarrow (W^\pm \rightarrow e^\pm + \bar{\nu}_e^{(-)}) + X$ .

The cross-section for  $W^\pm$  production depends strongly on the helicities of the quarks. For massless quarks a  $W^\pm$  couples only to left-handed ( $L$ ) quarks and right-handed ( $R$ ) antiquarks, because of the V–A form of the weak coupling. We know that the densities of  $L$  and  $R$  quarks in a proton depend on the proton helicity. Therefore, the cross-section for  $p_\lambda + \bar{p} \rightarrow W^\pm$ , where  $\lambda = L$  or  $R$  indicates the helicity of the proton, depends on  $\lambda$ . Measurement of the polarization dependence would provide some information on the ppdf's. The question which motivates our study is whether such data could determine the ppdf's accurately.

The ppdf's are defined as follows: For any parton type  $f$ , we define

$$\begin{aligned} f_+(x) &= \frac{1}{2}(f(x) + \Delta f(x)) \\ &= \text{density of L (or R) partons in a L (or R) proton,} \\ f_-(x) &= \frac{1}{2}(f(x) - \Delta f(x)) \\ &= \text{density of L (or R) partons in a R (or L) proton,} \end{aligned}$$

where  $x$  is the momentum fraction of the parton. Thus  $\Delta f(x)$  is the difference between partons with the same helicity as the proton and partons with opposite helicity. There are 13 different parton types

$$f = g, u, d, s, c, b, t, \bar{u}, \bar{d}, \bar{s}, \bar{c}, \bar{b}, \bar{t} .$$

---

be built in the near future at the Tevatron. However, since a polarized collider is technically feasible, we believe it is still interesting, and potentially useful, to explore theoretically the possible experiments with such a machine.

In our calculations we neglect the  $b, \bar{b}$  and  $t, \bar{t}$  distributions. Also, the gluon distribution does not contribute in our calculation, which is only a tree-level calculation.

We have used two recently published parametrizations of ppdf's [38, 39]. (Specifically, we use set 2 from Ref. [38] and set B from Ref. [39].) We calculated these ppdf's with a computer program written by Dr. Glenn Ladinsky. Figure 4.1 shows  $x \Delta f(x)$  vs  $x$  for  $f = u$  and  $d$ . The ppdf's depend on momentum scale  $Q$ ; i.e.,  $f_{\pm} = f_{\pm}(x, Q)$ . Figure 4.1 is for  $Q=5$  GeV. These distributions were constructed by fitting to data for the polarized structure function  $g_1^p(x, Q)$ ; in the parton model

$$g_1^p(x, Q) = \frac{1}{2} \sum_q e_q^2 [\Delta q(x, Q) + \Delta \bar{q}(x, Q)] . \quad (4.1)$$

Figure 4.2 shows plots of  $xg_1^p(x, Q)$  vs  $x$  calculated from the two sets of ppdf's we used, again for  $Q = 5$  GeV.

The difference between the two parametrizations of ppdf's, illustrated in Figs. 4.1 and 4.2, indicates the uncertainty of our current knowledge of the ppdf's. Either parametrization is a reasonable fit to existing data from polarized deep-inelastic lepton scattering, within the uncertainty of the data. We will use the difference between these two sets of ppdf's to gauge the current uncertainty of the ppdf's. We will consider whether measurements of  $W^{\pm}$  production in  $p_{\lambda} \bar{p}$  collisions could be used to reduce this uncertainty.

## 4.2 $W^{\pm}$ production

In the parton model, the cross-section for  $p_{\lambda} + \bar{p} \rightarrow W^+ + X$ , where  $\lambda$  is  $L$  or  $R$  for left-handed or right-handed protons, with subsequent decay  $W^+ \rightarrow e^+ + \nu_e$ , is expressed as

$$\sigma(\lambda) = \frac{1}{2} \int_0^1 dx dx' [\hat{\sigma}_{LR}(xP, x'P') u_{\pm}(x) d(x') + \hat{\sigma}_{LR}(x'P', xP) \bar{d}_{\mp}(x) \bar{u}(x')] \quad (4.2)$$

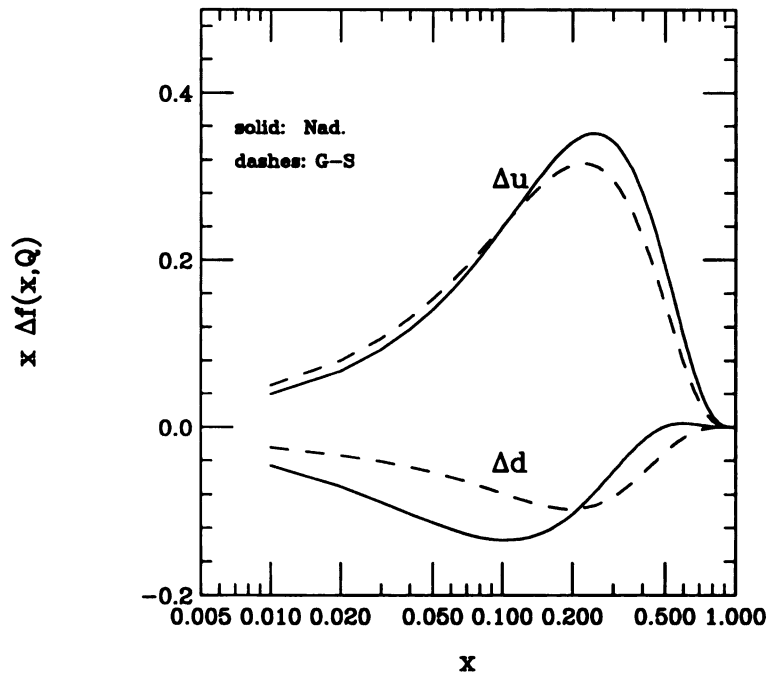


Figure 4.1: Polarized parton distribution functions. The curves are  $x\Delta f(x)$  vs  $x$  for parton types  $u$  and  $d$ , which are the most important partons in our calculations, for two sets of polarized parton distribution functions. The solid curve is the Nadolsky parametrization [38] and the dashed curve is the Gehrman-Stirling parametrization [39].

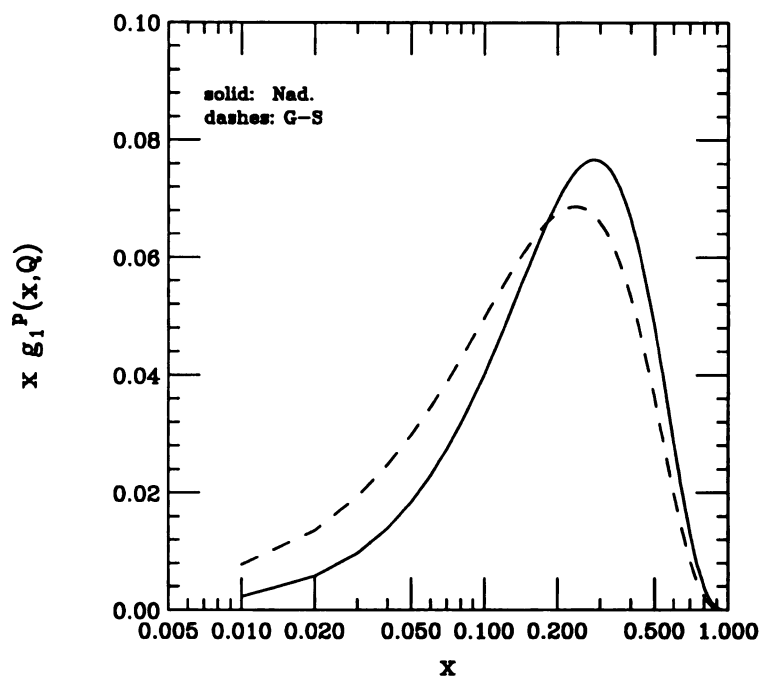


Figure 4.2: The function  $xg_1^P(x, Q)$ , which has been measured experimentally in polarized deep-inelastic lepton scattering, calculated using two sets of polarized parton distribution functions. The solid curve is the Nadolsky parametrization [38] and the dashed curve is the Gehrman-Stirling parametrization [39].

where the notation is as follows: The parton cross-section  $\hat{\sigma}_{LR}(p_1, p_2)$  is for the process  $u_L(p_1) + \bar{d}_R(p_2) \rightarrow W^+ \rightarrow e^+ + \nu_e$ ; note that  $u$  must be left-handed and  $\bar{d}$  right-handed because of the V-A coupling. The upper sign on  $u_{\pm}(x)$  and  $\bar{d}_{\mp}(x)$  is for  $\lambda = L$  and the lower sign is for  $\lambda = R$ . The first line in Eq. (4.2) corresponds to  $u, \bar{d}$  coming from  $p, \bar{p}$ , and the second line corresponds to  $\bar{d}, u$  coming from  $p, \bar{p}$ , respectively.  $x$  and  $x'$  are the parton momentum fractions in the proton and antiproton respectively. The parton distribution functions are, for example,

$$\begin{aligned} u_{\pm}(x) &= u \text{ quark with same/opposite helicity as } p \\ d(x') &= \bar{d} \text{ quark in unpolarized } \bar{p} \\ \bar{d}_{\mp}(x) &= \bar{d} \text{ quark with opposite/same helicity as } p \\ \bar{u}(x') &= u \text{ quark in unpolarized } \bar{p}. \end{aligned}$$

(We evaluate the parton distribution functions at momentum scale  $Q = 80$  GeV for  $W^{\pm}$  production.) The factor of  $1/2$  is from the average over  $\bar{p}$  helicities. We also add the contribution for the parton process  $c + \bar{s} \rightarrow W^+ \rightarrow e^+ + \nu_e$ . (We ignore Cabibbo-Kobayashi-Maskawa mixing in this work.) The cross-section for  $p_{\lambda} + \bar{p} \rightarrow W^- \rightarrow e^- + \bar{\nu}_e$  is given by a similar expression, but with parton densities  $d_{\pm}(x)u(x')$  and  $\bar{u}_{\mp}(x)\bar{d}(x')$ .

We have calculated  $\sigma(\lambda)$  from Eq. (4.2) by a Monte Carlo calculation based on the program PAPAGENO [32], modified to include the two sets of polarized parton distribution functions.

As a preliminary calculation, in this Section we consider the processes  $p_{\lambda} + \bar{p} \rightarrow W^{\pm}$  treating  $W^{\pm}$  as a stable particle. Figure 4.3 shows the Feynman diagram for the hard production process to produce a  $W^+$ . (In Section 4.3 we include the  $W^{\pm}$  decay.) Integrating the squared amplitude over the  $W$  phase-space yields the

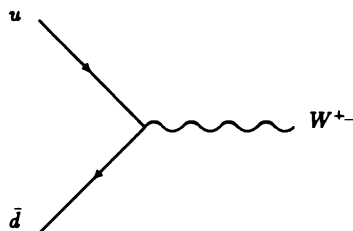


Figure 4.3: Diagram for  $u\bar{d} \rightarrow W^+$

color-averaged parton-level cross-section, summed over  $W$  polarizations:

$$\hat{\sigma}_{LR}(x, x') = \frac{\pi g^2}{3} \delta(xx's - M_W^2). \quad (4.3)$$

The  $\delta$ -function sets the invariant mass of the incoming partons equal to the invariant mass of the  $W$ .

In this case the cross-section  $\sigma(\lambda)$  may be calculated analytically, *i.e.*, without a Monte Carlo program, by inserting this  $\hat{\sigma}_{LR}$ — which treats the  $W^\pm$  as a stable particle of mass  $M_W$ —into Eq. (4.2), instead of the hard cross-section which includes the  $W$  decay. To find the differential cross-section in rapidity, include in Eq. (4.2) a factor

$$\delta\left(y_W - \frac{1}{2} \ln \frac{E_W + P_{zW}}{E_W - P_{zW}}\right),$$

which by going to the  $p\bar{p}$  center-of-momentum frame can be shown to be equal to

$$\delta\left(y_W - \frac{1}{2} \ln \frac{x}{x'}\right).$$

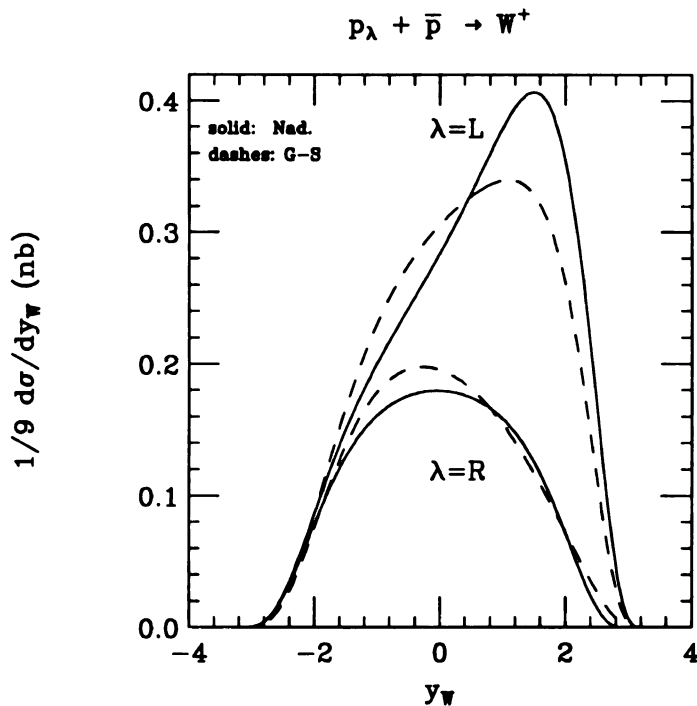


Figure 4.4: Cross-sections  $d\sigma(\lambda)/dy_W$  for  $p_\lambda + \bar{p} \rightarrow W^+$  in nb, multiplied by 1/9, the branching ratio for the  $W^+$  to decay to  $e^+ + \nu_e$ . Proton polarization  $\lambda$  is  $L$  or  $R$ . The solid and dashed curves are for pdf's from Ref. [38] and Ref. [39], respectively.

This  $\delta$ -function, together with the  $\delta$ -function from Eq. (4.3), relates the rapidity  $y_W$  of the  $W^\pm$  to the parton momentum fractions  $x$  and  $x'$ :

$$x = \frac{M_W}{\sqrt{s}} e^{y_W}, \quad x' = \frac{M_W}{\sqrt{s}} e^{-y_W}; \quad (4.4)$$

and yields the differential cross-section

$$\frac{d\sigma(\lambda)}{dy_W} = \frac{\pi g^2}{6s} \left[ u_\pm(x) d(x') + \bar{d}_\mp(x) \bar{u}(x') \right]. \quad (4.5)$$

For  $W^-$  production interchange  $u$  and  $d$ . The result is shown in Figures 4.4 and 4.5. Figure 4.4, which is for  $W^+$  production, has graphs of  $\frac{1}{9} d\sigma/dy_W$  vs  $y_W$ , where  $y_W$  is the rapidity of the  $W^+$ . Figure 4.5 is the same for  $W^-$  production. The cross-sections have been plotted in Figs. 4.4 and 4.5 multiplied by 1/9, which is the branching ratio for  $W^\pm$  to decay to  $e^\pm + \nu_e^{(\pm)}$ , because in an experiment the  $W^\pm$  would be observed from its decay to leptons.

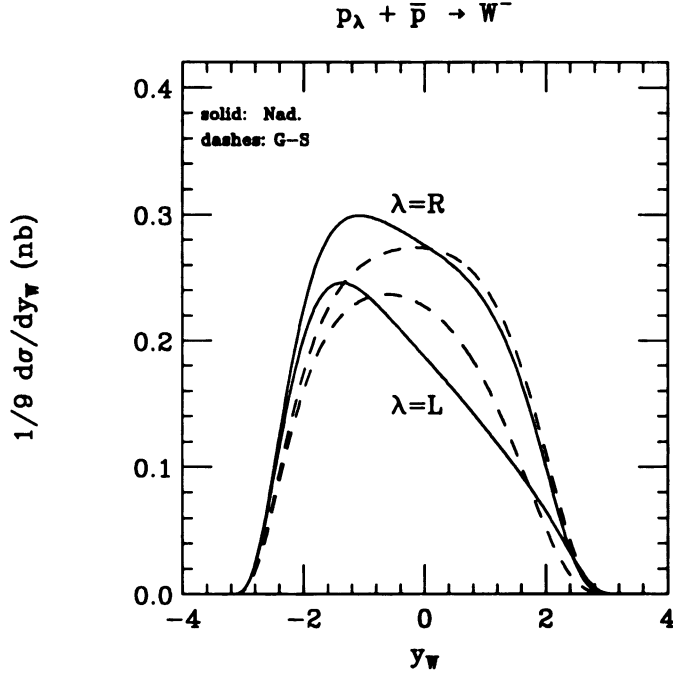


Figure 4.5: Cross-sections  $d\sigma(\lambda)/dy_W$  for  $p_\lambda + \bar{p} \rightarrow W^-$  in nb, multiplied by 1/9, the branching ratio for the  $W^-$  to decay to  $e^- + \bar{\nu}_e$ . Proton polarization  $\lambda$  is  $L$  or  $R$ . The solid and dashed curves are for ppdf's from Ref. [38] and Ref. [39], respectively.

The cross-section for  $p_L + \bar{p} \rightarrow W^+$  is greater than that for  $p_R + \bar{p} \rightarrow W^+$ , because  $W^+$  production is dominated by the reaction of  $u_L$  from the  $p$  and  $\bar{d}_R$  from the  $\bar{p}$ . Since  $\Delta u(x)$  is positive, as we see from Fig. 4.1,  $u_L$  has greater density in  $p_L$  than in  $p_R$ , making the cross-section larger for  $p_L$ . Similarly,  $\sigma(p_R + \bar{p} \rightarrow W^-)$  is greater than  $\sigma(p_L + \bar{p} \rightarrow W^-)$  because  $W^-$  production is dominated by  $d_L$  from the  $p$ . Figure 4.1 shows that  $\Delta d(x)$  is negative, so  $d_L$  has greater density in  $p_R$  than in  $p_L$ .

We can display the spin dependence by plotting the left-right polarization asymmetry  $\mathcal{A}_{LR}(W)$ , defined by

$$\mathcal{A}_{LR}(W) = \frac{d\sigma(L)/dy_W - d\sigma(R)/dy_W}{d\sigma(L)/dy_W + d\sigma(R)/dy_W}. \quad (4.6)$$

For  $W^+$  production Eq. (4.6) shows that  $\mathcal{A}_{LR}(W)$  is simply related to  $\Delta u(x)$  and

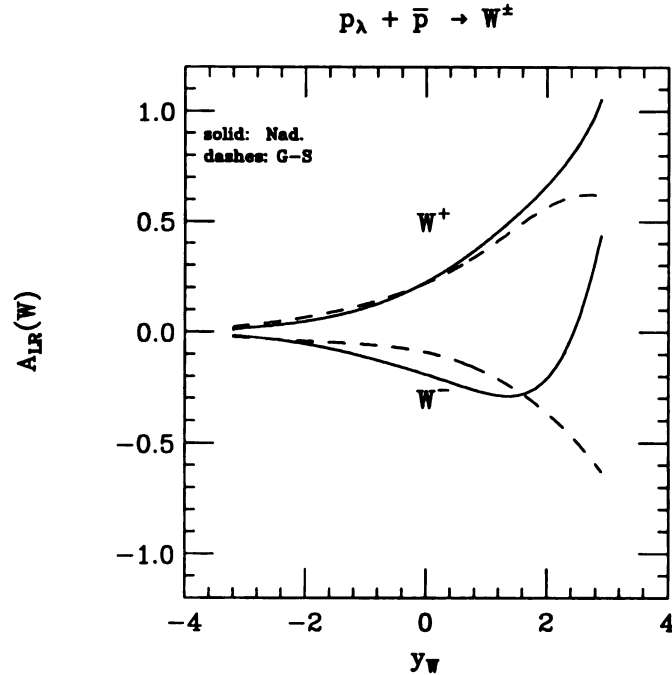


Figure 4.6: The left-right polarization asymmetry  $\mathcal{A}_{LR}$  for  $W^\pm$  production in polarized  $p - \bar{p}$  collisions. The solid and dashed curves are for ppdf's from Ref. [38] and Ref. [39], respectively.

$\Delta\bar{d}(x)$ ; we have

$$\mathcal{A}_{LR}(W) = \frac{\Delta u(x)d(x') - \Delta\bar{d}(x)\bar{u}(x')}{u(x)d(x') + \bar{d}(x)\bar{u}(x')} . \quad (4.7)$$

The polarization dependence of the sea quarks is small, so  $\mathcal{A}_{LR}(W)$  is approximately  $\Delta u(x)/u(x)$ . Similarly, for  $W^-$  production  $\mathcal{A}_{LR}(W)$  is approximately  $\Delta d(x)/d(x)$ .

The left-right polarization asymmetry  $\mathcal{A}_{LR}(W)$  is shown in Figure 4.6, as a function of  $y_W$ , for both  $W^+$  and  $W^-$  production. The asymmetry is greatest for  $y_W > 0$ , *i.e.*, at large  $x$ , where the asymmetry may be as large as 50 percent. For  $y_W < 0$ , the asymmetry is small because  $y_W < 0$  corresponds to small  $x$ , where  $\Delta f(x)$  is small. This result is in accord with the intuition that the helicity of partons with small  $x$  is not much correlated with proton helicity.

In the case of  $W^+$  production the two sets of ppdf's give fairly similar results for  $\mathcal{A}_{LR}(W)$ . The  $W^+$  asymmetry depends on  $\Delta u(x)$ , which is relatively well determined by deep-inelastic polarized lepton scattering. In the case of  $W^-$  production

the two sets of ppdf's give dissimilar results for  $\mathcal{A}_{LR}(W)$ . The  $W^-$  asymmetry depends on  $\Delta d(x)$ , which is less well determined by measurement of  $g_1^p(x, Q)$  because  $\Delta q(x)$  is weighted by  $e_q^2$  which is 1/9 for  $d$  compared to 4/9 for  $u$ . Thus the process  $p + \bar{p} \rightarrow W^-$  would be the most likely to give accurate new information on the ppdf's, specifically on  $\Delta d(x)$ , as has been pointed out by Nadolsky [40].

A significant difference between the two sets of ppdf's occurs at very large  $y_W$ , say  $y_W > 2$ , which corresponds to the limit  $x \rightarrow 1$  by Eq. (4.4). The two parametrizations of ppdf's treat the limit  $x \rightarrow 1$  differently. Nadolsky [38] imposed the requirement that  $u_-(x) \rightarrow 0$  and  $d_-(x) \rightarrow 0$  as  $x \rightarrow 1$ ; equivalently,  $\Delta u(x) \rightarrow u(x)$  and  $\Delta d(x) \rightarrow d(x)$ . This requirement, first derived in Ref. [41] by an argument based on first-order perturbation theory, means that if a parton carries all the momentum of the proton ( $x = 1$ ) then it has the same helicity as the proton. With this requirement the asymmetry  $\mathcal{A}_{LR}(W)$  must approach +1 as  $x \rightarrow 1$ , *i.e.*, as  $y_W$  approaches its maximum value. ( $\Delta \bar{d}(x)$  and  $\bar{d}(x)$  are negligible at  $x = 1$ .) Indeed  $\mathcal{A}_{LR}(W)$  for the Nadolsky ppdf's is increasing toward 1 as  $y_W$  increases. Testing experimentally this interesting helicity behavior at large  $x$  is emphasized in Ref. [40]. Gehrmann and Stirling [39] did not impose the requirement  $\Delta f(x) \rightarrow f(x)$  as  $x \rightarrow 1$ , but rather fitted  $\Delta u(x)$  and  $\Delta d(x)$  only in the limited range of  $x$  where data exists on  $g_1^p(x, Q)$ , extending out to  $x \approx 0.6$ ; therefore their ppdf's should only be applied for  $y_W < 2.7$ . Of course, we exaggerate the difference between  $\sigma(L)$  and  $\sigma(R)$  at very large  $y_W$  by plotting the left-right asymmetry  $\mathcal{A}_{LR}(W)$ , which is a ratio; both  $d\sigma(L)/dy_W$  and  $d\sigma(R)/dy_W$  approach 0 for large  $y_W$ , so  $\mathcal{A}_{LR}(W)$  is a ratio of very small cross-sections there. In any case we are interested in determining the ppdf's for all  $x$ , not just in the limit  $x \rightarrow 1$ .

The results shown in Figs. 4.4 - 4.6 give a good indication of the effect of proton polarization, but are not directly measurable because the  $W^\pm$  is unstable.

### 4.3 Decay of $W^\pm$

Next we include the leptonic decay of the  $W^\pm$  to consider the processes  $p_\lambda + \bar{p} \rightarrow (W^\pm \rightarrow e^\pm + \bar{\nu}_e) + X$ . It is this process that would actually be observed in an experiment. Of course only the  $e^\pm$  would be detected. The question addressed here is whether the  $W^\pm$  decay would markedly reduce the sensitivity of the polarization asymmetry  $\mathcal{A}_{LR}$  to the ppdf's.

Figure 4.8 shows  $d\sigma(\lambda)/dy_e$  for the process  $p_\lambda + \bar{p} \rightarrow (W^+ \rightarrow e^+ + \nu_e) + X$ , and Figure 4.9 shows the same for the process  $p_\lambda + \bar{p} \rightarrow (W^- \rightarrow e^- + \bar{\nu}_e) + X$ , where  $y_e$  is the rapidity of the  $e^\pm$ . These cross-sections were calculated by a Monte Carlo calculation from the tree-level formula.

We note that the distributions of  $y_e$  are spread out and shifted relative to the distributions of  $y_W$ ; the shift is toward negative rapidity in the case of  $e^+$  and  $W^+$ , and toward positive rapidity in the case of  $e^-$  and  $W^-$ . These shifts can be understood as a consequence of the V–A coupling between  $W^\pm$  and  $e^\pm \bar{\nu}_e$ , together with angular momentum conservation. Consider, for example,  $p_L \bar{p} \rightarrow W^+$ . The partons involved must be a left-handed  $u$  colliding with a right-handed  $\bar{d}$ , as shown schematically in Figure 4.7. Because a  $u_L$  in a  $p_L$  tends to have relatively large  $x$  (see Fig. 4.1) compared to the  $\bar{d}_R$  from the  $\bar{p}$ , the  $W^+$  comes out preferentially in the direction of the  $u_L$  (see Fig. 4.4), which is the case depicted in Figure 4.7. Angular momentum conservation—conservation of the double-arrow directions in Figure 4.7—along with the requirement that the  $e^+$  be right-handed, by the V–A coupling, force the positron direction to be against the  $W^+$  direction. In the lab frame this corresponds to a negative shift in rapidity, because a Lorentz boost from the  $W^+$  rest frame to the lab frame simply adds the  $W^+$  rapidity (zero in its rest frame) to the positron rapidity.

Figure 4.10 shows the left-right polarization asymmetry  $\mathcal{A}_{LR}(e)$  for both  $e^+$  and

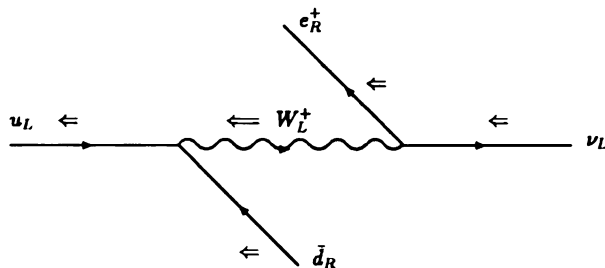


Figure 4.7: Schematic diagram of particle momentum and spin orientations in  $u_L \bar{d}_R \rightarrow W_L^+ \rightarrow e_R^+ \nu_L$ . Single arrows indicate momentum directions; double arrows indicate spin orientation. For clarity the  $\bar{d}$  and  $e^+$  momenta are shown at angles to the other particles', but they should be imagined as along the same line.

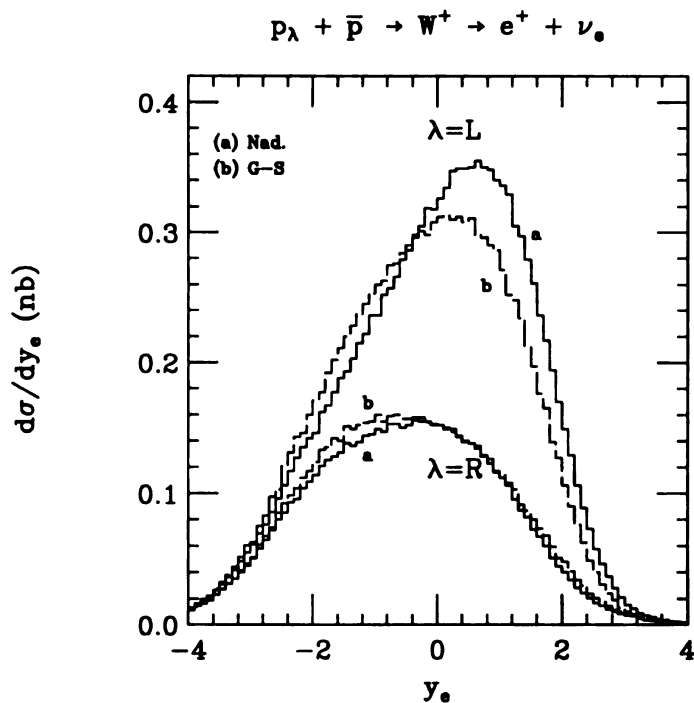


Figure 4.8: Cross-sections  $d\sigma(\lambda)/dy_e$  for  $p_\lambda + \bar{p} \rightarrow W^+ \rightarrow e^+ + \nu_e$  in nb, with proton polarization  $\lambda = L$  or  $R$ . The solid and dashed curves, labeled (a) and (b), are for ppdf's from Ref. [38] and Ref. [39], respectively.

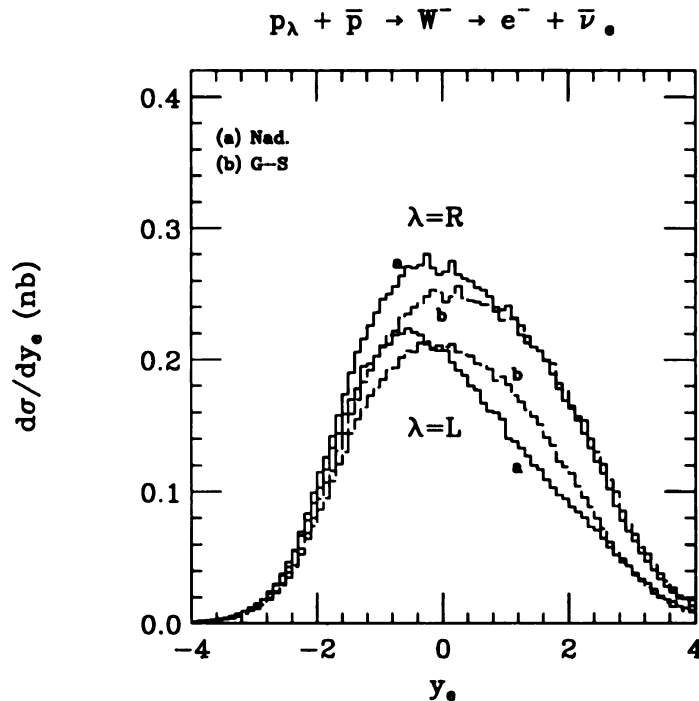


Figure 4.9: Cross-sections  $d\sigma(\lambda)/dy_e$  for  $p_\lambda + \bar{p} \rightarrow W^- \rightarrow e^- + \bar{\nu}_e$  in nb, with proton polarization  $\lambda = L$  or  $R$ . The solid and dashed curves labeled (a) and (b), are for ppdf's from Ref. [38] and Ref. [39], respectively.

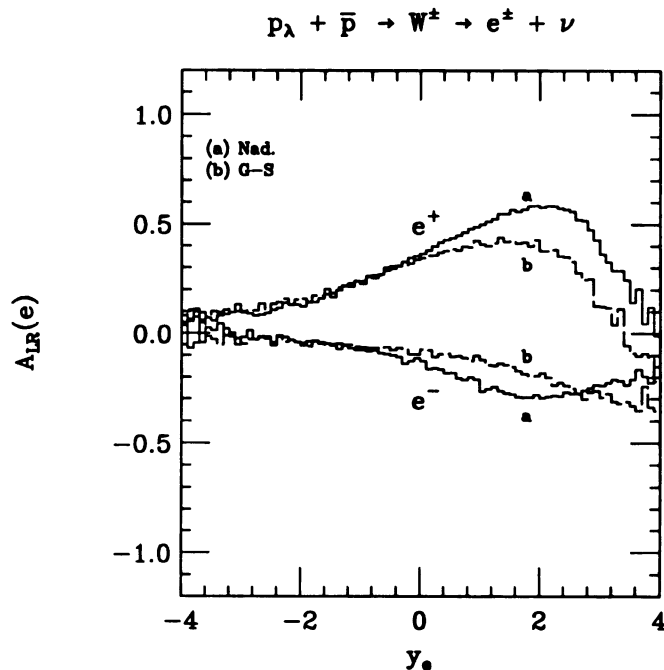


Figure 4.10: The left-right polarization asymmetry  $\mathcal{A}_{LR}(e)$  for  $W^\pm$  production in polarized  $p - \bar{p}$  collisions, with decay  $W^\pm \rightarrow e^\pm + \bar{\nu}_e$ . The solid and dashed curves, labeled (a) and (b), are for ppdf's from Ref. [38] and Ref. [39], respectively.

$e^-$  production,

$$\mathcal{A}_{LR}(e) = \frac{d\sigma(L)/dy_e - d\sigma(R)/dy_e}{d\sigma(L)/dy_e + d\sigma(R)/dy_e}. \quad (4.8)$$

As before,  $\mathcal{A}_{LR}(e)$  depends mainly on  $\Delta u(x)$  for  $e^+$ , and on  $\Delta d(x)$  for  $e^-$ . However,  $x$  is not simply related to  $y_e$ . Therefore a real experiment, where only  $y_e$  can be measured, would not determine  $\Delta u(x)$  or  $\Delta d(x)$  directly; there is no direct relation analogous to Eq. (4.7) for  $\mathcal{A}_{LR}(e)$ . Instead, a calculation of  $d\sigma(\lambda)/dy_e$ , computed from parametrized ppdf's, would be fitted to the data. The asymmetry for  $e^\pm$  production is somewhat less than the asymmetry found in Section 4.2 for  $W^\pm$  production, but is still significant. We will quantify this statement below by estimating the luminosity which would be required to distinguish the two ppdf's.

In an experiment, the charged leptons would be observed as a function of their transverse momentum  $p_{T_e}$ . It is interesting to consider events with large  $p_{T_e}$ . Therefore we plot in Figures 4.11 and 4.12 the cross-sections for  $W^+$  and  $W^-$  production,

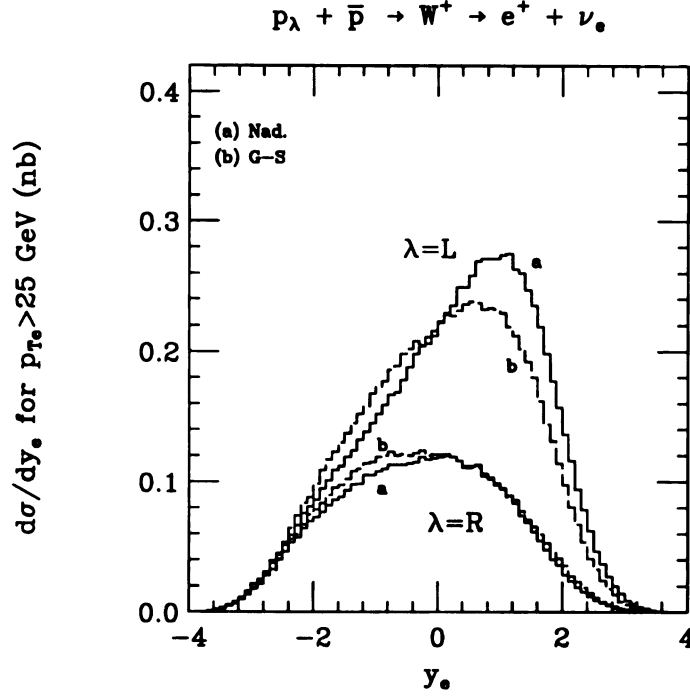


Figure 4.11: Cross-sections  $d\sigma(\lambda)/dy_e$  for  $p_\lambda + \bar{p} \rightarrow W^+ \rightarrow e^+ + \nu_e$  in nb, with a kinematic cut on the lepton transverse momentum,  $p_{Te} > 25$  GeV. The solid and dashed curves, labeled (a) and (b), are for ppdf's from Ref. [38] and Ref. [39], respectively.

with decay  $W^\pm \rightarrow e^\pm + \bar{\nu}_e$ , for events with  $p_{Te} > 25$  GeV; Figure 4.13 shows the corresponding polarization asymmetry. With this high- $p_{Te}$  cut there is again a significant asymmetry.

The left-right polarization asymmetry of  $d\sigma(\lambda)/dy_e$  with  $p_{Te} > 25$  GeV exhibits large differences between the two sets of ppdf's that we have used in our calculations, which implies that this process is sensitive to the ppdf's. The region of large rapidity is especially interesting. Indeed,  $\mathcal{A}_{LR}(e)$  with  $p_{Te} > 25$  GeV resembles  $\mathcal{A}_{LR}(W)$  of the underlying  $W^\pm$  production, for large rapidity. Specifically, for the Nadolsky ppdf's [38]  $\mathcal{A}_{LR}(e)$  increases at large  $y_e$ , which reflects the increase of  $\mathcal{A}_{LR}(W)$  at large  $y_W$ . Events with large  $y_W$  are interesting because they come from partons with large  $x$  in the proton, and we would like to verify the helicity behavior of partons at large  $x$ , that is, that  $f_-(x) \rightarrow 0$  as  $x \rightarrow 1$ . However there is an experimental

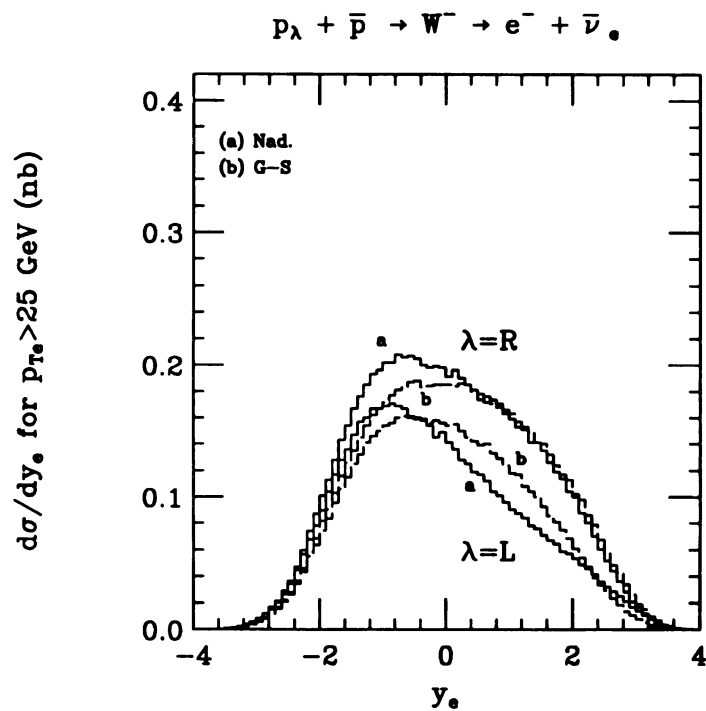


Figure 4.12: Cross-sections  $d\sigma(\lambda)/dy_e$  for  $p_\lambda + \bar{p} \rightarrow W^- \rightarrow e^- + \bar{\nu}_e$  in nb, with a kinematic cut on the lepton transverse momentum,  $p_{T_e} > 25$  GeV. The solid and dashed curves labeled (a) and (b), are for ppdf's from Ref. [38] and Ref. [39], respectively.

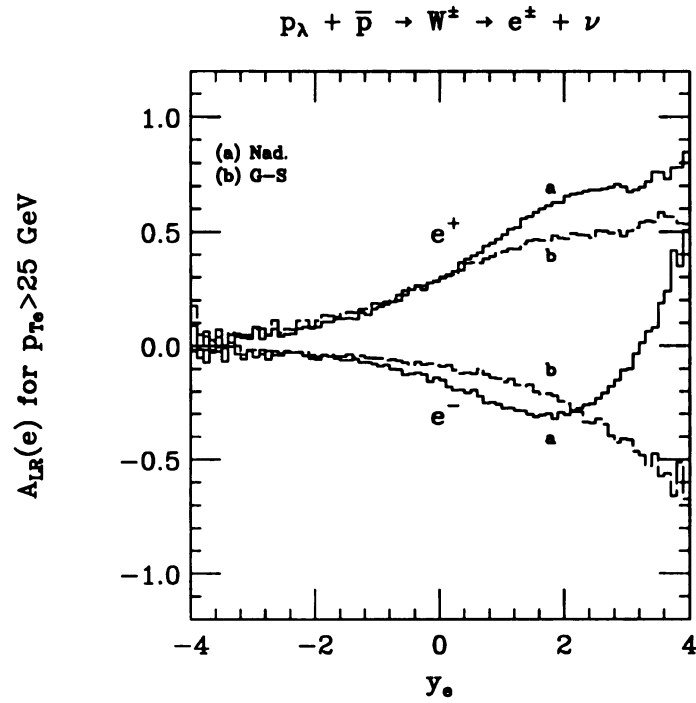


Figure 4.13: The left-right polarization asymmetry  $\mathcal{A}_{LR}(e)$  for  $W^\pm$  production in polarized  $p - \bar{p}$  collisions, with decay  $W^\pm \rightarrow e^\pm + \bar{\nu}_e^{(-)}$ , with a kinematic cut on the lepton transverse momentum,  $p_{Te} > 25$  GeV. The solid and dashed curves, labeled (a) and (b), are for pdf's from Ref. [38] and Ref. [39], respectively.

difficulty here: It is difficult for a collider detector to detect charged leptons well with  $y_e > 2.5$ , and the range of  $y_e$  where  $\mathcal{A}_{LR}(e)$  increases strongly with  $y_e$  is in the range of  $y_e > 2.5$ . Thus we find that a precise test of the helicity behavior of partons at large  $x$  would require a detector with large coverage in rapidity, extending to  $y_e > 2.5$ . This result shows the importance of the  $W^\pm$  decay. In terms of the  $W^\pm$ , the large- $x$  helicity behavior is already tested to some degree at  $y_W < 2.5$ ; but in terms of the  $e^\pm$ , the large- $x$  helicity behavior is not really tested until  $y_e > 2.5$ .

Finally, we estimate the integrated luminosity ( $\int \mathcal{L}$ ) that would be needed to measure the ppdf's accurately. Over a large range of  $y_e$  with  $y_e > 0$ , the asymmetry  $\mathcal{A}_{LR}(e)$  is of order 0.3, and the *difference* between the two sets of ppdf's, which we are using to gauge the current uncertainty of the ppdf's, is of order 0.1, *i.e.*, about 30 percent of the asymmetry. An experiment to distinguish between the two sets of ppdf's, and thus provide a more accurate measurement of the ppdf's than deep-inelastic scattering, would need to measure the polarized cross-sections to an accuracy of order 1 percent. The total polarized cross-sections, with and without the  $p_{Te}$  cut, are listed in Table 4.3. (There is no kinematic cut on the rapidity  $y_e$  for the cross-sections in Table 4.3; the reduction of  $\sigma(\lambda)$  for an experimentally accessible range of  $y_e$ , say  $|y_e| < 2.5$ , can be judged from Figs. 4.8, 4.9 and 4.11, 4.12.) By Poisson statistics, a measurement of the cross-section to an accuracy of 1 percent would require  $\delta\sigma/\sigma = 1/\sqrt{N} = 0.01$ , which implies a number of events  $N$  of order  $10^4$  events. For the cross-sections in Table 4.3, which are of order 1 nb, the required  $\int \mathcal{L}$  is of order  $10 \text{ pb}^{-1}$ . But those are total cross-sections. Larger integrated luminosity would be needed to measure *differential* cross-sections to 1 percent accuracy. To have  $10^4$  events in a rapidity bin  $\Delta y$  requires  $\int \mathcal{L} = 10^4 (d\sigma/dy \cdot \Delta y)^{-1}$ , which is of order  $100 \text{ pb}^{-1}/\Delta y$ . To measure the polarization asymmetry would require this large  $\int \mathcal{L}$  for each proton polarization ( $L$  and  $R$ ). These are only

Table 4.1: Total cross-sections for the processes  $p_\lambda + \bar{p} \rightarrow W^\pm \rightarrow e^\pm + \bar{\nu}_e^{(-)}$ , where  $\lambda$  is the proton polarization,  $L$  or  $R$ . The polarized parton distribution functions are taken from Refs. [38] and [39]. Also, we consider a transverse momentum cut  $p_{Te} > p_{Tmin}$ . There is no restriction on lepton rapidity  $y_e$ ; the effect of a cut on  $y_e$  may be judged from Figs. 4.8, 4.9, 4.11, 4.12.

charge	$\lambda$	$p_{Tmin}$	$\sigma(\lambda)(nb)$	ppdf
$W^+$	$L$	0	1.298	Ref. [38]
			1.211	Ref. [39]
$W^+$	$R$	0	0.638	[38]
			0.668	[39]
$W^-$	$L$	0	0.817	[38]
			0.829	[39]
$W^-$	$R$	0	1.117	[38]
			1.048	[39]
$W^+$	$L$	25 (GeV)	0.901	[38]
			0.841	[39]
$W^+$	$R$	25 (GeV)	0.442	[38]
			0.464	[39]
$W^-$	$L$	25 (GeV)	0.566	[38]
			0.576	[39]
$W^-$	$R$	25 (GeV)	0.775	[38]
			0.728	[39]

order of magnitude estimates, but they demonstrate that high luminosity, *e.g.*,  $\int \mathcal{L}$  as large as  $1 \text{ fb}^{-1}$ , would be necessary to measure the ppdf's at an interesting level of accuracy. For regions of  $y_e$  and  $p_{Te}$  where the cross-section is very small, such as the region of large  $y_e$ , the required integrated luminosity would be correspondingly larger.

## 4.4 Conclusions

We have calculated the cross-sections for  $W^\pm$  production, with subsequent decay to  $e^\pm \bar{\nu}_e^{(-)}$ , in polarized proton – unpolarized antiproton collisions at center-of-mass energy 2 TeV. The left-right polarization asymmetry is sensitive to the spin-dependent parton distributions  $\Delta u(x)$  in the case of  $W^+$ , and  $\Delta d(x)$  in the case of  $W^-$ . We

used two recently published parametrizations of polarized parton distribution functions to gauge the current uncertainty of  $\Delta u(x)$  and  $\Delta d(x)$ , as measured from deep-inelastic scattering.  $W^\pm$  production can provide a second method of measuring these important distributions.

The accurate determination of the ppdf's would be a necessary step in a program to use polarized proton scattering as a probe of interesting new physics. If a polarized proton beam were available at the Tevatron collider, the  $W^\pm$  production processes would be used to obtain new data on ppdf's. We find that with large luminosity, *i.e.*,  $\int \mathcal{L}$  of order  $1 \text{ fb}^{-1}$  for each proton polarization, the functions  $\Delta u(x)$  and  $\Delta d(x)$  can be measured to a few percent accuracy over a large range of  $x$ . The interesting large- $x$  region can be well measured only if the rapidity coverage of the detector extends to quite large  $y_e$ , at least beyond  $y_e = 2.5$ .

Experimental studies of spin physics and the ppdf's will soon be possible at the BNL Relativistic Heavy Ion Collider (RHIC). A recent preprint [42] examines the potential of various processes, including single  $W$  production, for constraining the ppdf's. Reference [43] focuses on  $W$  and  $Z^0$  production at RHIC, while other processes at RHIC are discussed in References [44, 45].

## **Part II**

# **A Light Gravitino and the Supersymmetry Breaking Mechanism**

# Chapter 5

## Detecting a Light Gravitino at a Future Linear Collider

### 5.1 Introduction to Supersymmetry

*A too rapid unification, and an excessive appliance to parts and particulars, are the twin dangers of speculation.*

—Ralph Waldo Emerson

Many physicists tacitly live according to a faith that the fundamental interactions, indeed all Natural phenomena, will eventually allow some *unified* description. Even if this is a mystical delusion, at very high energies, such as presumably were common in the early universe, quantum gravity effects are important—but are neglected in the Standard Model (SM). In this context, a puzzling feature of the SM becomes apparent. The natural scale of gravity is the Planck mass  $M_P = \frac{1}{\sqrt{G_{Newton}}} \approx 10^{19}$  GeV, while the scale of the electroweak interactions is about 100 GeV. The tiny ratio between these scales ( $10^{-17}$ ) is unexplained at present. This mystery is called the “hierarchy problem.”

Moreover, even should we accept this hierarchy as an *a priori* constraint, loop corrections to SM masses will include Planck-scale fields. To end up with physical masses of order 100 GeV, we would therefore have to multiply each such loop by a

constant of order  $10^{-17}$ . Unless such miniscule constants are explained at a deeper level we feel that this is a “naturalness” problem. This “fine-tuning” will have to be repeated at each order of perturbation theory.

Supersymmetry (SUSY) is a symmetry which solves the fine-tuning problem. That is, if we define a SUSY theory with a hierarchy of mass scales, the hierarchy will not be spoiled by loop corrections. In terms of Feynman diagrams, this is because every boson loop will be cancelled by a matching fermion loop including a factor of  $-1$ , according to the usual Feynman rule for fermion loops. This cancellation, which preserves a hierarchy against higher-order corrections, is the practical motivation for SUSY.

But SUSY is also aesthetically attractive, because the symmetry relates fermions to bosons, the two fundamental classes of field in relativistic quantum field theory. From the point of view which asks for unification, nothing could be more natural. In order to accomplish this relation between bosons and fermions, it turns out that one must involve the generators of the Poincaré group. Specifically, the generators of SUSY are fermionic operators  $Q$  and  $\bar{Q}$  which obey the anti-commutative algebra:

$$\{\bar{Q}_\alpha, Q_\beta\} = 2P^\mu(\gamma_\mu)_{\alpha\beta}, \quad (5.1)$$

where  $P^\mu$  is the four-momentum operator, and  $\alpha$  and  $\beta$  are spinor indices. It is satisfying that the generators of SUSY and of space-time translations are woven together inevitably.

This connection with the Poincaré group is a clue to another attractive feature of SUSY. In addition to Eq. (5.1), the SUSY generator also commutes with the generator of space-time translations:

$$[Q_\alpha, P^\mu] = 0.$$

That is, SUSY is a global symmetry, independent of space-time coordinates. SUSY can be made local, or gauged. The resulting theory includes a spin-2 field and

its spin-3/2 partner, identifiable as the graviton and the gravitino. In other words, local SUSY is a (non-renormalizable) theory of quantum gravity, called supergravity (SUGRA). Part II of this thesis deals with the phenomenology of a light (order keV) gravitino.

This symmetry between bosons and fermions implies that every fermion has a bosonic partner with the same SM quantum numbers. Reflection on the SM particles reveals that none of them can be SUSY partners of each other. For example, the neutrino cannot be the fermionic partner of the photon, because the neutrino transforms differently under  $SU(2)_L$ . Therefore if SUSY actually is a symmetry of nature, the SUSY partners (“sparticles”) have not been observed. The hypothetical sparticles are named according to their SM partners. The scalar partners of fermions are known as “sfermions,” whose names are derived by adding an “s” prefix to the name of their SM partner to get “squarks” and “sleptons.” The fermionic partners of the bosons are named with an “ino” suffix: the “gauginos” are “gluinos,” “winos,” “zinos,” “photinos,” and “Higgsinos.” However, the mass eigenstates of the fermionic sparticles need not be the same linear combination of unbroken SM fields as the SM gauge bosons. That is, in general we must consider “neutralinos” and “charginos,” not specific combinations like the photino. Sparticles are denoted by a tilde over their SM counterpart. For example,  $\tilde{W}$  is the wino field.

Only a few of these new fields will enter into our calculation in this chapter. We will be interested in the production of gravitinos, the fermionic partner of the graviton in SUGRA. The diagrams for the production of gravitinos from  $e^+e^-$  annihilation involve an exchange of the scalar partner to the electron field, called the selectron. Because right-handed and left-handed electrons are independent fields, they each have a scalar partner. These are named the right and left selectrons although, again, they are scalars. The exchange of a selectron produces neutralinos

which will decay to gravitinos if the gravitino is light enough. The neutralino field is an unknown combination of the neutral gauginos and Higgsinos.

The SM fields are conveniently distinguished from their superpartners by introducing a global symmetry called R-parity. The SM fields are R-even, while their superpartners are R-odd. If R-parity is assumed to be conserved, then lepton and baryon number are conserved <sup>†</sup>, and R-odd particles can only be produced in pairs [47]. We assume R-parity conservation throughout this work.

### 5.1.1 Supersymmetry Breaking

If supersymmetry is unbroken, then particles must be degenerate in mass with their superpartners. As we noted above, no superpartners have been observed. Therefore, in our low-energy world, SUSY must be broken to be a viable theory of particles. As long as the breaking mechanism does not generate any new quadratic divergences, which will contaminate weak-scale physics with Planck-scale masses, then our theory will still stabilize the hierarchy as we wish. Such SUSY breaking is called “soft”; and the (relatively few) Lagrangian terms which satisfy this constraint are called “soft SUSY-breaking terms.” These may be determined experimentally, but ultimately we would like to explain their origin. In fact, Haber said recently [48], “The origin of supersymmetry breaking is perhaps the most pressing theoretical problem in fundamental theories of supersymmetry.”

We noted above that SUSY solves the fine-tuning problem by stabilizing the hierarchy of mass scales against radiative corrections. It has been suggested that models of dynamically broken SUSY may explain the hierarchy itself [49]. It is also encouraging to note that in many supersymmetric models electroweak symmetry

---

<sup>†</sup>R-parity is imposed by hand in the minimal supersymmetric SM. Some theories, such as the minimal left-right symmetric SUSY SM, automatically guarantee R-parity conservation at the weak scale [46].

is broken dynamically by the renormalization group running of one of the Higgs masses [50].

Since the origin of SUSY breaking is an unsolved problem, the subject is still rather technical. Because we will be examining the phenomenology of a light gravitino, we will only consider models of SUSY breaking derived from more fundamental models of broken SUGRA. Here we will merely distinguish two broad classes of models. In both types of model one posits a “hidden” sector of heavy fields in addition to the SM “visible” sector. The hidden sector gauge symmetry is assumed to break itself dynamically, for example by instantons [49] or by condensation of a gaugino field [51]. This breaking is transmitted to the visible sector via some “messenger” interaction. The messenger interaction distinguishes our two classes of models. In older models, the visible and hidden sectors interact only gravitationally; these are “gravity-mediated” models of SUSY breaking. More recently [52], there has been a renewal of interest in “gauge-mediated” models of SUSY breaking, in which the breaking of the hidden sector symmetry is transmitted to the visible sector by some additional gauge interaction.

The gauge-mediated models discussed in Ref. [52] have been found to require a very small mass for the gravitino [52]. Therefore the existence of a light gravitino is a definite prediction of the whole class of gauge-mediated SUSY breaking models. Ruling out a light gravitino experimentally would mean ruling out the gauge-mediated SUSY breaking mechanism. Discovering a light gravitino, on the other hand, does *not* rule out all gravity-mediated models; for example, certain “no-scale” unified SUGRA models [53] allow a very light gravitino. Should a light gravitino be found, these models would have to be distinguished from each other by the mass spectrum of the remaining sparticles.

## 5.2 Introduction to the Problem at Hand

Recently, Dine, Nelson and Shirman [52] have revisited a class of models in which SUSY is dynamically broken at a low scale, within a few orders of magnitude of the weak scale. Certain technical problems with these models have been solved, so that they are more attractive as realistic fundamental theories. They noted that in such models the lightest supersymmetric partner (LSP) is the gravitino ( $\tilde{G}$ ) and the next to lightest supersymmetric partner (NLSP) is a neutralino  $\chi_1^0$ , which is a mixture of neutral gauginos and Higgsinos.<sup>†</sup> Ellis, Enqvist, and Nanopoulos had also noted as early as 1984 that “no-scale” models of dynamically broken SUGRA allow a very light gravitino [53]. These models may have a bearing on the cosmological constant problem and the strong CP problem,<sup>‡</sup> as well as dynamically creating a mass hierarchy. Motivated by these theoretical possibilities, we consider in this chapter the production of neutralinos and their subsequent decay into gravitinos. The decay channel of the neutralino which we focus on is the decay into a photon and a light gravitino.

In the gauge-mediated models the mass of the gravitino  $m_{3/2}$  is in the range  $1\text{ eV} < m_{3/2} < 10\text{ keV}$ . As in the spontaneously broken electroweak theory, where the  $W$  mass is proportional to the vacuum expectation value of the Higgs field and the weak coupling, so here the gravitino mass is related to the SUSY breaking scale and the gravitational coupling [47]. We define a mass parameter

$$M_{susy} = \sqrt{m_{3/2} M_{Planck}}, \quad (5.2)$$

where the Planck mass is  $M_{Planck} = 1/\sqrt{G_N} \sim 10^{19}\text{ GeV}$ . In the gauge-mediated models  $M_{susy}$  is in the range  $10^5 - 10^7\text{ GeV}$ . This mass parameter *may be* the scale of SUSY breaking, but in general we must only consider  $M_{susy}$  to be a parameter which

---

<sup>†</sup>In  $N=2$  supersymmetric models of this type it is likely that the NLSP will be the right slepton [54]. We do not treat this possibility here.

<sup>‡</sup>The strong CP problem is described for example in Kaku’s book [1].

determines the gravitino mass and its effective coupling strength. In particular, in the “no-scale” unified SUGRA models of Reference [53], SUSY may be broken by gaugino condensation at scales above  $10^7$  GeV, yet the gravitino can be even lighter than 1 eV.

In most other models of SUSY breaking, such as the minimal supersymmetric standard model (MSSM), the gravitino mass is of order the weak scale and the supersymmetry-breaking occurs at a scale in the range  $10^{10} - 10^{11}$  GeV. Usually, in the MSSM, the lightest supersymmetric partner is a neutralino, which is then stable assuming  $R$ -parity conservation. Thus the decay of the neutralino into a photon and a light gravitino probably signals “low-energy” SUSY breaking; in any case it narrows the field of possible breaking scenarios.

In this chapter we study the possibility of detecting a light gravitino from the decay of massive neutralinos (the NLSP, with mass  $m_{\chi_1^0}$ ) which are produced in pairs from  $e^-e^+$  annihilation at the Next Linear Collider (NLC, a proposed collider introduced in Chapter 2) with a right-hand polarized electron beam. (Use of a right-hand polarized beam is to suppress background contributions, as discussed in Section 5.3.4.) For this study, we assume that the center-of-mass energy  $\sqrt{S}$  of the NLC leptons is 500 GeV and the NLC luminosity is  $50 \text{ fb}^{-1}$  per year. Accordingly, we ignore the mass of the electron and the mass of the gravitino. The experimental signature of the signal event of interest is two photons with large missing energy. The missing energy belongs to the two gravitinos, which escape undetected, because their interactions are so weak. By calculating the cross section for this process as a function of  $M_{\text{susy}}$  and  $m_{\chi_1^0}$ , we will determine what region of this parameter space would be accessible at the NLC. The accessible parameter range for current electron (LEP/SLC) and hadron (Tevatron) colliders is also briefly discussed; detection of a light gravitino at these colliders is more thoroughly analysed in Refs. [55] and [53].

## 5.3 Detecting a Light Gravitino at the Next Linear Collider

### 5.3.1 Production of Neutralino Pairs at the NLC

A pair of neutralinos, the NLSP's, can be produced at the NLC via the tree-level process  $e^-e^+ \rightarrow \chi_1^0\chi_1^0$ . At tree level, the particle exchanged in the t- and u-channel Feynman diagrams are either left or right selectrons, and that of the s-channel diagram is the Z-boson. The t- and u-channel diagrams vanish if  $\chi_1^0$  is Higgsino-like because the Higgsino-electron-selectron coupling is zero for a massless electron. The s-channel diagram vanishes if  $\chi_1^0$  is gaugino-like because there is no tree-level  $Z\text{-}\tilde{B}\text{-}\tilde{B}$  or  $Z\text{-}\widetilde{W}^3\text{-}\widetilde{W}^3$  interaction, because the Z is a combination of  $W^3$  and  $B$ , which interact neither with each other nor themselves. ( $\tilde{B}$  is the supersymmetric partner of the  $U(1)_Y$  gauge boson  $B$ , and  $\widetilde{W}^3$  is the supersymmetric partner of the third component of the  $SU(2)_L$  gauge boson  $W^3$ .)

In general the neutralino is a mixture of the neutral gauginos ( $\tilde{B}$  and  $\widetilde{W}^3$ ) and neutral Higgsinos. Determining its gaugino and Higgsino components will be important for distinguishing different models of SUSY breaking. For example, in the constrained MSSM (CMSSM), which narrows the MSSM's parameter space with some cosmological and unification assumptions, the lightest neutralino  $\chi_1^0$  is most often primarily  $\tilde{B}$ , or "bino-like" (see [56] and [57]).

The NLC will provide a powerful tool for probing the content of the neutralino. Calculation of  $e^+e^-$  cross sections is simpler than for hadron collisions, and more than 90% polarization of the NLC electron beam is expected [19]. For simplicity, in this paper, we shall assume that the electron beam at the NLC can be 100% right-hand polarized. The assumption of 100% polarization will not significantly affect our

conclusions as compared to a 90% polarized beam, but the polarization capability will simplify calculation and eliminate a background. For a right-polarized electron beam, the  $\widetilde{W}^3$  component of the neutralino does not contribute to neutralino pair production in  $e_R^- e^+$  collisions because the  $\widetilde{W}^3$  coupling to fermions is pure left-handed, due to the  $SU(2)_L$  gauge symmetry. As for the bino component of the neutralino, recall that  $\widetilde{B}$  may be written as a linear combination of photino  $\widetilde{\gamma}$  and  $\widetilde{W}^3$ ; specifically,

$$\widetilde{B} = \widetilde{\gamma} / \cos \theta_w - \widetilde{W}^3 \tan \theta_w , \quad (5.3)$$

where  $\theta_w$  is the weak mixing angle ( $\sin^2 \theta_w = 0.23$ ). We decompose the bino this way so that we may compare the cross section for production of mass-eigenstate photinos to production of general neutralino mass-eigenstates. If  $\chi_1^0$  is photino-like, then the production of  $\chi_1^0 \chi_1^0$  from a right-hand polarized electron beam occurs only through the  $\widetilde{\gamma}$  component in Eq. (5.3). Similarly, for a general gaugino-like neutralino, only the mass-eigenstate component of the bino will contribute to  $\chi_1^0 \chi_1^0$  production, while the  $\widetilde{W}^3$  remainder will not contribute when the electron is right-polarized. For the rest of this thesis we assume that the neutralino  $\chi_1^0$  is gaugino-like. The case that  $\chi_1^0$  is Higgsino-like is discussed in the paper upon which this chapter is based [58].

For a gaugino-like neutralino we define a mixing angle  $\alpha$  by

$$\chi_1^0 = \widetilde{B} \cos \alpha + \widetilde{W}^3 \sin \alpha . \quad (5.4)$$

Then the cross section for  $\chi_1^0 \chi_1^0$  production from a right-handed electron is, by Eqs. (5.4) and (5.3),

$$\sigma(e_R^- e^+ \rightarrow \chi_1^0 \chi_1^0) = \sigma(e_R^- e^+ \rightarrow \widetilde{\gamma} \widetilde{\gamma}) \left( \frac{\cos \alpha}{\cos \theta_w} \right)^4 \quad (5.5)$$

in terms of the cross section for photino-pair production. In the numerical calculations below we always report results for  $\alpha = 0$ , corresponding to  $\chi_1^0$  being  $\widetilde{B}$ -like; it is straightforward to determine the numbers for other values of  $\alpha$ .

The cross section for  $e_R^- e^+ \rightarrow \tilde{\gamma} \tilde{\gamma}$  has been published [59, 60]. There are two Feynman diagrams remaining for this process after our assumption of a gaugino-like neutralino and a right-handed electron beam, representing the t-channel and u-channel exchange of a right selectron  $\tilde{e}_R$ . The differential cross section  $d\sigma/d\cos\theta$  for  $e_R^-(p_1) + e^+(p_2) \rightarrow \chi_1^0(p_3) + \chi_1^0(p_4)$ , where  $\theta$  is the angle of an outgoing neutralino  $\chi_1^0$  relative to the  $e^-$  direction, is

$$\frac{d\sigma}{d\cos\theta} = \frac{e^4}{16\pi S} \sqrt{1 - \frac{4m_{\chi_1^0}^2}{S}} \left\{ \left( \frac{t - m_{\chi_1^0}^2}{m_{e_R}^2 - t} \right)^2 + \left( \frac{u - m_{\chi_1^0}^2}{m_{e_R}^2 - u} \right)^2 - \frac{2Sm_{\chi_1^0}^2}{(m_{e_R}^2 - t)(m_{e_R}^2 - u)} \right\} \left( \frac{\cos\alpha}{\cos\theta_w} \right)^4 \quad (5.6)$$

where  $t = (p_1 - p_3)^2$  and  $u = (p_1 - p_4)^2$ . (Because the final state  $\chi_1^0\chi_1^0$  contains identical particles we must specify the normalization of the differential cross section. The normalization of  $d\sigma/d\cos\theta$  is such that the integral over  $\cos\theta$  from  $-1$  to  $1$  is 2 times the total cross section.) This cross section is shown in Fig. 5.1 for  $\sqrt{S} = 500$  GeV, for  $\alpha = 0$  and two cases of the mass parameters:  $m_{\chi_1^0} = 100$  GeV,  $m_{e_R} = 300$  GeV; and  $m_{\chi_1^0} = 200$  GeV,  $m_{e_R} = 600$  GeV.

### 5.3.2 Decay of the Neutralino

Since the photino component of the neutralino  $\chi_1^0$  would mainly decay into a photon and a gravitino for models ([52], [53]) in which the gravitino is extremely light, the experimental signature of the signal event we consider here is two photons and missing energy. The missing energy belongs to the two gravitinos. Other signals could be considered that involve the zino  $\tilde{Z}$  component of  $\chi_1^0$ , which would decay to a  $Z$ -boson and a gravitino; these signatures are  $\gamma Z$  with missing energy and  $ZZ$  with missing energy.

The rate of the neutralino decay  $\chi_1^0 \rightarrow \gamma \tilde{G}$  can be related to the rate of the photino decay  $\tilde{\gamma} \rightarrow \gamma \tilde{G}$  from the fact that a gaugino-like neutralino is a mixture of

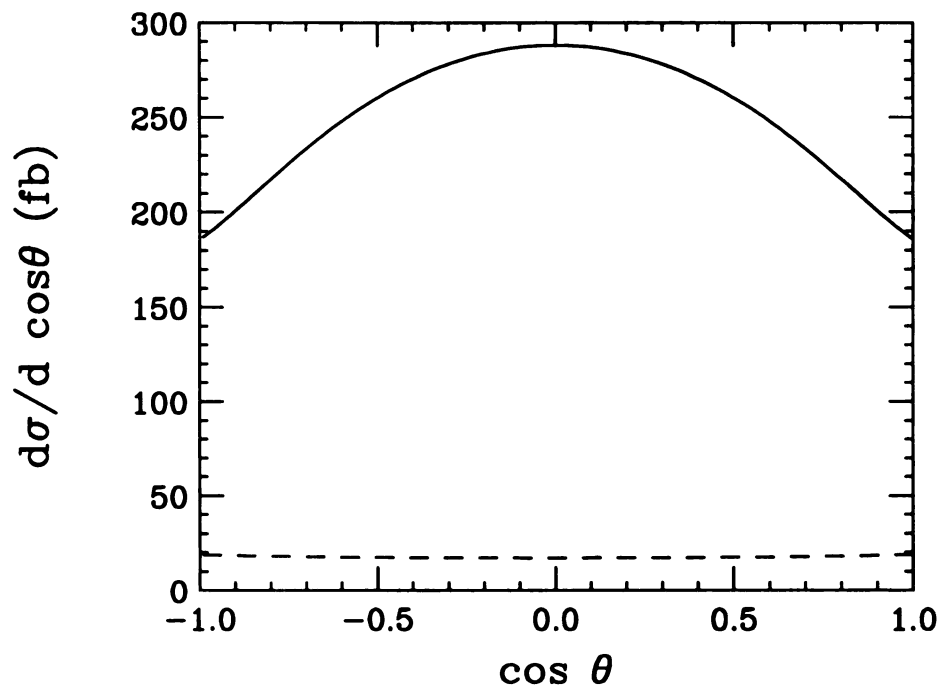


Figure 5.1: Differential cross-section  $d\sigma/d\cos\theta$  for  $e_R^-e^+ \rightarrow \chi_1^0\chi_1^0$ , where  $\theta$  is the angle of a neutralino, at  $\sqrt{s} = 500$  GeV. The mixing angle  $\alpha$  is 0, and the masses are  $m_{\chi_1^0} = 100$  GeV,  $m_{\tilde{e}_R} = 300$  GeV (solid curve), and  $m_{\chi_1^0} = 200$  GeV,  $m_{\tilde{e}_R} = 600$  GeV (dashed curve).

$\tilde{\gamma}$  and  $\tilde{Z}$

$$\chi_1^0 = \tilde{\gamma} \cos(\alpha - \theta_w) + \tilde{Z} \sin(\alpha - \theta_w) , \quad (5.7)$$

and the fact that at tree level only the  $\tilde{\gamma}$  component decays to  $\gamma\tilde{G}$ , with nearly 100% branching ratio. Therefore we have

$$\Gamma(\chi_1^0 \rightarrow \gamma\tilde{G}) = \Gamma(\tilde{\gamma} \rightarrow \gamma\tilde{G}) \cos^2(\alpha - \theta_w) . \quad (5.8)$$

The photino decay rate has been calculated [61, 59] to be

$$\Gamma(\tilde{\gamma} \rightarrow \gamma\tilde{G}) = \frac{m^5}{8\pi d^2} , \quad (5.9)$$

where  $m$  is the photino mass, assuming the photino is a mass eigenstate. In general, however,  $\tilde{\gamma}$  is not a mass eigenstate, and in Eq. (5.8) we use the neutralino mass  $m_{\chi_1^0}$ ; that is,

$$\Gamma(\chi_1^0 \rightarrow \gamma\tilde{G}) = \frac{m_{\chi_1^0}^5}{8\pi d^2} \cos^2(\alpha - \theta_w) . \quad (5.10)$$

The parameter  $d$  is related to our  $M_{susy}$  by [47]

$$d = \frac{\sqrt{3}}{\sqrt{4\pi}} m_{3/2} M_{Planck} = \frac{\sqrt{3}}{\sqrt{4\pi}} M_{susy}^2 . \quad (5.11)$$

The decay rate in Eq. (5.9) is derived by noting that at energies large compared to the gravitino mass, only the spin-1/2 component of the spin-3/2 gravitino interacts. The spin-1/2 component of the gravitino is called the Goldstino, a fermionic analogue of a Goldstone boson, because it is the massless excitation arising from the breaking of SUSY. When the local SUGRA symmetry is broken, the two components of the Goldstino combine with the two components of the massless gravitino, to make a four-component massive gravitino. Then  $\tilde{\gamma}$ - $\gamma$ - $\tilde{G}$  vertex factor, including only this Goldstino part of the gravitino coupling, is  $[\not{x}_\gamma, \gamma^\mu] \not{x}_{\tilde{G}} / 2d$  [47]. Note that the decay rate is inversely proportional to the fourth power of the supersymmetry-breaking scale  $M_{susy}$  and is proportional to the fifth power of the neutralino mass.

For  $M_{susy} = 10^6$  GeV and  $m_{\chi_1^0} = 100$  GeV, which are characteristic values for our study, the lifetime of the NLSP  $\chi_1^0$ , given by

$$\tau = \frac{1}{\Gamma} = \frac{6M_{susy}^4}{m_{\chi_1^0}^5} \frac{1}{\cos^2(\alpha - \theta_w)}, \quad (5.12)$$

is expected to be  $5 \times 10^{-10}$  sec for  $\alpha = 0$ . For  $M_{susy}$  in the range  $10^4$  to  $10^7$  GeV,  $\tau$  can vary from  $10^{-18}$  sec to  $10^{-6}$  sec.

The average distance travelled by a neutralino before it decays at the NLC is

$$D = \gamma\beta c\tau, \quad (5.13)$$

where  $\beta$  is the neutralino velocity  $\beta = \sqrt{1 - 4m_{\chi_1^0}^2/S}$  and  $\gamma = 1/\sqrt{1 - \beta^2}$ . One must observe the decay photon to make any statement about existence of a light gravitino, and to detect the photon from  $\chi_1^0 \rightarrow \gamma\tilde{G}$  the decay must occur within the detector volume. We shall assume that  $D$  must be smaller than 1 meter to observe the decay photon inside the detector. Figure 5.2, which is explained further below, shows the range of parameters  $M_{susy}$  and  $m_{\chi_1^0}$  for which at least ten signal events would be observed at the NLC.

### 5.3.3 Background-Free Signal Events

In certain circumstances there will be no background to our signal. The signal we seek is two photons plus missing energy. If the massive neutralinos live long enough before decaying into photons, then it will be possible to verify that the photons did not originate at the interaction point (IP) of the collider. In this case there will be no SM process with the same signature to act as a background. At the NLC the beam size is expected to be stable with dimensions  $\sigma_x \times \sigma_y \times \sigma_z = 5 \text{ nm} \times 300 \text{ nm} \times 100 \text{ } \mu\text{m}$  [62]. This is small enough that we may consider the interaction region to be a point. Depending on calorimeter technology, the angular resolution for the trajectory of a few Gev photon is typically in the range 10 to 100 mrad, assuming

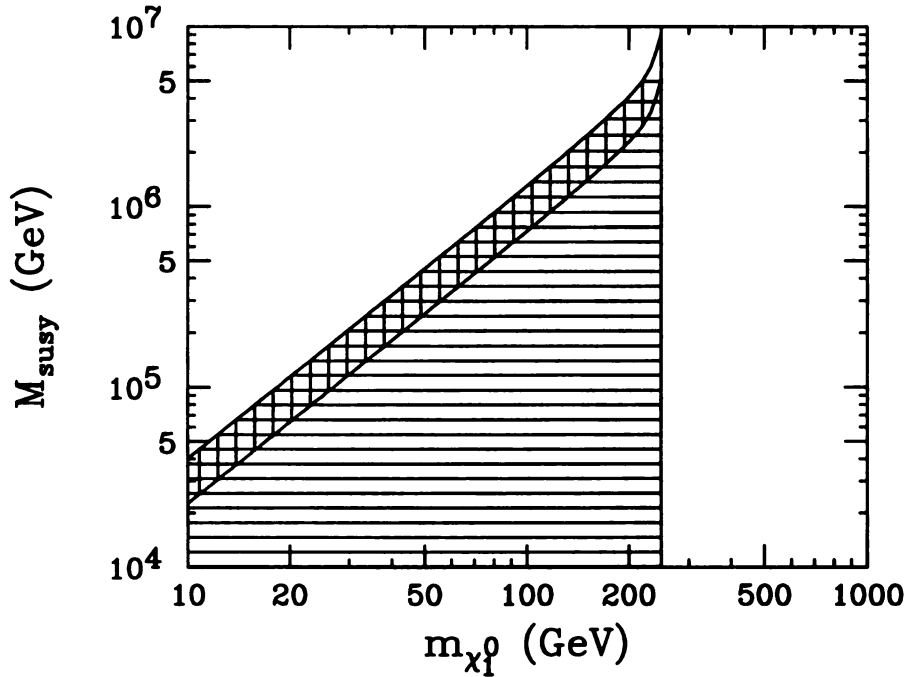


Figure 5.2: Range of parameters  $M_{\text{susy}}$  and  $m_{\chi_1^0}$  accessible at the NLC. We allow  $M_{\text{susy}}$  to vary from  $10^4$  to  $10^7$  GeV. The shaded region is the range of  $M_{\text{susy}}$  and  $m_{\chi_1^0}$  for which  $D < 1$  m and  $\sigma > 0.2$  fb, where  $D$  is the typical decay length of  $\chi_1^0$  and  $\sigma$  is the production cross-section for  $e_R^- e^+ \rightarrow \chi_1^0 \chi_1^0$  at the NLC. The bound  $\sigma > 0.2$  fb is equivalent to observing more than 10 events assuming integrated luminosity  $50 \text{ fb}^{-1}$ . The cross-shaded region is for  $10 \text{ cm} < D < 1$  m, corresponding to the background-free signal process. Parameter values for this plot are  $\alpha = 0$  and  $m_{\tilde{e}_R} = 300$  GeV.

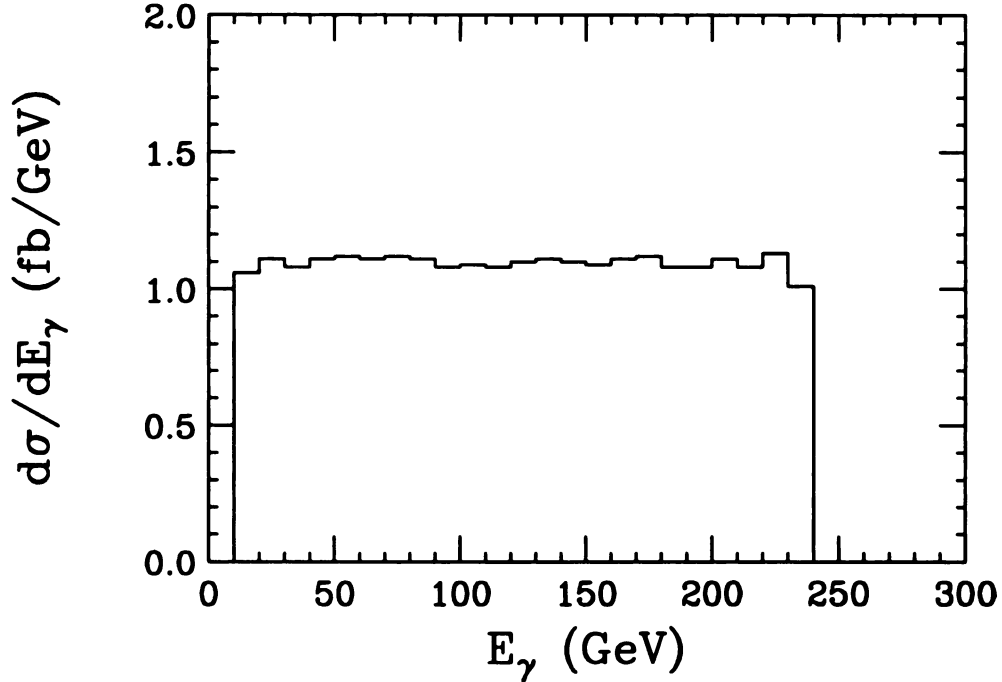


Figure 5.3: Differential cross-section in photon energy  $d\sigma/dE_\gamma$  for  $e_R^- e^+ \rightarrow \chi_1^0 \chi_1^0 \rightarrow \gamma\gamma \tilde{G}\tilde{G}$  at the NLC, assuming  $\alpha = 0$ . The mass parameter values are  $m_{\chi_1^0} = 100$  GeV and  $m_{\tilde{e}_R} = 300$  GeV. (The normalization of  $d\sigma/dE_\gamma$  is such that the integral over  $E_\gamma$  is 2 times the total cross-section, because the final state has identical photons.)

the photon originates in the inner portion of the calorimeter. Given a 1 m radius for the calorimeter, the pointing resolution to the IP would be 1 cm to 10 cm. Note that the resolution will generally improve as  $1/\sqrt{E_\gamma}$ . The typical energy  $E_\gamma$  of the photon from the decay of a massive  $\chi_1^0$  is  $\sqrt{S}/4$ ; more precisely, the distribution in photon energy is constant with  $E_\gamma$  between  $\sqrt{S}(1 - \beta)/4$  and  $\sqrt{S}(1 + \beta)/4$ , as shown in Fig. 5.3. To be conservative, we will assume that if a neutralino travels more than 10 cm before it decays, then the displaced origin of the decay photon can be well-separated from the IP at the NLC.

If  $10 \text{ cm} \leq D \leq 1 \text{ m}$ , then the typical signal event occurs within the detector but away from the IP, and the event is background-free. The range of  $M_{\text{susy}}$  and  $m_{\chi_1^0}$  in which this condition on  $D$  is satisfied is the cross-shaded region in Fig. 5.2. We allow  $M_{\text{susy}}$  to vary between  $10^4$  and  $10^7$  GeV in the figures; this range is within a

few orders of magnitude of the weak scale, as required in the models of Ref. [52]. This range corresponds to gravitino masses allowed in the SUGRA models of [53], although in these models SUSY is actually broken at a higher scale than  $M_{susy}$ . We see from figure 5.2 that for  $m_{\chi_1^0} = 100$  GeV, the background-free signal occurs for  $M_{susy}$  around  $10^6$  GeV. Conversely, for  $M_{susy} = 10^6$  GeV, the background-free range of  $m_{\chi_1^0}$  is from 85 GeV up to 122 GeV. (We note that for fixed  $M_{susy}$  and  $\sqrt{S}$ ,  $D$  is proportional to  $\beta/m_{\chi_1^0}^6$ .) However, for the lowest  $M_{susy}$  considered,  $10^4$  GeV, the background-free range of  $m_{\chi_1^0}$  would be below 10 GeV. Since we are considering a signal with no background, observing just one event would be in principle sufficient to declare the discovery of the signal. The integrated luminosity of the NLC is  $50 \text{ fb}^{-1}$  per year, so the NLC experiment is sensitive to a signal production cross section larger than 0.02 fb.

We find that over a reasonable range of the mass parameters involved in the Feynman diagrams, the cross section is larger than 1 fb. Because we chose to polarize the electron beam right-handedly, the production of  $\chi_1^0\chi_1^0$  occurs by exchange of a right selectron  $\widetilde{e}_R$ , and the cross section depends on the mass of  $\widetilde{e}_R$ . (In this work, we shall ignore the possible small mixing between  $\widetilde{e}_R$  and  $\widetilde{e}_L$  so that  $\widetilde{e}_R$  is the mass eigenstate with mass  $m_{\widetilde{e}_R}$ .) We are assuming, in accord with the models of references [52] and [53], that the LSP is the gravitino and the NLSP is  $\chi_1^0$ , so  $\widetilde{e}_R$  must be heavier than  $\chi_1^0$ . Also, in both sets of models, we expect  $m_{\widetilde{e}_R}$  to be of the same order as  $m_{\chi_1^0}$ , because sfermion masses squared ( $m_{\widetilde{e}_R}^2$ ) depend on a two-loop diagram while gaugino masses ( $m_{\chi_1^0}$ ) depend on a one-loop diagram. (The details depend on the gauge groups assumed in the model.) In Table 5.1 we give the signal production cross section  $\sigma$  for a few choices of  $m_{\chi_1^0}$  and  $m_{\widetilde{e}_R}$  at the NLC, assuming  $M_{susy} = 10^6$  GeV. In all cases the cross section is larger than 1 fb. We conclude that for  $M_{susy} = 10^6$  GeV and  $m_{\widetilde{e}_R}$  less than 1 TeV, the NLC guarantees the discovery of

Table 5.1: Production cross-section  $\sigma$  and typical decay distance  $D$  for the process  $e_R^- e^+ \rightarrow \chi_1^0 \chi_1^0$  at the NLC, assuming  $\alpha = 0$ , for several values of masses. (Note that the electron beam is right-hand polarized, so the cross-section is a factor of 2 larger than that for an unpolarized electron beam.) These numbers are for  $M_{\text{susy}} = 10^6$  GeV.

$m_{\chi_1^0}$ (GeV)	$m_{\tilde{e}_R}$ (GeV)	$\sigma$ (fb)	$D$ (m)
100	100	670	0.35
100	300	252	0.35
100	600	57.1	0.35
100	1000	11.7	0.35
200	300	84.6	0.0036
200	600	17.6	0.0036
200	1000	3.4	0.0036

the background-free signal event if  $85 \text{ GeV} \leq m_{\chi_1^0} \leq 122 \text{ GeV}$ .

Table 5.1 also shows the typical decay length  $D$  in the various cases. In fact, it is the decay length  $D$ , not the production cross section  $\sigma$ , that constrains the discovery of the background-free signal event, because  $\sigma$  is larger than 0.02 fb for  $m_{\chi_1^0} < \sqrt{S}/2 = 250 \text{ GeV}$  and  $m_{\tilde{e}_R} < 1 \text{ TeV}$  except when  $m_{\chi_1^0}$  is extremely close to  $\sqrt{S}/2$ . Our conclusion does not change even if we require observation of at least 10 signal events to declare discovery of the signal.

The shaded region in Fig. 5.2 shows the values of  $M_{\text{susy}}$  and  $m_{\chi_1^0}$  for which  $D \leq 1 \text{ m}$  and for which the number of events at the NLC ( $\sigma \times 50 \text{ fb}^{-1}$ ) is greater than 10. The diagonal boundary on the left is the curve  $D = 1 \text{ m}$ , and the vertical boundary on the right is where the number of events equals 10. The cross section  $\sigma$  does not depend on  $M_{\text{susy}}$  so the boundary on the right side is a vertical line near the threshold at  $m_{\chi_1^0} = \sqrt{S}/2 = 250 \text{ GeV}$ . Figure 5.2 is for  $m_{\tilde{e}_R} = 300 \text{ GeV}$ , where the right selectron  $\tilde{e}_R$  is the exchanged particle in the process  $e_R^- e^+ \rightarrow \chi_1^0 \chi_1^0$ . Increasing  $m_{\tilde{e}_R}$  up to 1 TeV only slightly shifts the vertical boundary on the right toward the left. The cross-shaded region has  $10 \text{ cm} \leq D \leq 1 \text{ m}$ , corresponding to

the background-free signal. The two diagonal boundary curves depend only on the kinematics, not on the cross section, so they do not depend on the selectron mass  $m_{\tilde{e}_R}$ .

This calculation in terms of the average decay length  $D$  provides a rough estimate of the parameters  $M_{susy}$  and  $m_{\chi_1^0}$  for which background-free events occur. The cross-shaded region in Fig. 5.2 is the region of parameter space where the average decay distance of the neutralino  $D = \beta\gamma c\tau$  is between  $r_{min} = 0.1$  m and  $r_{max} = 1$  m. However, the cross section is large enough that there will be events in which the neutralinos decay in a distance between  $r_{min}$  and  $r_{max}$  even though their *average* decay distance is outside that range.

To calculate a more precise parameter range for background-free events, let  $P(r)dr$  be the probability that a neutralino travels a distance between  $r$  and  $r + dr$  before decaying

$$P(r) = \frac{1}{D} e^{-r/D} . \quad (5.14)$$

Then the fraction of events for which both neutralinos decay in a distance between  $r_{min}$  and  $r_{max}$  is

$$f_{BF} = \left( \int_{r_{min}}^{r_{max}} P(r) dr \right)^2 . \quad (5.15)$$

If we require that there are more than 10 background-free events, given integrated luminosity equal to  $50 \text{ fb}^{-1}$ , then we must have

$$\sigma f_{BF} > 0.2 \text{ fb} , \quad (5.16)$$

where  $\sigma$  is the production cross section. The range of parameters that satisfy this condition is larger than the simpler estimate in Fig. 5.2, and is shown as the cross shaded region in Fig. 5.4.

In the rest of the shaded region, *i.e.*, not including the cross-shaded region, the decays occur within 10 cm of the IP. We assume conservatively it is not possible to detect a displaced vertex of these decay photons. For these values of  $M_{susy}$

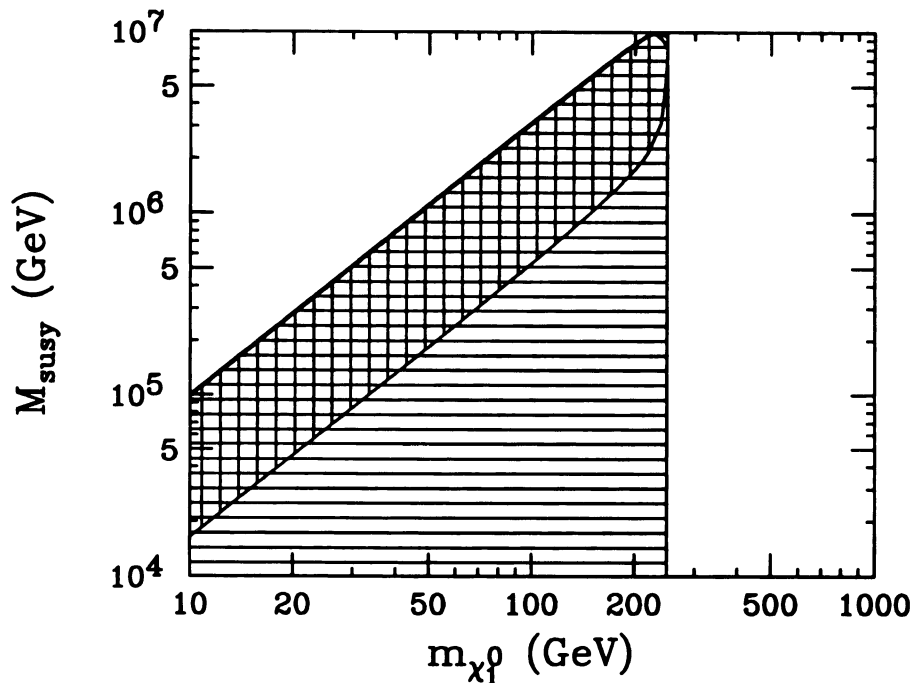


Figure 5.4: Same as Fig. 5.2, but with a more precise calculation as described in Section 5.3.3.

and  $m_{\chi_1^0}$  there are intrinsic backgrounds to the signal process, which we discuss next.

### 5.3.4 Non-Background-Free Signal Events

As shown in Fig. 5.2 and Table 5.1, assuming  $M_{\text{susy}} = 10^6$  GeV, if  $m_{\chi_1^0} \geq 120$  GeV then the decay length  $D$  is less than 10 cm, which does not satisfy the criterion for being a background-free signal event. The experimental signature of the signal event in this case consists of two photons coming out of the interaction region with large missing energy. Any background will consist of a standard process with a similar event signature. Before identifying these processes, let us examine the details of the signal event, so that we may better distinguish them from the features of the various backgrounds.

To obtain the distributions of the decay photons we evaluated the full correlated helicity amplitudes including the decays of the two neutralinos. However, we did

not find a noticeable difference compared to a simpler calculation in which the decays of the  $\chi_1^0$ 's are treated independently, ignoring the correlation between their polarizations. Figure 5.3 shows the distribution of the single-photon energy  $E_\gamma$ , for  $m_{\chi_1^0} = 100$  GeV and  $m_{\tilde{e}_R} = 300$  GeV. The distribution is approximately constant with  $E_\gamma$  between  $\sqrt{S}(1 - \beta)/4$  and  $\sqrt{S}(1 + \beta)/4$ , so the order of magnitude of the photon energies is  $\sqrt{S}/4$ . Typically, each photon has large transverse momentum  $p_T^\gamma$ . Figure 5.5 shows the  $p_T^\gamma$  distribution of either photon, for  $m_{\chi_1^0} = 100$  GeV and  $m_{\tilde{e}_R} = 300$  GeV. If  $\chi_1^0$  is heavy, then the two decay photons are acollinear, which indicates missing transverse momentum. If  $\chi_1^0$  is light, then due to the large momenta of the  $\chi_1^0$ 's the two photons will tend to be more nearly back-to-back, but the sum of the two photon energies will still be peaked at about  $\sqrt{S}/2$ , which indicates missing energy. This latter feature of the signal event is shown in Fig. 5.6, which is the distribution of the sum of photon energies, for  $m_{\chi_1^0} = 100$  GeV and  $m_{\tilde{e}_R} = 300$  GeV. (Figures 3–5 are for  $\alpha = 0$ .)

Since the signal event consists of two photons, the first obvious background process to consider is the ordinary QED process  $e_R^- e^+ \rightarrow \gamma\gamma$ . However, the photon kinematics for this process are much different than for the signal process: The photons will be approximately back-to-back with combined energy  $\sqrt{S}$ . Initial state radiation can change the energy by a small amount, but at the NLC it is expected that the effects of bremsstrahlung will not significantly change the available center-of-mass energy of the  $e^- e^+$  system [19]. Hence in events generated from the QED process  $e_R^- e^+ \rightarrow \gamma\gamma$ , including possible initial state radiation, the sum of the two photon energies is close to  $\sqrt{S}$ . By demanding that the sum of the two photon energies is around  $\sqrt{S}/2$ , indicating large missing energy in the event, and that the two photons are not back-to-back, one can eliminate the large background from photon pair production.

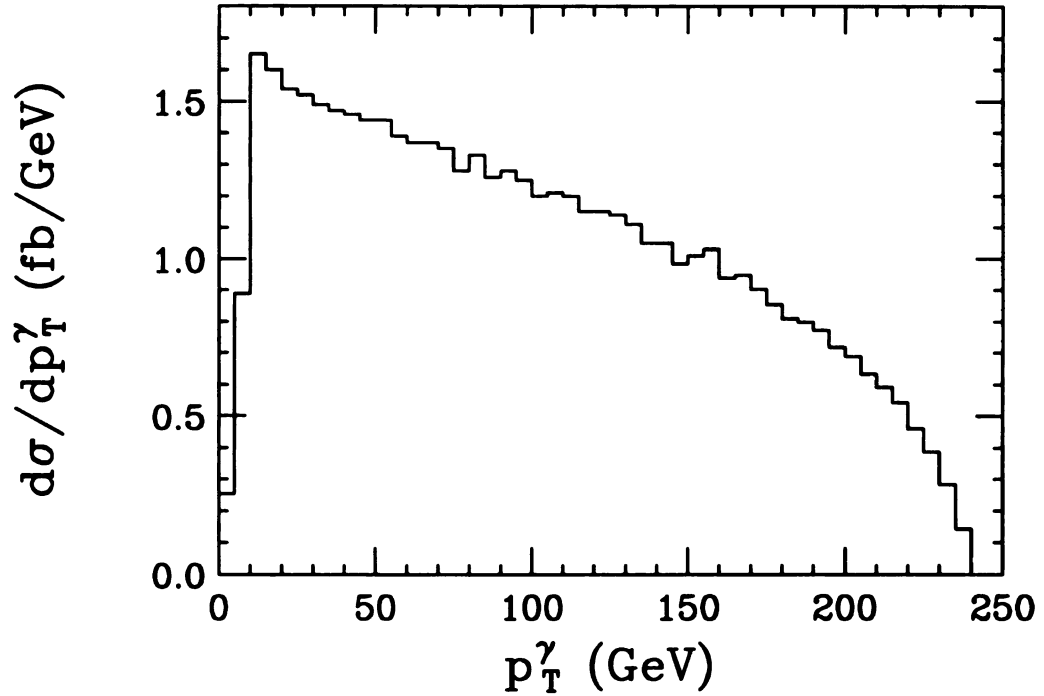


Figure 5.5: Differential cross-section in photon transverse momentum  $d\sigma/dp_T^\gamma$  for  $e_R^- e^+ \rightarrow \chi_1^0 \chi_1^0 \rightarrow \gamma\gamma \tilde{G}\tilde{G}$  at the NLC, assuming  $\alpha = 0$ . The mass parameter values are  $m_{\chi_1^0} = 100$  GeV and  $m_{\tilde{e}_R} = 300$  GeV. (The normalization of  $d\sigma/dp_T^\gamma$  is such that the integral over  $p_T^\gamma$  is 2 times the total cross-section, because the final state has identical photons.)

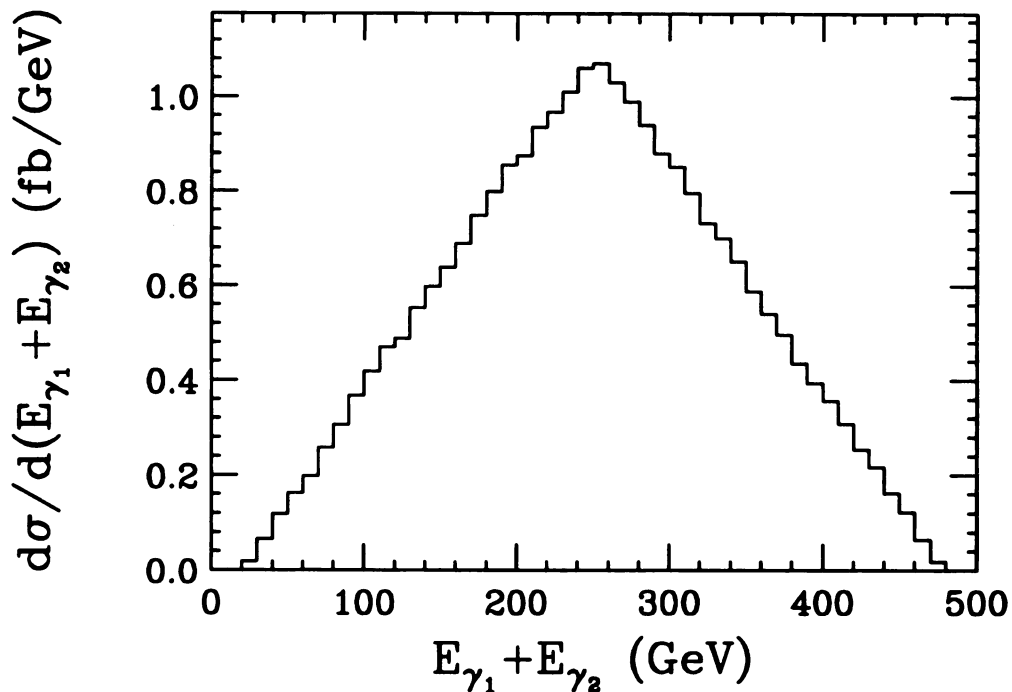


Figure 5.6: Differential cross-section in the sum of photon energies  $d\sigma/d(E_{\gamma_1} + E_{\gamma_2})$  for  $e_R^- e^+ \rightarrow \chi_1^0 \chi_1^0 \rightarrow \gamma\gamma\tilde{G}\tilde{G}$  at the NLC, assuming  $\alpha = 0$ . The mass parameter values are  $m_{\chi_1^0} = 100$  GeV and  $m_{\tilde{e}_R} = 300$  GeV.

Another background process at the NLC is  $e_R^- e^+ \rightarrow \gamma\gamma Z$  with the  $Z$ -boson decay  $Z \rightarrow \nu\bar{\nu}$ . This process has large missing energy carried away by the neutrino pair. We have calculated the cross section for this background process. The cross section diverges at low transverse momentum  $p_T$  of either photon, so we require  $p_T$  to be larger than 20 GeV for each photon. We find that this background cross section is 14.7 fb (including three neutrino flavors from  $Z$ -boson decays) which is rather small (*cf.* Table 1). For comparison, with the same  $p_T$  cut on the photons the production cross section of the signal event  $e_R^- e^+ \rightarrow \chi_1^0 \chi_1^0 \rightarrow \gamma\gamma\tilde{G}\tilde{G}$  is 210 fb for  $m_{\chi_1^0} = 100$  GeV and  $m_{\tilde{e}_R} = 300$  GeV, and it is 16.9 fb for  $m_{\chi_1^0} = 200$  GeV and  $m_{\tilde{e}_R} = 600$  GeV. Although the  $\gamma\gamma Z$  cross section is comparable to the signal cross section in the limit of large SUSY-partner masses, this background event can be easily distinguished from the signal event: The missing energy in the  $\gamma\gamma Z$  event is entirely due to the decay of the  $Z$ -boson, so the invariant mass of the invisible particles (the  $\nu\bar{\nu}$  pair)

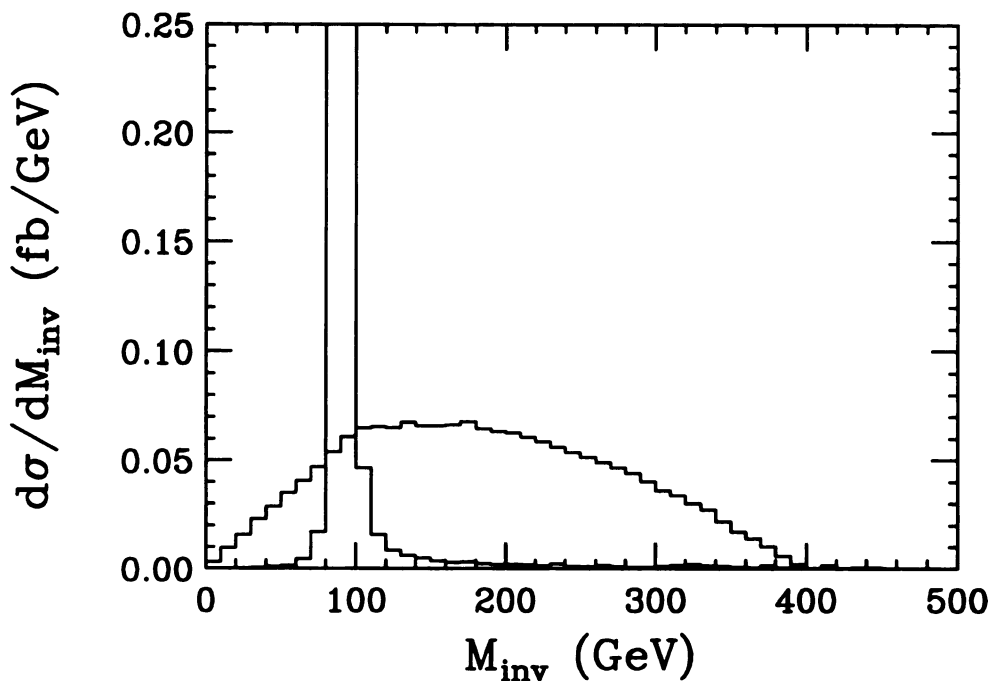


Figure 5.7: Differential cross-section  $d\sigma/dM_{inv}$  in the invariant mass of invisible particles  $M_{inv}$  for the signal process  $e_R^- e^+ \rightarrow \chi_1^0 \chi_1^0 \rightarrow \gamma\gamma \tilde{G}\tilde{G}$ , and for the background process  $e_R^- e^+ \rightarrow \gamma\gamma Z$ , with decay  $Z \rightarrow \nu\bar{\nu}$ . The photon transverse momenta are required to be greater than 20 GeV. The masses for the signal process are  $m_{\chi_1^0} = 200$  GeV and  $m_{e_R^-} = 600$  GeV.

is peaked at the  $Z$ -boson mass. The invariant mass can be determined from the visible energy, *i.e.*, the energy of the initial state and the two photons. We define this invariant mass squared to be  $M_{inv}^2 = (p_{e^-} + p_{e^+} - p_{\gamma_1} - p_{\gamma_2})^2$ . The invariant-mass peak for the  $\gamma\gamma Z$  background event is shown in Fig. 5.7, along with the distribution in  $M_{inv}$  for signal events with  $m_{\chi_1^0} = 200$  GeV and  $m_{e_R^-} = 600$  GeV. The signal distribution is broad, so requiring  $M_{inv}$  to be away from the  $Z$ -peak to discriminate against the  $\gamma\gamma Z$  events would further suppress this already small background. For instance, as seen in Fig. 5.7, if we require  $|M_{inv} - m_Z| > 20$  GeV, then the ratio of signal to background becomes  $14.6 \text{ fb}/0.7 \text{ fb}=21$ , as compared to  $16.9 \text{ fb}/14.7 \text{ fb}=1.15$  without the invariant-mass cut.

We have noted in the previous section that the search for our signal is limited by kinematics rather than cross section, so we need not fear such cuts. Figure 5.8

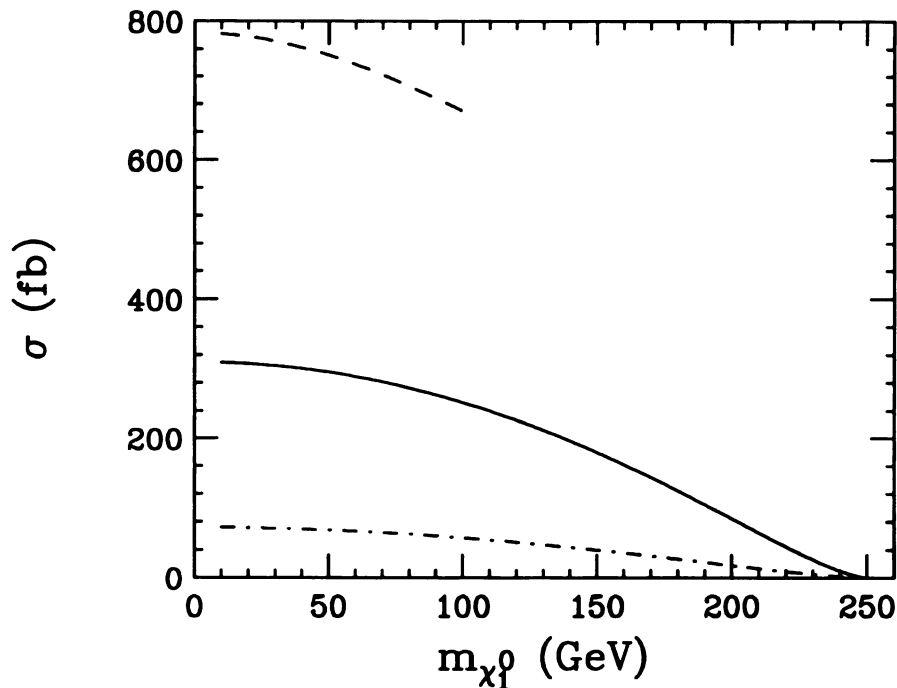


Figure 5.8: Total cross-section at the NLC for the process  $e_R^- e^+ \rightarrow \chi_1^0 \chi_1^0$  with  $\alpha = 0$ , as a function of  $m_{\chi_1^0}$  for  $m_{e_R^-} = 300$  GeV (solid curve),  $m_{e_R^-} = 100$  GeV (dashed curve), and  $m_{e_R^-} = 600$  GeV (dot dashed curve). (Note that only  $m_{\chi_1^0} < m_{e_R^-}$  is allowed in the models we consider because  $\chi_1^0$  is the NLSP.)

shows the  $\chi_1^0 \chi_1^0$  production cross section  $\sigma$  for a few choices of  $m_{e_R^-}$ , as a function of  $m_{\chi_1^0}$  at the NLC. The order of magnitude of  $\sigma$  is 100 fb. We conclude that it is possible to observe the non-background-free signal event at the NLC with  $50 \text{ fb}^{-1}$  integrated luminosity, for all the shaded region shown in Fig. 5.2 except if  $m_{\chi_1^0}$  is extremely close to the threshold for  $\chi_1^0 \chi_1^0$  production, which is  $\sqrt{S}/2 = 250$  GeV for the NLC.

Before closing this section, we comment on the reason for using a right-hand polarized  $e^-$  beam for the proposed experiment. Polarization has little effect on the backgrounds already discussed. As the QED coupling is pure vector, the cross section for  $e_R^- e^+ \rightarrow \gamma \gamma$  is independent of electron polarization. Because the vector part of the  $e$ - $e$ - $Z$  coupling is proportional to  $1 - 4 \sin^2 \theta_w$ , which is small, this coupling is approximately pure axial vector. Thus the background which produces a photon

pair and a Z boson is also nearly independent of the electron polarization. The signal process, on the other hand, may differ for the two polarization cases.  $e_R^- e^+ \rightarrow \chi_1^0 \chi_1^0$  occurs by exchange of a  $\widetilde{e}_R$ , which does not interact with the  $\widetilde{W}^3$  component of  $\chi_1^0$ ; whereas  $e_L^- e^+ \rightarrow \chi_1^0 \chi_1^0$  occurs by exchange of a  $\widetilde{e}_L$ , which does couple to  $\widetilde{W}^3$ . Furthermore, the masses of  $\widetilde{e}_R$  and  $\widetilde{e}_L$  may be different. We might expect the  $\widetilde{e}_L$  to be heavier due to extra contributions from the weak interaction [59]. A heavier left selectron mass would suppress the left polarized cross section, leading one to choose the right polarization.

In any case, running the experiment with a right-polarized electron beam also eliminates a background we have not yet considered, the process  $e^- e^+ \rightarrow \nu_e \bar{\nu}_e \gamma \gamma$ . The complete gauge-invariant set of diagrams for this process includes the diagrams for  $e^- e^+ \rightarrow \gamma \gamma Z (\rightarrow \nu_e \bar{\nu}_e)$ , discussed above, but also includes diagrams involving  $e$ - $\nu_e$ - $W$  interactions. These contributions to  $e^- e^+ \rightarrow \nu_e \bar{\nu}_e \gamma \gamma$  arise from Feynman diagrams in which a t-channel W boson is exchanged between the two fermion lines. A right-polarized electron beam eliminates this additional background, because the W coupling to fermions is pure left-handed. Therefore a right-hand polarized electron beam has a significantly better ratio of signal to backgrounds, compared to an unpolarized  $e^-$  beam. Predicting this additional background due to W boson interactions for the NLC with less than 100% right-hand polarization of the electron beam, or for current colliders which have weaker polarization capability, is a topic for a more detailed study.

## 5.4 Discussion and Conclusion

We have discussed the possibility of detecting a light gravitino at the NLC, a proposed future  $e^- e^+$  collider with center-of-mass energy  $\sqrt{S} = 500$  GeV and with a

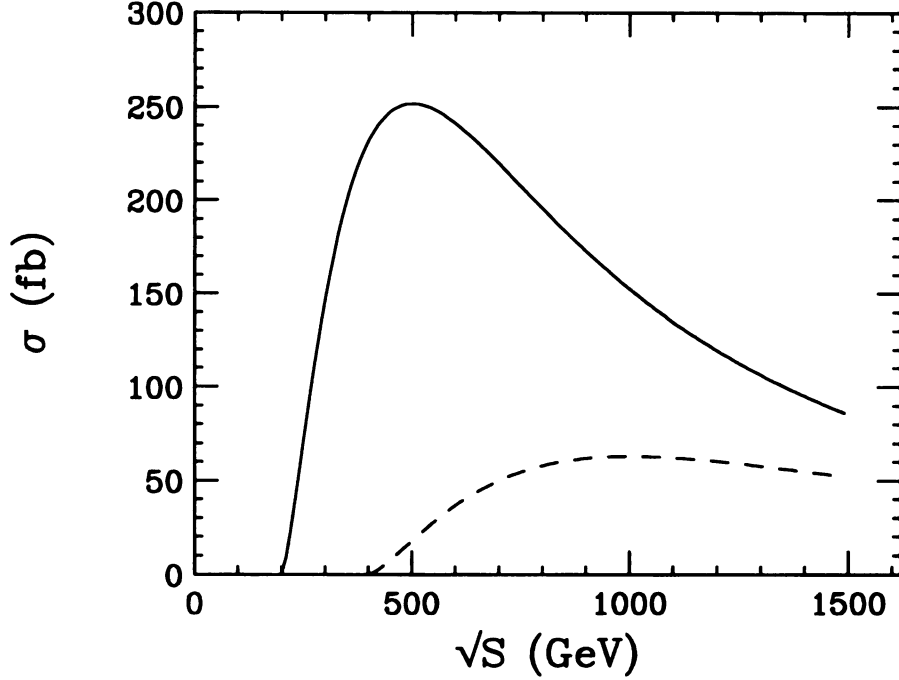


Figure 5.9: Total cross-section for the process  $e_R^- e^+ \rightarrow \chi_1^0 \chi_1^0$  with  $\alpha = 0$ , as a function of  $\sqrt{S}$ . The mass parameter values are  $m_{\chi_1^0} = 100$  GeV,  $m_{\tilde{e}_R} = 300$  GeV (solid curve), and  $m_{\chi_1^0} = 200$  GeV,  $m_{\tilde{e}_R} = 600$  GeV (dashed curve).

right-hand polarized  $e^-$  beam, from the decay  $\chi_1^0 \rightarrow \gamma \tilde{G}$  where the neutralino  $\chi_1^0$  is produced in pairs in the  $e^- e^+$  collisions. The proposed NLC would also operate at  $\sqrt{S} = 1$  or 1.5 TeV with a luminosity of  $200 \text{ fb}^{-1}$  per year. Figure 5.9 shows the total cross section  $\sigma(e_R^- e^+ \rightarrow \chi_1^0 \chi_1^0)$  for a gaugino-like  $\chi_1^0$  with  $\alpha = 0$ , as a function of  $\sqrt{S}$ , for two cases of the mass parameters:  $m_{\chi_1^0} = 100$  GeV  $m_{\tilde{e}_R} = 300$  GeV, and  $m_{\chi_1^0} = 200$  GeV  $m_{\tilde{e}_R} = 600$  GeV. If  $m_{\chi_1^0}$  is large then the cross section increases with  $\sqrt{S}$ ; but if  $m_{\chi_1^0} = 100$  GeV then the cross section actually decreases as  $\sqrt{S}$  increases from 500 GeV to 1 TeV.

The ranges of the parameters  $M_{susy}$  and  $m_{\chi_1^0}$  that are accessible for the three modes of the NLC are shown in Fig. 5.10. (For simplicity, we did not separate the regions of parameters for background-free signal events from those for non-background-free signal events, as we did in Fig. 5.2.) It is clearly seen that at 500 GeV the NLC will probe a slightly larger region of the parameters  $M_{susy}$  and

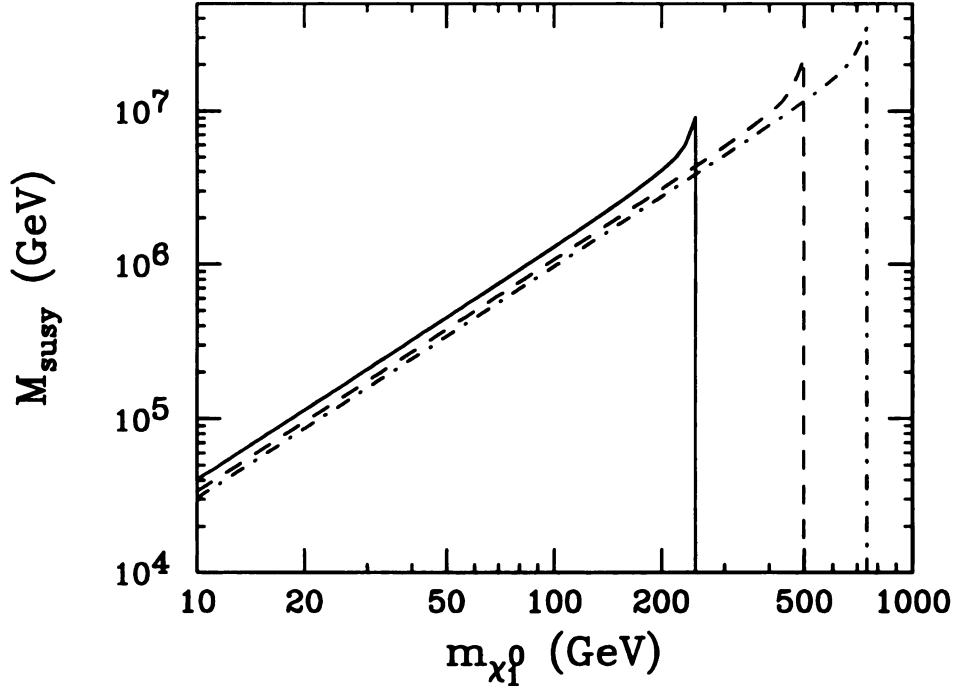


Figure 5.10: Range of parameters  $M_{\text{susy}}$  and  $m_{\chi_1^0}$  accessible at the NLC with  $\sqrt{s} = 500$  GeV (solid line), 1 TeV (dashed line), and 1.5 TeV (dot-dash line). The luminosity per year is 50, 200 and 200  $\text{fb}^{-1}$ , respectively. Mass parameter values are  $m_{\tilde{e}_R} = 300$  GeV, 500 GeV and 750 GeV, respectively, and the mixing angle  $\alpha$  is 0. The interior of each triangle is the region where the number of events is greater than 10, and  $D < 1$  m.

$m_{\chi_1^0}$  than a TeV NLC if  $m_{\chi_1^0} < 250$  GeV. At higher  $\sqrt{S}$  the neutralinos are more likely to exit the detector before decaying. Therefore, a TeV NLC is needed to detect a light gravitino through the event signature of 2 photons plus missing energy, only if the NLSP  $\chi_1^0$  is heavier than about 250 GeV.

We should also consider whether this process can be discovered at a current  $e^-e^+$  or  $p\bar{p}$  collider. First consider the case of LEP/SLC, with center-of-mass energy  $\sqrt{S} = m_Z = 91$  GeV and integrated luminosity  $450 \text{ pb}^{-1}$  (which is about the integrated luminosity at  $m_Z$  when combining all the experiments from LEP and SLC), and also LEP-II, with center-of-mass energy  $\sqrt{S} = 190$  GeV and luminosity  $500 \text{ pb}^{-1}$  per year per experiment. Figure 5.11 shows the range of parameters  $M_{\text{susy}}$  and  $m_{\chi_1^0}$  accessible by LEP/SLC, LEP-II, and the NLC, superimposed, with the same

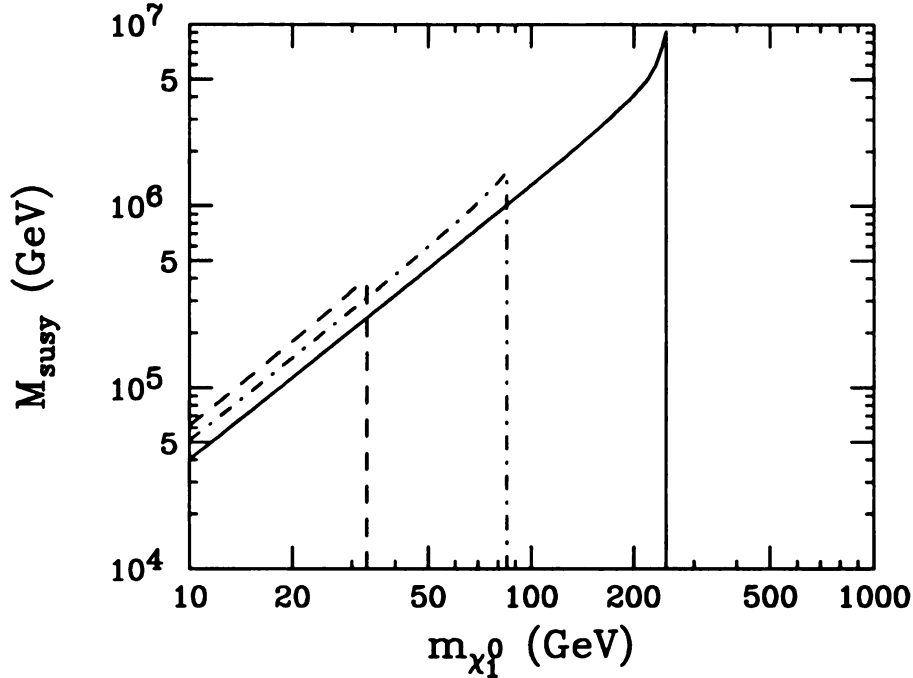


Figure 5.11: Range of parameters  $M_{\text{susy}}$  and  $m_{\chi_1^0}$  accessible at the NLC (solid line), LEP/SLC (dashed line), and LEP-II (dot-dash line). The interior of each triangle is the region where the number of events is greater than 10, and  $D < 1$  m. Parameter values for this plot are  $\alpha = 0$  and  $m_{\tilde{e}_R} = 300$  GeV.

assumptions as Fig. 5.2.

The accessible region depends mainly the threshold mass  $m_{\chi_1^0} = \sqrt{S}/2$ ; and on kinematics, *i.e.*, on the requirement that  $D < 1$  m, where  $D$  is the mean distance traveled by the neutralino before it decays. In the case of a gaugino-like  $\chi_1^0$  at the NLC we found that the cross section for right-handed electrons is of order 100 fb (*cf.* Table 1), large enough to discover the signal even for large  $m_{\tilde{e}_R}$  and  $m_{\chi_1^0}$  near the threshold. In the case of LEP/SLC or LEP-II with unpolarized  $e^-$  beam, the cross section depends on the masses of both selectrons ( $\tilde{e}_R$  and  $\tilde{e}_L$ ), but if we assume these masses are about equal then we may *estimate* that the unpolarized cross section is approximately equal to the right-handed  $e^-$  cross section. The boundaries for LEP/SLC and LEP-II in Fig. 5.11 were calculated with this assumption, with  $m_{\tilde{e}_R} = m_{\tilde{e}_L} = 300$  GeV. For example, the cross section for LEP-II ( $\sqrt{S} = 190$  GeV)

with  $m_{\chi_1^0} = 100$  GeV and  $m_{\tilde{e}_R} = m_{\tilde{e}_L} = 300$  GeV is 143 fb. In Fig. 5.11 the triangular area enclosed by the curve for each collider is the range of parameters such that there would be 10 events (total for LEP/SLC, or per year per experiment for LEP-II or the NLC), with average decay length  $D < 1$  m.

Figure 5.11 implies that for  $M_{susy}$  between  $10^4$  GeV and  $10^7$  GeV, the range relevant to the model of Ref. [52], only the region of parameter space with  $m_{\chi_1^0} \lesssim 30$  GeV is accessible at LEP/SLC; however, an interesting region for  $M_{susy} < 10^6$  GeV will be accessible at LEP-II. However, because the electron beam polarization at LEP-II is only of order 50%, there is a background from left-handed electrons: the process  $e^-e^+ \rightarrow \nu_e\bar{\nu}_e\gamma\gamma$  in which a  $W$ -boson is exchanged between the fermions. This background may be significant at the level of 10 events. A definitive analysis of a LEP-II search for the gravitino process must include this background.

Next we turn to the Tevatron  $p\bar{p}$  collider. We have calculated the cross section for the process  $p\bar{p} \rightarrow \chi_1^0\chi_1^0$  at  $\sqrt{s} = 2$  TeV, for bino-like  $\chi_1^0$ , using a Monte Carlo program with CTEQ2 parton distribution functions. We find that the cross section is 19 fb for  $m_{\chi_1^0} = 100$  GeV and  $m_{\tilde{q}} = 100$  GeV, where  $\tilde{q}$  indicates any squark. The cross section decreases with  $m_{\tilde{q}}$ . Because of the small production rate (about a factor of 35 smaller than a 500 GeV  $e^+e^-$  collider) and the additional large backgrounds in hadron collisions (either from physics processes or from the imperfectness of the detector), the current total integrated luminosity of the Tevatron is probably too small to provide a useful search for the light gravitino. With the upgrade of the Tevatron, at which the luminosity will increase by an order of magnitude (to about  $2\text{fb}^{-1}$  per year), one can probably detect the light gravitino for some values of  $M_{susy}$  and  $m_{\chi_1^0}$ . This requires a separate study as well. The Tevatron and LEP are considered in detail in Reference [55].

In conclusion, the proposed NLC could provide a means to search for the decay

of a gaugino-like Next-to-Lightest-Supersymmetric-Particle  $\chi_1^0$  into a gravitino and photon,  $\chi_1^0 \rightarrow \gamma\tilde{G}$ , for a significant part of the parameter space relevant to models in which the SUSY-breaking scale is within a few orders of magnitude of the weak scale. Models with a light gravitino but a higher SUSY-breaking scale would also be probed by the NLC. The range  $10^5 \text{ GeV} < M_{\text{susy}} < 10^7 \text{ GeV}$  corresponds to gravitino masses in the range  $1 \text{ eV} < m_{3/2} < 10 \text{ keV}$ . This range of parameters could be accessible at the NLC, depending on the neutralino mass. The neutralino pair production cross section is large enough, of order 100 fb, that it is not a limiting factor. The limiting factor is the lifetime of the NLSP, which is proportional to  $M_{\text{susy}}^4$ . If  $M_{\text{susy}}$  is too large, then the NLSP will exit the detector before decaying, and no information on the gravitino will be obtained. But as shown in Fig. 5.2, if  $M_{\text{susy}}$  is small enough for a given neutralino mass  $m_{\chi_1^0}$ , then the neutralinos will decay inside the NLC detector. The decay  $\chi_1^0 \rightarrow \gamma\tilde{G}$  can then be used to detect the gravitino by seeing the two photons with large missing energy from  $\chi_1^0$  pair production.

This study was motivated by the class of gauge-mediated dynamical SUSY-breaking models, which require a light gravitino. We investigated the possibility of observing the light gravitino at the NLC, and found that for a large region of the parameter space, the gravitino would be produced copiously and within the detector. Therefore, non-detection of the gravitino would rule out a region of parameter space of the gauge-mediated models. Detection would narrow the field of viable SUSY-breaking models, providing evidence for the gauge-mediated scenario—though not proof, since other models do exist which allow a light gravitino.

## 5.5 Additional Comments

After completing this work we received the paper “Experimental Signatures of Low Energy Gauge Mediated Supersymmetry Breaking”, by S. Dimopoulos, M. Dine,

S. Raby and S. Thomas [54], which is similar and complementary to this chapter.

Also, an  $ee\gamma\gamma$  plus missing transverse energy event was reported by CDF at the Fermilab collider which seems to have no SM interpretation, and may be consistent with a light gravitino SUSY scenario. This and another SUSY interpretation of the event are analyzed in Ref. [63]. The authors of Ref. [63] also consider other signals which can occur at the Fermilab Tevatron or LEP II in the light gravitino scenario. In Ref. [64], the CDF event is considered in the “no-scale” SUGRA framework.

# APPENDICES

# Appendix A

## The Standard Model Lagrangian

After symmetry-breaking, the physical fields can be written in terms of the  $SU(3)_C \times SU(2)_L \times U(1)_Y$  fields:

$$\begin{aligned} W^{\mu\pm} &= \frac{1}{\sqrt{2}}(W_1^\mu \mp iW_2^\mu), \\ Z^{0,\mu} &= (-B^\mu \sin \theta_W + W_3^\mu \cos \theta_W), \\ A^\mu &= (B^\mu \cos \theta_W + W_3^\mu \sin \theta_W), \end{aligned}$$

where the Weinberg angle  $\theta_W$  parametrizes the mixing of the electroweak fields. In the unitary gauge the Higgs field can be written in terms of one real field  $\eta$  and a constant vacuum expectation value  $v$ :

$$\Phi(\mathbf{x}) = \begin{pmatrix} 0 \\ [v + \eta(\mathbf{x})] / \sqrt{2} \end{pmatrix}$$

The Lagrangian is then:

$$L_{SM} = L_{boson} + L_{lepton} + L_{quark}.$$

$$\begin{aligned} L_{boson} &= -\frac{1}{4}F_{\mu\nu,a}(G)F_a^{\mu\nu}(G) - \frac{1}{2}\lambda(\partial \cdot G)^2 \\ &- \frac{1}{2}|\bar{D}_\mu W_\nu^+ - \bar{D}_\nu W_\mu^+|^2 \\ &+ M_W^2(W_\mu^+)^*W^{\mu+} - \frac{1}{4}Z_{\mu\nu}^0 Z^{0,\mu\nu} + \frac{1}{2}M_Z^2 Z_\mu^0 Z^{0,\mu} - \frac{1}{4}A_{\mu\nu}A^{\mu\nu} \end{aligned} \tag{A.1}$$

$$\begin{aligned}
& - \frac{1}{2}i[g \cos \theta_W Z_{\mu\nu}^0 + eA_{\mu\nu}](W^{+\mu}W^{-\nu} - W^{-\mu}W^{+\nu}) \quad (\text{A.2}) \\
& + \frac{1}{4}g^2(W_\mu^+W_\nu^- - W_\mu^-W_\nu^+)^2 \\
& + \frac{1}{8}[g^2(|W^+|^2 + |W^-|^2) + (g'^2 + g^2)Z_\mu^0Z^{0,\mu}](2v\eta + \eta^2) \\
& + \frac{1}{2}[(\partial^\mu\eta)(\partial_\mu\eta) - 2\mu^2\eta^2] - v\lambda\eta^3 - \frac{1}{4}\lambda\eta^4,
\end{aligned}$$

where Latin indices run from 1 to 8 in color space, and Greek indices run from 1 to 4 in Minkowski space. The terms labelled A.1 and A.2 are discussed in the Introduction; they are responsible for electroweak gauge tri-boson couplings. In terms of the physical fields the covariant derivative is

$$\bar{D}_\mu \equiv \partial_\mu + ig(Z_\mu^0 \cos \theta_W + A_\mu \sin \theta_W),$$

and the field strength tensors are

$$\begin{aligned}
F_{\mu\nu,\bar{a}}(G) &= \partial_\mu G_{\nu,\bar{a}} - \partial_\nu G_{\mu,\bar{a}} - g_s f_{\bar{a},\bar{b},\bar{c}} G_{\mu,\bar{b}} G_{\nu,\bar{c}}, \\
A_{\mu\nu} &= \partial_\mu A_\nu - \partial_\nu A_\mu, \\
Z_{\mu\nu}^0 &= \partial_\mu Z_\nu^0 - \partial_\nu Z_\mu^0.
\end{aligned}$$

In terms of  $v$  and the  $SU(2)_L$  and  $U(1)_Y$  coupling constants  $g$  and  $g'$ , the new parameters are

$$\begin{aligned}
\sin \theta_W &= \frac{g'}{(g'^2 + g^2)^{\frac{1}{2}}}, \\
e &\equiv \frac{g'g}{(g'^2 + g^2)^{\frac{1}{2}}}, \\
M_W &= \frac{1}{2}vg, \\
M_Z &= \frac{1}{2}v(g'^2 + g^2)^{\frac{1}{2}} = \frac{M_W}{\cos \theta_W}.
\end{aligned}$$

$\eta$  is the real Higgs scalar field.

Finally, the lepton and quark terms are:

$$L_{lepton} + L_{quark} =$$

$$\begin{aligned}
& \sum_{\text{all } f} \bar{f} [i \not{\partial} - e Q_f \not{A} - m_f - \frac{g m_f}{2 M_W} \eta] f \\
& + \sum_q \bar{q} (-g_s \gamma^\mu \frac{1}{2} \lambda_a) q G_{\mu,a} \\
& - \frac{g}{\sqrt{2}} \sum_{i=e,\mu,\tau,u,c,t} \bar{\psi}_i^{(L)} \gamma^\mu [\sigma^+ W_\mu^+ + \sigma^- W_\mu^-] \psi_i^{(L)} \\
& - \frac{g}{2 \cos \theta_W} \sum_{\text{all } f} \bar{f} \gamma^\mu (v_f - a_f \gamma^5) f Z_\mu^0.
\end{aligned}$$

Recall that electroweak doublets have  $I_3 = \pm \frac{1}{2}$  for their upper and lower components, respectively. Then the vector and axial-vector couplings of the  $Z^0$  to a fermion are given by

$$v_f = I_{3,f} - 2Q_f \sin^2 \theta_W,$$

$$a_f = I_{3,f}.$$

$\sigma^\pm$  are equal to  $\frac{1}{2}(\sigma_1 \pm i\sigma_2)$ , respectively.

# Appendix B

## Helicity Amplitude Method

### B.1 Helicity Eigenstates

In the Weyl basis the gamma matrices are the following  $4 \times 4$  matrices

$$\gamma^0 = \begin{pmatrix} 0 & 1 \\ 1 & 0 \end{pmatrix}, \quad \gamma^j = \begin{pmatrix} 0 & -\sigma_j \\ \sigma_j & 0 \end{pmatrix}, \quad \gamma^5 = \begin{pmatrix} 1 & 0 \\ 0 & -1 \end{pmatrix},$$

where  $\sigma_j$  are the Pauli  $2 \times 2$  spin matrices

$$\sigma_1 = \begin{pmatrix} 0 & 1 \\ 1 & 0 \end{pmatrix}, \quad \sigma_2 = \begin{pmatrix} 0 & -i \\ i & 0 \end{pmatrix}, \quad \sigma_3 = \begin{pmatrix} 1 & 0 \\ 0 & -1 \end{pmatrix}.$$

The spin operator for a Dirac particle is  $\frac{1}{2} \vec{\Sigma}$ , where in terms of the Pauli matrices

$$\vec{\Sigma} = \begin{pmatrix} \vec{\sigma} & 0 \\ 0 & \vec{\sigma} \end{pmatrix}.$$

We define the helicity operator  $h(\vec{p}) = \vec{\Sigma} \cdot \hat{p}$ , with eigenvalues  $\lambda = +1$  and  $-1$  corresponding to spin parallel and antiparallel to the momentum  $\vec{p}$ , respectively.

A four-component Dirac spinor can be written as

$$\psi = \begin{pmatrix} \psi_+ \\ \psi_- \end{pmatrix},$$

where  $\psi_+$  and  $\psi_-$  are two-component spinors.  $\psi$  is a helicity eigenstate if for fermions

$$\psi_{\pm} = u_{\pm} = \omega_{\pm\lambda} \chi_{\frac{\lambda}{2}}, \quad (\text{B.1})$$

Table B.1: Helicity states in two-component spinor, and bra-ket notation.

$u_+(\lambda = +1)$	$+\sqrt{E +  \vec{p} }  \hat{p}+ \rangle$
$u_+(\lambda = -1)$	$+\sqrt{E -  \vec{p} }  \hat{p}- \rangle$
$u_-(\lambda = +1)$	$+\sqrt{E -  \vec{p} }  \hat{p}+ \rangle$
$u_-(\lambda = -1)$	$+\sqrt{E +  \vec{p} }  \hat{p}- \rangle$
$v_+(\lambda = +1)$	$+\sqrt{E -  \vec{p} }  \hat{p}- \rangle$
$v_+(\lambda = -1)$	$-\sqrt{E +  \vec{p} }  \hat{p}+ \rangle$
$v_-(\lambda = +1)$	$-\sqrt{E +  \vec{p} }  \hat{p}- \rangle$
$v_-(\lambda = -1)$	$+\sqrt{E -  \vec{p} }  \hat{p}+ \rangle$

and for anti-fermions

$$\psi_{\pm} = v_{\pm} = \pm \lambda \omega_{\mp \lambda} \chi_{-\frac{\lambda}{2}}, \quad (\text{B.2})$$

with  $\omega_{\pm} = \sqrt{E \pm |\vec{p}|}$ . Here  $\chi_{\lambda/2}$  is the eigenvector of the  $2 \times 2$  operator  $\vec{\sigma} \cdot \hat{p}$  with eigenvalue  $\lambda = \pm 1$ . These two-component eigenvectors  $\chi_{\lambda/2}$ , are

$$\chi_{1/2} = \begin{pmatrix} \cos \theta/2 \\ e^{i\phi} \sin \theta/2 \end{pmatrix}, \quad \chi_{-1/2} = \begin{pmatrix} -e^{-i\phi} \sin \theta/2 \\ \cos \theta/2 \end{pmatrix},$$

where  $\theta, \phi$  are the directional polar coordinates of  $\vec{p}$ . We also introduce a ket notation for the Weyl two-component eigenvectors

$$|\hat{p}+ \rangle \equiv \chi_{1/2}, \quad |\hat{p}- \rangle \equiv \chi_{-1/2}.$$

In this notation, the eigenstates for fermions ( $u_{\pm}$ ) and anti-fermions ( $v_{\pm}$ ) for each helicity are listed in Table B.1. The helicity eigenvectors for massless fermions in four-component Dirac form have either  $\psi_+$  or  $\psi_-$  equal to zero; and the non-zero two-component spinor is proportional to  $\chi_{\pm\lambda/2}$ . The massless Dirac helicity eigenvectors are shown in Table B.2 in terms of Weyl spinors. Because two components are zero the algebra reduces to two-component spinors acted on by  $2 \times 2$  matrices.

Table B.2: Dirac helicity eigenvectors for massless fermions.

	$\lambda = +1$	$\lambda = -1$
Fermion	$\psi = \begin{pmatrix} +\sqrt{2E}\chi_{1/2} \\ 0 \end{pmatrix}$	$\psi = \begin{pmatrix} 0 \\ +\sqrt{2E}\chi_{-1/2} \end{pmatrix}$
Antifermion	$\psi = \begin{pmatrix} 0 \\ -\sqrt{2E}\chi_{-1/2} \end{pmatrix}$	$\psi = \begin{pmatrix} -\sqrt{2E}\chi_{1/2} \\ 0 \end{pmatrix}$

The chirality projection operators are defined to be

$$P_{\pm} = \frac{1}{2}(1 \pm \gamma_5).$$

In the Weyl basis they are diagonal

$$P_+ = \begin{pmatrix} 1 & 0 \\ 0 & 0 \end{pmatrix}, \quad P_- = \begin{pmatrix} 0 & 0 \\ 0 & 1 \end{pmatrix},$$

and they project out  $\psi_{\pm}$ , respectively.

Feynman diagram calculations with a fermion propagator include a factor of  $\not{p} = p_{\mu}\gamma^{\mu}$ . In the Weyl basis

$$\gamma^{\mu} \equiv \begin{pmatrix} 0 & \gamma_+^{\mu} \\ \gamma_-^{\mu} & 0 \end{pmatrix},$$

where

$$\gamma_{\pm}^{\mu} = (1, \mp \vec{\sigma}).$$

Thus,

$$\not{p} = \begin{pmatrix} 0 & p^0 + \vec{\sigma} \cdot \vec{p} \\ p^0 - \vec{\sigma} \cdot \vec{p} & 0 \end{pmatrix}.$$

The Fierz identities are useful for performing contractions. In terms of bra-kets one identity is

$$\langle i|\gamma_{\pm}^{\mu}|j\rangle \langle k|\gamma_{\mp\mu}|l\rangle = 2 \langle i|l\rangle \langle k|j\rangle. \quad (\text{B.3})$$

Also, for each ket  $|\hat{p}_{\pm}\rangle$ , we define an associated ket  $|\widetilde{\hat{p}_{\pm}}\rangle$  by

$$|\widetilde{\hat{p}_{\pm}}\rangle = \mp |\hat{p}_{\mp}\rangle.$$

Then it can be shown that

$$\langle i|\gamma_{\pm\mu_1}\dots\gamma_{\pm\mu_n}|j\rangle = \langle \tilde{j}|\gamma_{\mp\mu_n}\dots\gamma_{\mp\mu_1}|\tilde{k}\rangle. \quad (\text{B.4})$$

Therefore uniting Eqs.(B.3) and (B.4) another Fierz identity is

$$\langle i|\gamma_{\pm}^{\mu}|j\rangle \langle k|\gamma_{\pm\mu}|l\rangle = 2 \langle i|\tilde{k}\rangle \langle \tilde{l}|j\rangle. \quad (\text{B.5})$$

For a spin-1 field, the right-handed (R), left-handed (L), and longitudinal (0) polarization vectors are

$$\begin{aligned} \epsilon_R^{\mu} &= \frac{e^{i\phi}}{\sqrt{2}}(0, i \sin \phi - \cos \phi \cos \theta, -i \cos \phi - \sin \phi \cos \theta, \sin \theta) \\ \epsilon_L^{\mu} &= \frac{e^{-i\phi}}{\sqrt{2}}(0, i \sin \phi + \cos \phi \cos \theta, -i \cos \phi + \sin \phi \cos \theta, -\sin \theta) \\ \epsilon_0^{\mu} &= \frac{1}{m}(|\vec{p}|, E \sin \theta \cos \phi, E \sin \theta \sin \phi, E \cos \theta). \end{aligned}$$

$\theta$  and  $\phi$  are spherical coordinates specifying the direction of the boson's momentum. The longitudinal polarization applies only to massive vector bosons.

## B.2 Example Calculation

In this section we give an example calculation of a Feynman diagram, using helicity states. We also briefly discuss the numerical calculation of the cross section.

We calculate the Feynman diagram in Fig. B.1(b), which is one term in the amplitude for  $W\gamma$  production (with  $W$  decay). This s-channel diagram includes a triple-boson vertex. For simplicity we assume  $\lambda_{\gamma} = 0$ . Then the  $WW\gamma$  vertex factor, with momentum definitions as shown in Figure B.1(a), is  $-ig \sin \theta_W \Gamma^{\alpha\beta\mu}$ , where

$$\begin{aligned} \Gamma^{\alpha\beta\mu}(q, \bar{q}, p) &= (q - \bar{q})^{\mu} g^{\alpha\beta} - (p + q)^{\beta} g^{\mu\alpha} + (p + \bar{q})^{\alpha} g^{\mu\beta} \\ &+ \Delta\kappa_{\gamma}(p^{\alpha} g^{\mu\beta} - p^{\beta} g^{\mu\alpha}). \end{aligned} \quad (\text{B.6})$$

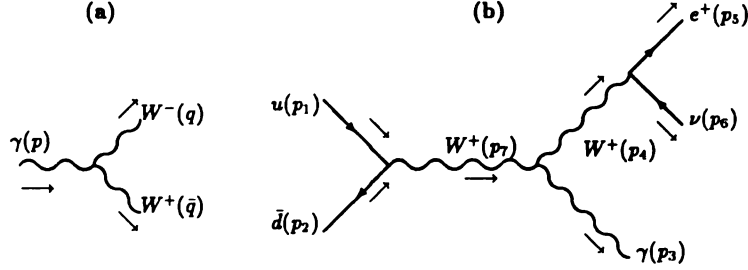


Figure B.1: (a) The  $WW\gamma$  vertex. (b) Example diagram for  $u\bar{d} \rightarrow W^+\gamma \rightarrow e^+\nu\gamma$ . Arrows indicate the defined momentum direction.

(The factor for the  $WWZ$  vertex would be identical, with  $\sin \theta_W$  replaced by  $\cos \theta_W$ .)

With the assignment

$$p = -p_3$$

$$q = -p_7$$

$$\bar{q} = p_4$$

we can write down the contribution to the amplitude from this diagram

$$M = \frac{-ieg^2}{2} \frac{1}{(p_4^2 - M_W^2)} \frac{1}{(p_7^2 - M_W^2)} \cdot [\bar{v}(2)\gamma_\alpha P_- u(1)] \cdot [\bar{u}(6)\gamma_\beta P_- v(5)] \cdot \epsilon_\mu^*(3)\Gamma^{\alpha\beta\mu}, \quad (\text{B.7})$$

where we have adopted the shorthand  $u(1) = u(p_1)$ , etc. Note that the  $f\bar{f}W$  vertex has a chirality projection operator  $P_-$  because of the parity violating V-A coupling.

To simplify the first term in square brackets, we note that

$$[\bar{v}(2)\gamma_\alpha P_- u(1)] = [\bar{v}(2)P_+\gamma_\alpha P_- u(1)]$$

and that

$$\begin{aligned}
\bar{v}(2)P_+ &= v^\dagger(2)\gamma^0P_+ \\
&= (v_+^\dagger(2) \ v_-^\dagger(2)) \begin{pmatrix} 0 & 0 \\ 1 & 0 \end{pmatrix} \\
&= (v_-^\dagger(2) \ 0) \\
P_-u(1) &= \begin{pmatrix} 0 & 0 \\ 0 & 1 \end{pmatrix} \begin{pmatrix} u_+(1) \\ u_-(1) \end{pmatrix} \\
&= \begin{pmatrix} 0 \\ u_-(1) \end{pmatrix}.
\end{aligned} \tag{B.8}$$

From Eqs. (B.1) and (B.2) we deduce that, in order to be non-zero,  $u_-(1)$  and  $v_-^\dagger(2)$  must have  $\lambda$  equal to minus and plus one, respectively; that is, the up quark is left-handed and the  $\bar{d}$  is right-handed. We make a similar simplification of the other square-bracketed factor in Eq. (B.7). Then we can use Table B.1 to write the amplitude in terms of bra-kets:

$$\begin{aligned}
M &= \frac{-ieg^2}{2} \frac{1}{(p_4^2 - M_W^2)} \frac{1}{(p_7^2 - M_W^2)} \sqrt{2E_1 2E_2 2E_5 2E_6} \cdot \\
&\quad \langle 2 - |\gamma_{+\alpha}| 1 - \rangle \cdot \langle 6 - |\gamma_{+\beta}| 5 - \rangle \cdot \epsilon_\mu^*(3) \Gamma^{\alpha\beta\mu}.
\end{aligned} \tag{B.9}$$

Using Eq. (B.6) for  $\Gamma_{\alpha\beta\mu}$  and the Fierz identity, (B.3), we simplify the Lorentz contractions to get

$$\begin{aligned}
M &= \frac{-ieg^2}{2} \frac{1}{(p_4^2 - M_W^2)} \frac{1}{(p_7^2 - M_W^2)} \sqrt{2E_1 2E_2 2E_5 2E_6} \cdot \\
&\quad \{-2(p_4 + p_7) \cdot \epsilon^*(3) \langle 2 - | 6 + \rangle \langle 5 + | 1 - \rangle \\
&\quad + \langle 6 - | (\not{p}_7 + \not{p}_3)_+ | 5 - \rangle \langle 2 - | \not{\epsilon}_+^*(3) | 1 - \rangle \\
&\quad + \langle 2 - | (\not{p}_4 - \not{p}_3)_+ | 1 - \rangle \langle 6 - | \not{\epsilon}_+^*(3) | 5 - \rangle \\
&\quad + \Delta\kappa_\gamma [\langle 6 - | \not{p}_{3+} | 5 - \rangle \langle 2 - | \not{\epsilon}_+^*(3) | 1 - \rangle \\
&\quad - \langle 2 - | \not{p}_{3+} | 1 - \rangle \langle 6 - | \not{\epsilon}_+^*(3) | 5 - \rangle] \},
\end{aligned} \tag{B.10}$$

where  $\not{p}_\pm$  denotes  $p_\mu \gamma_\pm^\mu$ .

The rest of the cross section calculation is done by computer. Components of the transition amplitude in the form of Eq. (B.10) are calculated numerically by a FORTRAN subroutine. To obtain a differential or total cross section, the “hard” cross section in terms of partons must be convoluted with the parton distribution functions and integrated over the momentum fractions of the initial partons. The hard cross section (for massless partons) is

$$\hat{\sigma} = \frac{(2\pi)^4}{2\hat{s}} |\mathcal{M}|^2 d\Phi, \quad (\text{B.11})$$

where  $\hat{s}$  is the partonic center-of-mass energy,  $\mathcal{M}$  is the matrix element, and  $d\Phi$  is the phase-space element appropriate to the number of outgoing particles. The total hadronic cross section is then

$$\sigma = \int dx dx' f(x) f'(x') \hat{\sigma}, \quad (\text{B.12})$$

where  $x$  and  $x'$  are the momentum fractions of a parton in the proton and antiproton, respectively. (This is one term; we also include a term in which the  $f$  and  $f'$  originate in the antiproton and proton, with probability  $f(x')f'(x)$ .) Our Monte-Carlo program, based on PAPAGENO [32], evaluates the phase-space and  $x$  integrals simultaneously by summing the kinematic and matrix element weights of many events. That is, for each event a set of random  $x$ 's and momenta are generated which satisfy all kinematic constraints. The  $x$ 's determine the parton distribution weight, while the momenta determine the matrix element and phase space weights. The product of these weights, summed over many events, yields the cross section. The parameters of each event are stored in an HBOOK NTUPLE, so that we may project out the distribution of events along any kinematic variable, *i.e.* the differential cross sections.

# BIBLIOGRAPHY

# Bibliography

- [1] G. Sterman, *An Introduction to Quantum Field Theory* (Cambridge University Press, 1993).  
M. Kaku, *Quantum Field Theory A Modern Introduction* (Oxford University Press, 1993).
- [2] S.L. Glashow, *Nucl. Phys.* **22**, 579 (1961).  
A. Salam, *Elementary Particle Theory*, ed. N. Svartholm, Stockholm, Almquist, and Wiksells (1968).  
S. Weinberg, *Phys. Rev. Lett.* **19**, 1264 (1967).
- [3] F. Englert and R. Brout, *Phys. Rev. Lett.* **13**, 321 (1964).  
G.S. Guralnik, C.R. Hagen, and T.W.B. Kibble, *Phys. Rev. Lett.* **13**, 585 (1964).  
P.W. Higgs, *Phys. Lett.* **12**, 132 (1964); *Phys. Rev.* **145**, 1156 (1966).
- [4] M. Kobayashi and T. Maskawa, *Progr. Theor. Phys.* (Kyoto) **49**, 652 (1973).
- [5] K.G. Wilson and J.G.Kogut, *Phys. Rep.* **12**, 75 (1974);  
R.S.Chivukula and E. Simmons, hep-ph/9608320.
- [6] T. D. Lee and C. N. Yang, *Phys. Rev.* **128**, 885 (1962).

- [7] H. Georgi, Nucl. Phys. **B361**, 339 (1991). H. Georgi, *Weak Interactions and Modern Particle Theory* (The Benjamin/Cummings Publishing Company, 1984).
- [8] DØ Collaboration, S. Abachi *et. al.*, Phys. Rev. Lett. **75**, 1034 (1995).
- [9] DØ Collaboration, B. Abbott *et. al.*, hep-ex/9705010, Fermilab-Pub-97/136-E.
- [10] DØ Collaboration, S. Abachi *et. al.*, hep-ex/9704004, Fermilab-Pub-97/088-E.
- [11] CDF Collaboration, F. Abe *et. al.*, Phys. Rev. Lett. **74**, 1936 (1995).
- [12] CDF Collaboration, F. Abe *et. al.*, Phys. Rev. Lett. **75**, 1017 (1995).
- [13] K. Hagiwara, J. Woodside, and D. Zeppenfeld, Phys. Rev. **D41** 2113 (1990).
- [14] U. Baur and D. Zeppenfeld, Phys. Lett. **B201**, 383 (1988).
- [15]  $(g - 2)_\mu$ : F. Herzog, Phys. Lett. **bf B148** (1984) 355;  
M. Suzuki, Phys. Lett. **B153** (1985) 289;  
J.C. Wallet, Phys. Rev. **D32** (1985) 813;  
A. Grau and J.A. Grifols, Phys. Lett. **B154** (1985) 283.  
Low energy neutrino scattering: J. A. Grifols, S. Peris, and J. Sola, Phys. Lett. **B197** (1987) 437.  
 $W - Z^0$  mass difference: M. Suzuki, Phys. Lett. **B153** (1985) 289;  
H. Neufeld, D. Schildknecht and J.D. Stroughair, Phys. Lett. **B198** (1987) 563;  
J.A. Grifols, S. Peris and J. Sola, DESY preprint DESY-86-055;  
J.J. van der Bij, Phys. Rev. **D35** (1987) 1088.
- [16] H. Aihara *et. al.*, Fermilab-Pub-95/031, to be published in "Electroweak Symmetry Breaking and Beyond the Standard Model," eds. T. Barklow, S. Dawson, H. Haber, and J. Siegrist.

- [17] F.M. Renard, S. Spagnolo, and C. Verzegnassi, Preprint hep-ph/9705274.
- [18] K. Hagiwara, R. D. Peccei, D. Zeppenfeld, and K. Hikasa, *Nucl. Phys.* **B282** (1987) 253.
- [19] *e<sup>+</sup>e<sup>-</sup> Collisions at 500 Gev: The Physics Potential*, Hamburg, Germany, 1993, Ed. P.M. Zerwas; and *Physics and Experiments with Linear e<sup>+</sup>e<sup>-</sup> Colliders*, Waikoloa, USA, 1993, Ed. F.A. Harris et al.
- [20] A. Miyamoto in “Workshop on Physics and Experiments with Linear e<sup>+</sup>e<sup>-</sup> Colliders, Volume 1,” Eds. F.A. Harris, S.L. Olsen, S. Pakvasa, X. Tata (World Scientific 1993); p.141.
- [21] G. P. LePage, *J. Comp. Phys.* **27**, 192 (1978).
- [22] J.R. Taylor, *An Introduction to Error Analysis* (University Science Books 1982).
- [23] *Acceleration of Polarized Protons to 120 and 150 GeV in the Fermilab Main Injector*, University of Michigan Report UM HE 92-5, March 1992 (unpublished); *Progress Report: Acceleration of Polarized Protons to 1 TeV in the Fermilab Tevatron*, University of Michigan Report UM HE 94-15, August 1994 (unpublished).
- [24] Expression of Interest, *Polarization Physics at the Tevatron Collider*, by R. Brock, G. A. Ladinsky, D. Stump, M. Wiest, H. Weerts, C.-P. Yuan, and G. Blazey, May-5, 1994.
- [25] Morfin and W. K. Tung, *Z. Phys.* **C52**, 13 (1991).
- [26] G. A. Ladinsky, *Phys. Rev.* **D46**, 3789 (1992); **D47**, 3086 (1993).
- [27] P. L. Anthony *et al.*, *Phys. Rev. Lett.* **71**,959 (1993); J. Ashman *et al.*, *Nucl. Phys.* **B328**,1 (1989); B. Adeva, *et al.*, *Phys. Lett.* **B302**, 533 (1993).

- [28] Spin Muon Collaboration, *Phys. Lett.* **B329**, 399 (1994).
- [29] H.-Y. Cheng, "Status of the Proton Spin Problem," hep-ph/9607254; M. Anselmino, A. Efremov, and E. Leader, *Phys. Rep.* **261**, 1 (1995).
- [30] U. Baur and E. Berger, *Phys. Rev.* **D41**, 1476 (1990).
- [31] U. Baur, T. Han, and J. Ohnemus, *Phys. Rev.* **D48**, 5140 (1993).
- [32] I. Hinchliffe, *Argonne Accel. Phys.*, 679 (1993).
- [33] K. Hagiwara and D. Zeppenfeld, *Nucl. Phys.* **B313**, 560 (1989). Our program is based on a program by D. Zeppenfeld, W. Long, T. Han, and D. Zeppenfeld. We have modified their code to select helicity amplitudes for specific helicity states of the initial partons, and to use polarized parton distribution functions.
- [34] J. Bagger, V. Barger, K. Cheung, J. Gunion, T. Han, G. Ladinsky, R. Rosenfeld, and C.-P. Yuan, *Rhys. Rev.* **D49**, 1246 (1994).
- [35] J. Botts, J. Huston, H. L. Lai, J. G. Morfin, J. F. Owens, J. Qiu, W.-K. Tung, H. Weerts, Michigan State Univeristy preprint MSUTH-93/17 (unpublished).
- [36] M. J. Alguard *et al*, *Phys. Rev. Lett.* **37**, 1261 (1976); G. Baum *et al*, *Phys. Rev. Lett.* **45**, 2000 (1982); *Phys. Rev. Lett.* **51**, 1135 (1983).
- [37] R. D. Carlitz and J. Kaur, *Phys. Rev. Lett.* **38**, 673 (1977); J. Kaur, *Nucl. Phys.* **B128**, 219 (1977).
- [38] P. M. Nadolsky, *Z. Phys.* **C63**, 601 (1994).
- [39] T. Gehrmann and W. J. Stirling, *Z. Physik* **C65**,461 (1995).
- [40] P. M. Nadolsky, Institute for High-Energy Physics (Protvino, Russia) preprint, Mar. 1995.

- [41] G. R. Farrar and D. R. Jackson, *Phys. Rev. Lett.* **35**, 1416 (1975).
- [42] J. Soffer and J.M. Virey, Preprint Hep-ph/9706229.
- [43] C. Bourrely and J. Soffer, *Phys. Lett.* **B314**, 132 (1993).
- [44] C. Bourrely, J. Ph. Guillet and J. Soffer, *Nucl. Phys.* **B361**, 72 (1991).
- [45] R.L. Jaffe and N. Saito, *Phys. Lett.* **B382**, 165 (1996).
- [46] C.S. Aulakh, K. Benakli, and G. Senjanovic, preprint hep-ph/9703434.
- [47] P. Fayet, "Supersymmetry, Particle Physics, and Gravitation", in *Unification of the fundamental particle interactions*, eds. S. Ferrara, J. Ellis and P. Van Nieuwenhuizen (Plenum, New York, 1980); P. Fayet, *Phys. Lett.* **84B**, 421 (1979).
- [48] H. Haber, "Introduction to Low-Energy Supersymmetry," lectures at the 1992 Theoretical Advanced Study Institute, University of Colorado.
- [49] M. Dine, "Supersymmetry: Microphysics and Macrophysics," lectures at the 1988 Theoretical Advanced Study Institute, Brown University.
- [50] L.E. Ibanez and C.G. Ross, *Phys. Lett.* **110B** (1982) 215; K. Inoue, A. Kakuto, H. Komatsu, and S. Takeshita, *Progr. Theor. Phys.* **68** (1982) 927; L. Alvarez-Gaume, J. Polchinsky, and M. Wise, *Nucl. Phys.* **B221** (1983) 495; J. Ellis, D.V. Nanopoulos, and K. Tamvakis, *Phys. Lett.* **121B** (1983) 123.
- [51] M. Dine, A.E. Nelson, Y. Nir, and Y. Shirman, *Phys. Rev.* **D53** (1996) 2658-2669.
- [52] M. Dine, A. Nelson, and Y. Shirman, *Phys. Rev.* **D51** 1362 (1995).

- [53] J. Ellis, K. Enqvist, and D.V. Nanopoulos, *Phys. Lett. B* **147** (1984) 99; A. Lahanaz, and D.V. Nanopoulos, *Phys. Rep.* **145** (1987) 1; J.L. Lopez, and D.V. Nanopoulos, Preprint hep-ph/9607220.
- [54] S. Dimopoulos, M. Dine, S. Raby and S. Thomas, *Phys. Rev. Lett.* **76** (1996) 3494-3497.
- [55] S. Ambrosiano, G.L. Kane, G.D. Kribs, S.P. Martin, S. Mrenna, *Phys. Rev. D* **54** (1996) 5395-5411.
- [56] R.G. Roberts and L. Roszkowski, *Phys. Lett.* **B309**, 329 (1993).
- [57] G.L. Kane, C. Kolda, L. Roszkowski, J.D. Wells, *Phys. Rev. D* **49** 6173 (1994).
- [58] D.R. Stump, M. Wiest, C.-P. Yuan, *Phys. Rev. D* **54**, 1993 (1996).
- [59] J. Ellis and J. S. Hagelin, *Phys. Lett.* **122B** 303 (1983).
- [60] H. E. Haber and G. L. Kane, *Phys. Rep.* **117**, 76 (1985).
- [61] M. K. Gaillard, L. Hall and I. Hinchliffe, *Phys. Lett.* **116B** 279 (1982).
- [62] R. Frey, private communication.
- [63] S. Ambrosiano, G.L. Kane, G.D. Kribs, S.P. Martin, S. Mrenna, *Phys. Rev. Lett.* **76** (1996) 3498-3501.
- [64] J.L. Lopez and D.V. Nanopoulos, *Mod. Phys. Lett.* **A10** (1996) 2473.